DEVELOPMENT OF SPECTROSCOPIC SMARTPHONE BIOSENSORS FOR POINT-OF-CARE APPLICATIONS

BY

KENNETH D. LONG

DISSERTATION

Submitted in partial fulfillment of the requirements
for the degree of Doctor of Philosophy in Bioengineering
in the Graduate College of the
University of Illinois at Urbana-Champaign, 2018

Urbana, Illinois

Doctoral Committee:

Professor Brian T. Cunningham, Chair
Professor Rashid Bashir
Professor Stephen A. Boppart
Associate Professor Chad J. Achenbach, Northwestern University

ABSTRACT

This dissertation explores the combination of two emergent areas within contemporary biosensing, smartphone based spectroscopy and photonic crystal enhanced microscopy, and how these technologies can be combined to produce a fundamentally novel point-of-care testing paradigm: a portable device platform capable of non-amplifying, digital-detection for high-sensitivity diagnostics. In this work, I describe the development of this system, moving from usage-specific benchtop and smartphone based devices demonstrating proof-of-concept capabilities, to a multimodal smartphone platform compatible with thousands of existing spectroscopic assays. The resulting smartphone biosensor can perform various clinically-relevant tests with physiologically-relevant sensitivities. Next, photonic crystal enhanced microscopy is described for uses in the micrometer and nanometer scales for use both to study cellular and subcellular behavior and also to perform single-particle attachment quantification. Finally, this work explores how the single-particle attachment quantification capability can be leveraged to measure HIV viral load using a novel biosensor, designed specifically developed for a smartphone based platform for point of care applications.

ACKNOWLEDGEMENTS

This work reflects the support of so many individuals and organizations. To my funders, including NIH F30 AI122925A, NSF CBET 12-64377, and NIH R25 CA154015A, thank you for the support of my education and research. I wish to thank the Bioengineering Department, the Medical Scholars Program at UI-COM, and the ISUR program (including support from both Intel and SRC) for their support of my training.

I would like to express my appreciation for the journals and publishers that have kindly allowed me to include material first published with them. Specifically, portions of Chapter 2, including Subsections 2.2.1, 2.2.2, and Section 2.3, as well as Figures 2.3 and 2.11 are adapted and reproduced from Ref. 16 with permission from the Royal Society of Chemistry. Section 2.2, including Figures 2.4-2.9, is adapted and reproduced from Ref. 10 with permission from the Optical Society of America. © 2014 Optical Society of America. Users may use, reuse, and build upon content from this article, or use the article for text or data mining, so long as such uses are for non-commercial purposes and appropriate attribution is maintained. All other rights are reserved. Much of Chapter 3, including Figures 3.1 – 3.9 is adapted and reproduced from Ref. 87 with permission from the Royal Society of Chemistry. Some material in Sections 3.2 and 3.4 was first published with IEEE, as indicated by references at the end of those paragraphs. © 2017 IEEE. Reprinted, with permission, from Reference #95, *Long, K. D., Woodburn, E. V. & Cunningham, B. T. in IEEE-NIH 2017 Special Topics Conference on Healthcare Innovations and Point-of-Care Technologies (IEEE EMB, NIH Natcher Conference Center, Bethesda, MD, November 6-8 2017).* Sections 4.3-4.7, including Figures 4.2-4.5, is adapted and reproduced from Ref. 114 with permission from the Royal Society of Chemistry.

I want to express my gratitude to each of my committee members for their support and wisdom over the years, both with my research and preparation for a career as a physician-scientist. Professor Boppart, as the first MD-PhD I had the pleasure of meeting as a Freshman ECE student, and a member of my interview committee into the MSP, it's such a privilege to have you participate in this next step of my career. Professor Bashir, thank you for your support of my research and mentorship through my F30 award, but also for your support of my global health ambitions. Dr. Achenbach, thank you for your continued patience and mentorship in the clinic over the past 3 years—it has truly informed both my research and my ambitions as a future physician-scientist. Most importantly, I wish to thank Professor Cunningham for his help and guidance throughout the work leading up to this manuscript, and for his continued flexibility during this period of my graduate studies. With his direction, I have been afforded opportunities and experiences that I will carry with me for the rest of my career.

Similarly, I thank past- and present-members of the Nano Sensors Group, specifically Vikram, Erich, Meng, and Gloria for their guidance and mentorship, as well as Weili, Yue, Nantao, Miguel, and Che for their fantastic work ethic and assistance through the past 6 years. I would like to express both gratitude and encouragement to Maggie, Sonya, and Elizabeth—I appreciate you letting me be a part of your education.

I would like to express thanks to my friends and family for their continued support and encouragement, especially Ritu, Alex, and Emily, with whom I've shared so many celebrations and commiserations. To Ian, my partner, friend, and co-adventurer, thank you for your unwavering love and support.

TABLE OF CONTENTS

CHAPTER 1: INTRODUCTION

Since the introduction of smartphones in 2004, interest in coupling them with wearable devices for monitoring health-related metrics has grown to an over $15 billion/year market[1] , focused mainly upon reporting physiological parameters such as heart rate and blood pressure. While the majority of these consumer products are not classified as medical devices, there is intense interest in coupling new sensors to mobile devices to transition additional health diagnostics, particularly *in vitro* diagnostic (IVD) tests on bodily fluids from the laboratory to the point-of-care (POC). Tests that can be facilitated through test-specific cartridges that interface with a readout instrument [2,3] or paper-based assays that can be interpreted by visual inspection have obtained regulatory approval that facilitates their use in POC settings.[4,5]

As smartphones continue to include greater computational power and more sophisticated imaging sensors that complement their capabilities for wireless communication and internet connectivity, the interface between IVD testing and mobile devices offers a powerful new POC testing paradigm. The output of nearly all of the most common laboratory-based diagnostic tests can be sensed using a smartphone with sensitivity that rivals that of conventional laboratory-based benchtop instruments. Examples include smartphone-based microscopy,[6,7] fluorimetry,[8,9] Enzyme Linked Immunosorbent Assay (ELISA),[10] Polymerase Chain Reaction (PCR),[11] and lateral flow assays.[12,13] The reader is directed to recent reviews on the topic of smartphone-based biosensing.[14,15] It is evident that while laboratory-based assays and detection instruments provide high throughput and automation, enormous needs exist to provide diagnostic information to people who lack convenient access to a diagnostic test facility. Additionally, in many urgent health situations, an immediate result is required for feedback to the physician and patient.

Over the past six years, I have engaged in research developing POC diagnostic platforms across the entire design process: from ideation through demonstration of utility. In this dissertation I will describe the progression of that work from early "benchtop" devices, demonstrating basic capabilities, through final prototypes of smartphone-based platforms capable of performing myriads of diagnostic tests which are otherwise typically dependent on a standard laboratory infrastructure. Then, I will describe the development of a novel detection strategy for a significant global health need, a point-of-care HIV viral load test, which relies on the fundamentals of earlier work combined with cutting-edge biosensing research. I hope that this document will track the progression of smartphone biosensing from a "catch-up" phase of replicating detection modalities already refined in a laboratory setting to a future where novel biosensing research is developed using smartphone-based platforms from the onset.

This dissertation will be composed of two principal parts: first, a description of various projects focusing on the translation of existing spectrometric measurement platforms and assays to various smartphone-based devices, and second, a description of a nascent biosensing technique, Photonic Crystal Enhanced Microscopy (PCEM) and its subsequent development directly to a POCT context for providing digital detection of HIV viral load, a significant global health need unserved by contemporary POCT strategies.

In Chapters 2 and 3, I will describe our early work demonstrating the feasibility of using the rear-facing CMOS camera of a smartphone as the imaging sensor of a spectrometer, and the development of lightpaths to perform three broad classes of existing spectrometric assays: absorbance, fluorescence, and label-free assays. For both the absorption and label-free modalities, biological proof-of-concept experiments were completed and will be described demonstrating the

ability of a smartphone-based spectrometric system to perform measurements of analytes at ranges comparable to standard benchtop devices.

In Chapters 4 and 5, I will narrow-in on a single spectroscopic modality, and explore the opportunities for biosensing provided by photonic crystals in more detail. Unlike absorption and fluorescence-based measurements, PC-based biosensors have properties that are inherently spatially-related. Individual attachment events to the sensor surface will generate localized responses of peak wavelength shift and a decrease in reflection efficiency. Where initial experiments utilizing PCs with smartphone-based biosensors lose one dimension of spatial data in exchange for the spectral data, using a line-scanning approach of illumination and light collection can reconstitute that additional spatial dimension, allowing for spatially-resolved spectral information. First, I will discuss the micro-scale implications for biological attachment, which roughly correspond to cellular and sub-cellular attachment events. The experiments I describe will demonstrate the first uses of the PCEM instrument to detect cellular attachment, detachment, and chemotaxis on a PC sensor-surface. Next, I will discuss the nano-scale implications, as we push the limits of spatial resolution in pursuit of the resolution of single molecule-attachment events. This provides an opportunity to perform "digital-detection" of attachment events, which opens up a world of non-amplification-based low-LOD diagnostics. In Chapter 5, I will present the natural advantages that a PCEM-based detection method presents for a future POC diagnostic for HIV viral load, and will discuss the progress that has been made toward developing such an instrument. To close, I will discuss the future strengths and weaknesses of the developed platform for translation to a point-of-care test.

CHAPTER 2: DEVELOPMENT OF USAGE-SPECIFIC SMARTPHONE SPECTROMETERS[1]

2.1 Introduction

This chapter aims to investigate two fundamental optical biosensing modalities: the absorption-based measurement of enzyme-linked immunosorbent assays (ELISAs) and the label-free measurement of biomolecular adsorption on photonic crystal (PC) sensors. First, an overview of ELISA testing will be given, followed by a survey of contemporary attempts to bring the technology out of the traditional laboratory setting. Then, using the developed smartphone based biosensing platform, a demonstration of the system will be completed using a cancer biomarker, human interleukin 6 (IL-6), and a peanut allergen, Ara h 1. Then, the underpinnings of photonic crystal-based detection will be discussed, followed by a summary of the practical experiments that have been demonstrated thus far on a smartphone-based platform. The work in this chapter is meant to compliment other work that has been completed in the realms of microfluidics and sample collection. As a mainstay of diagnostic medicine, spectroscopy poses an important measurement technique to be translated to a point-of-care device, and the work in this chapter serves as an introduction to the first step of realizing a portable instrument capable of replicating measurements of traditional laboratory benchtop analyzers, which will be further refined in Chapter 3.

2.2 Design of a Smartphone Biosensor

2.2.1 Instrument Design and Fabrication

The instrument cradle was designed to interface with an iPhone 4 (800 MHz ARM Cortex A8, Omnivison OV5653 5MP BSI CMOS sensor with f/2.4, 5 element lens; Apple

[1] This Chapter contains work previously published as outlined in both the Acknowledgements and References.

Inc.) by using the onboard, rear-facing camera as a digital light detector. A custom cradle fabricated from anodized aluminum was designed to align the necessary optics with the phone camera.[16] This cradle allows for the precise alignment of the optical path with the aperture of the smartphone camera, while maintaining full utility of the screen, enabling the camera to function as a spectrometer. The main optical path is comprised of a square channel with two rubber bands along its length so that optical components can be moved along the optical axis, but will maintain proper centering and not move freely on their own. For these experiments, two configurations were used, one for solid-phase PC-based measurements and the other for liquid-phase immunoassays, as shown schematically in Figure 2.1.

For the solid-phase system, a broadband light source (150 W halogen fiber optic high intensity illuminator; Cole Parmer) is used to illuminate a 100-micron pinhole at the end of the channel. Upon entry, light is collimated (focal length, f=75mm) and linearly polarized to align the electric field with the PC grating. At the PC surface, the characteristic narrowband reflection occurs, and the remaining transmitted light is focused to a line via a cylindrical lens (f=50 mm) through the smartphone aperture and onto the CMOS sensor. Between the cylindrical lens and the smartphone is a diffraction grating (1200 lines/mm), which disperses light in one direction generating a spectral dimension on the resulting captured image.

For the liquid-phase system, the same broadband light source is used to illuminate the sample cuvette. Light that is not absorbed by the sample is collected by a 1 mm diameter optical fiber and relayed to a 0.1 mm diameter pinhole at the end of the optical channel.

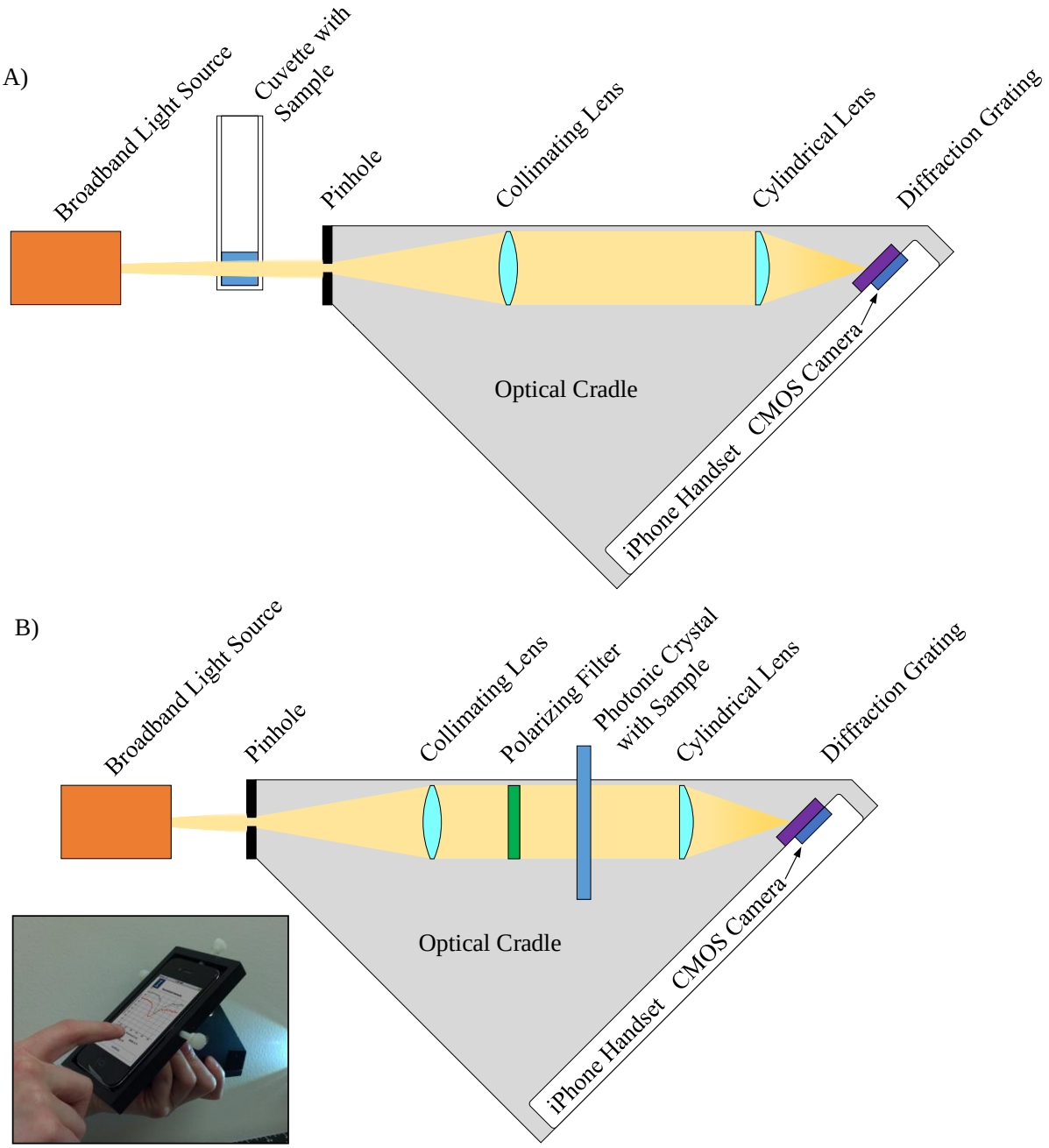

Figure 2.1. Schematic Drawings of Smartphone Biosensing Attachments for A) Absorption measurements for ELISA analysis and B) for PC-based label-free detection of biomolecular attachment. To align the first order diffraction pattern with the CMOS sensor of the smartphone, the optical path is at an angle of approximately 47º. In both systems, the pinhole serves to optically isolate the internal optical path and to maximize spectral resolution, as the diffracted spectrum is convoluted with the apparent light source, just as a slit does on a traditional spectrometer. **Inset: Photograph of smartphone cradle in use.**

Light that enters the optical channel is similarly collimated (f=75mm), focused to a line by a cylindrical lens (f = 50 mm), and diffracted (1200 grooves/mm) as in the solid-phase

instrument.

In both cases, the wavelength components of the light are separated by the diffraction grating, which disperses the light onto the pixels of the camera. Illumination from the lamp is observed in the resulting camera image as a bright, rainbow band appearing near the center of the screen on the smartphone. Although the iPhone4 camera image sensor has a total of 5 megapixels (2592 x 1936), the spectrum band covers approximately 750 pixels in the dispersive direction and it is roughly 100 pixels wide. Assuming a focal length of the iPhone4 lens of 3.85 mm, the wavelength separation between adjacent pixels in the spectral direction will be 0.334 nm/pixel. Due to the spectral responsivity of the Si-based sensor and internal infrared cutoff filters within the camera optics, the range of wavelengths which may be observed by the system extends from approximately 400 to 700 nm.

2.2.2 Use of the Smartphone Instrument

Before introduction to the cradle, the iPhone was prepared by first locking the focus and exposure of the native camera application by focusing on a point sufficiently far away in a dark room or hallway to focus the camera at an infinite distance in a low-light setting. The phone was then placed in the cradle, and a broadband illumination source was turned on at the end of the optical path. The phone was aligned using adjustment knobs to achieve an x-y positioning providing a centered image of a broadband spectrum on the smartphone display. The broadband light source used allowed for the manual manipulation of intensity, which was adjusted to maximize the dynamic range of the sensor for each of the two modalities. For every measurement step, five consecutive images were captured using the native iPhone camera application and averaged to account for variations arising from the

camera hardware and sensor noise. Red and green laser pointers (λ = 656.26 nm and λ = 532.10 nm, respectively) measured with a spectrometer (USB2000+; Ocean Optics) were imaged using the smartphone system to provide reference wavelengths for calibration of the pixel to wavelength conversion.

2.2.3 Image Processing and Wavelength Calibration

Post-processing scripts were written in Matlab to convert raw images into absorption spectra. Once images are uploaded to a PC, auto-thresholding is performed to crop non-data pixels from analysis by removing pixels with zero intensity, which yields a reduction of the image to a ~ 1100 x 100 block of pixels. The intensity of pixels in the non-spectral direction is averaged to yield a one-dimensional vector representation of the spectra.

For both label-based and label-free modalities the data of interest lies in the non-transmitted light: either the light absorbed by the liquid sample or the resonantly reflected resonant peak of the PC. The non-uniformity of both the red, green, and blue (RGB) color filters and the broadband illumination source across the visible wavelengths requires a broadband response be defined (Figure 2.2). For each assay run, a blank consisting of aqueous solution for liquid-phase or air for solid phase is measured. The resulting RGB responses are recorded, and all other analyte samples are subtracted from the blanked RGB channels. To adjust for differences in RGB channel intensity, each channel is individually normalized to unity to provide a near-uniform spectral response.

Pixel values are converted to wavelength values using a linear approximation via known pixel indices calculated by illuminating the pinhole with red and green laser pointers of known wavelength. The laser emission profiles are fit with a 4^{th} order polynomial curve to determine the

precise pixel index of each laser, and are then used to calculate the pixel-to-wavelength conversion, found in this case to be 0.334 nm/pixel.

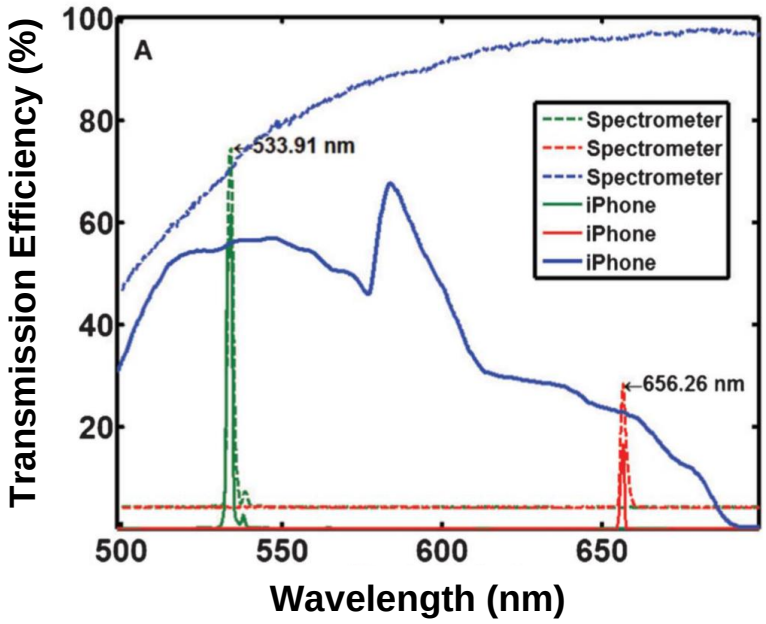

Figure 2.2. Background spectra and calibration lasers. Nonuniform transmission is observed for the bright field light source when imaged by the iPhone because of the RGB filter responses. While broadband transmission must be corrected for via normalization, laser peaks display a high similarity between the spectrometer and the smartphone setup. Using the known wavelengths of these lasers, the rest of the spectrum is interpolated linearly.

2.3 Smartphone-based ELISA

Since its introduction 40 years ago, ELISA has become one of the most widely adaptable tools for biological assays, allowing for the rapid quantification of proteins and antibodies for diseases ranging from HIV to cancer, yielding over 40,000 new articles involving the technology annually.[17]

An ELISA test is completed by immobilizing primary antibodies that possess an affinity for a specific biomolecule of interest onto a surface (usually a 96-well microplate). Next, the biomolecule of interest is introduced to the sensor surface where it will be bound by the immobilized antibody. A secondary antibody, also complimentary to the molecule of interest, is conjugated to an enzyme and introduced to the sensor surface after a thorough washing to remove unbound molecules of interest. These secondary antibodies will only bind to successfully captured molecules of interest. Finally, after another series of washes, a chromogen, or color-generating compound, is introduced. The enzyme present on the secondary antibody cleaves a peptide on the chromogen, which causes it to undergo a shift in its absorption spectrum to the visible range. After the optical absorptions of standards at known concentrations are used to obtain a calibration curve, the concentrations of an analyte within a test sample may be accurately determined via interpolation.

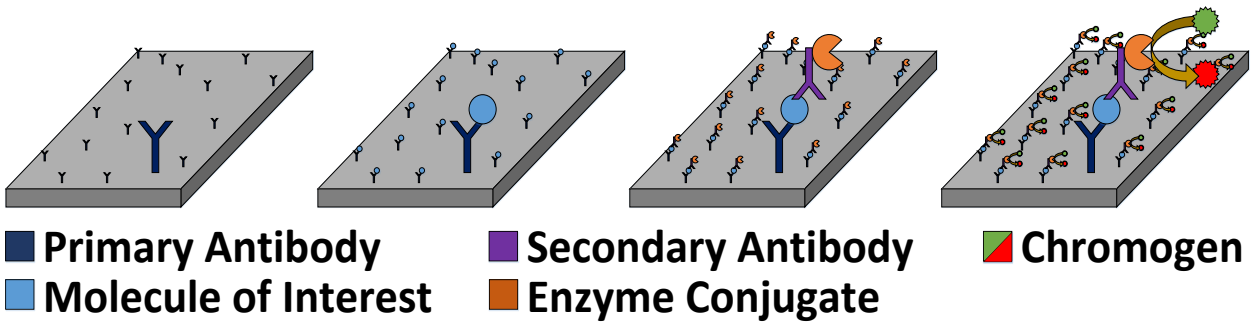

Figure 2.3. Schematic of an ELISA Procedure. On a biosensor, immobilized antibody binds to a molecule of interest, which is then targeted by a secondary antibody. The enzyme bound to this antibody catalyzes a color change of the chromogen, yielding a visible color in the solution which can then be quantified via spectroscopy.

Here we demonstrate the use of a smartphone to perform the readout and quantification of any ELISA assay and compare results with those obtained from a conventional laboratory ELISA microplate reader for two representative biomarkers. First, we demonstrate smartphone-based detection of a clinical biomolecule used for human disease diagnostics, IL-6. Second, we demonstrate detection of a peanut allergen, Ara h 1, in the context of a food safety application. Together, these biomarkers illustrate both the immediate utility and broad applicability of smartphone-based ELISA.

While there have been successful demonstrations of simplifying liquid handling steps[18-20] and both macro- and microfluidic sample collection techniques amenable to POCT,[21-24] high quality spectroscopic instruments have yet to be developed for on-site analysis. By providing a spectroscopic reader for ELISA tests that is integrated with a mobile communication device, this technology can be used with the myriad of existing, well-studied ELISA procedures that have been well characterized for wavelength-specific analysis. Combined with approaches for microfluidic-based automation of sample preparation procedures, the detection instrument presented here opens up the possibility of transferring ELISA-type tests to other fields requiring point of care analysis, such as quality control validation and agricultural monitoring.

The Cunningham lab is not unique in identifying the potential impact that a POCT device capable of performing immunoassays might have. POCT immunoassay have been around for many years, and are readily identifiable as part of everyday life. The most basic and prevalent form of POCT ELISA procedures would likely be a standard pregnancy test for human chorionic gonadotropin (hCG). These tests are completed on a paper membrane, and the colorimetric output is observed as a binary readout via visual comparison with a control band. More advanced versions

of ELISA as POCT have been demonstrated for a variety of conditions including tuberculosis,[25] HIV,[26] and Giardia infection.[27] While positive/negative results are acceptable for some types of diagnostic situations, often quantitative characterization of the amount of biological analyte is important within a specified range.

To this end, several different approaches have been taken. Paper-based microfluidic ELISA tests were demonstrated by the Whitesides group in 2004 that provide a quantitative measurement system based upon single-wavelength absorption.[28] This set of experiments is widely credited as the birth of paper microfluidics, a growing area of research for low-cost diagnostics. Aside from the custom-built illumination/sensor system used in that work, the most prevalent method for quantitative POCT ELISA measurement uses either a CMOS or CCD to directly image solutions, which has recently been shown to be successful on a smartphone platform.[29-32]

Systems such as these use various RGB color image weighting techniques to analyze concentrations of biological molecules of interest and therefore do not provide the spectrometric data required to perform a wavelength-based ELISA test. CMOS sensors, like those found in most smartphone devices, are wavelength-independent photon collectors that convert photons into RGB pixels via physical filters. These filters are comprised of colored dyes that each have both their own spectral response[33] and an additional infrared cutoff filter with a response that provides a sharp cutoff that can vary among batches of identical cameras by 10 nm.[34] In such a system, light intensity and color are intrinsically intertwined as they both rely on the number of photons captured by the RGB pixels compared with the number captured by those adjacent to them.

Spectrometers have been a cornerstone of modern analytical chemistry. The Beckman DU Spectrophotometer surpassed its contemporaries in popularity rapidly upon its invention, due largely to its increased spectral resolution across the entire range of measured wavelengths. They

present the standard laboratory tool for the measurement of a variety of experiments as they can provide wavelength-specific absorption information. The peaks at which a substance absorbs light the most correspond to chemical bonds and interactions at the molecular level, and can be used to identify specific components of a mixture. By dispersing the spectrum of absorbed light along one of the CMOS camera dimensions, we can decouple the wavelength from intensity and thereby determine the wavelength-specific absorbance of samples. This enables the accurate analysis of ELISA tests in a way that is immune to polychromatic spectral absorption variation.

2.3.1 Quantification of Absorption-Based Measurements

For the experiments in this section,[10] as the entirety of chromogenic spectral data for *3,3',5,5'* trimethylbenzidine (TMB) tests is captured solely in the blue channel of the RGB data, red and green channels are omitted from further calculation for ELISA-based measurements. To generate absorption spectra, converted vector forms of the data were subtracted from those of a blank comprised of deionized (DI) water, and normalized to the RGB response of the sensor when illuminated without sample or cuvette present in the optical path.

To best compare the smartphone measurement sensitivity with that of a commercially available microplate reader, absorption values at $\lambda = 450$ nm are interpolated from calibrated spectra. In addition, recognizing the potential value of the full spectral data for each sample, we calculate the integrative absorption from $410 < \lambda < 500$ nm (Figure 2.4). Finally, the ELISA microplate reader data is imported from the instrument, appropriately normalized with respect to the blank, and averaged across replicates.

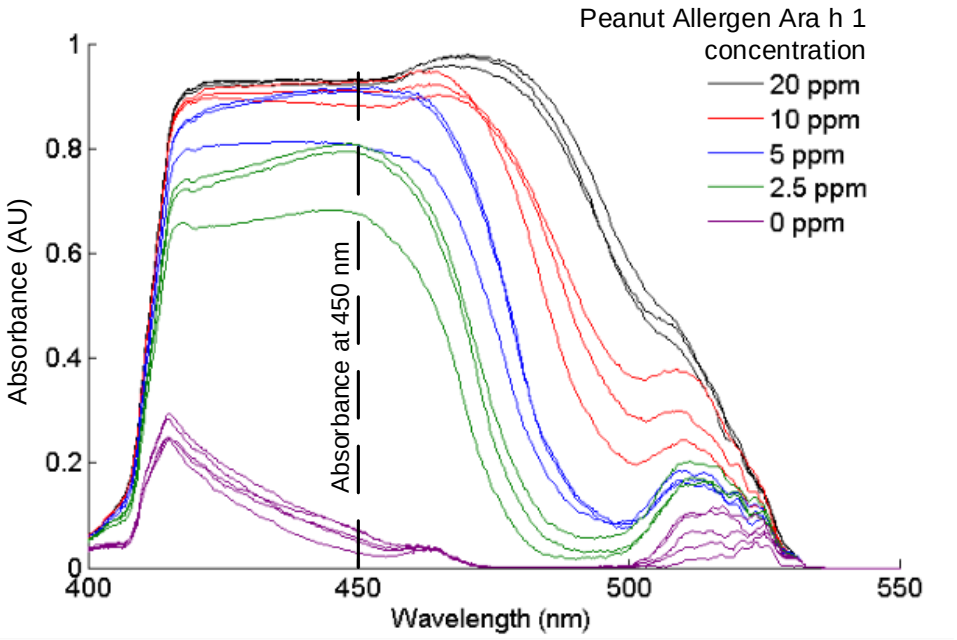

Figure 2.4. Example of Wavelength-Normalized Spectra Generated from Camera Images with Peanut Allergen Ara h 1. Five independent smartphone images were averaged, then normalized to a blank. Using lasers of known wavelength, images were converted to wavelength-dependent spectral absorbances. Five concentrations of peanut allergen Ara h 1 are present to illustrate the difference in absorption characteristics. The dashed line at λ=450 nm represents the single wavelength at which conventional ELISA measurements are taken using a microplate reader.

For each measurement method, the absorption as a function of concentration for the calibration standards is fit to a four-parameter logistic regression model based upon a sigmoidal response curve governed by

$$F(x) = D + \frac{A-D}{1+\left(\frac{x}{C}\right)^{B}} \qquad \text{(Eq. 3.1)}$$

where A is the minimum asymptote, B is the Hill's slope, C is the inflection point, and D is the maximum asymptote. While Beer-Lambert relations are often used to characterize absorption-based measurements, this logistic model was selected both on the recommendations of the assay protocols and to account for sensor saturation effects and polychromaticity for integrative absorption measurements.[35] Limits of detection are calculated as three standard deviations above the average zero-concentration value for each measurement method.

2.3.2 Human Interleukin 6 Quantification

Human Interleukin-6 (IL-6) is an important cytokine involved in the signaling cascade for the pro-inflammatory activation of B-cells following T-cell activation due to an antigen-mediated immune response. Elevated expression of IL-6 in serum samples has been demonstrated as an important indicator in conditions ranging from diabetes to postoperative surgical stress.[36-38] Additionally, IL-6 has been shown to be a relevant cancer biomarker important for the tracking, classification, and prognosis of various cancers including breast, hepatic, prostate, and renal varieties.[39-42]

A commercially available ELISA kit was purchased (Invitrogen) for the quantification of human IL-6. Lyophilized IL-6 was reconstituted in standard diluent buffer, and serially diluted to concentrations of 512, 128, 32, 8, 2, 0.5 and 0.125 pg/mL. Standards were added to pre-prepared wells with immobilized anti-IL-6 antibodies in replicate (n=6). A blank well was incubated with only diluent buffer. Biotinylated anti-IL-6 antibody was added to each well, and the solutions were allowed to incubate, covered, for 2 hours at room temperature on an orbital shaker (100 rpm). Solutions were removed, and the wells were rinsed (4x) with the provided wash solution, per assay instructions. Streptavidin-HRP solution was added to each well, and the plate was returned to the shaker for another 30 minutes. Another wash step was completed as before, and 100 µL chromogen solution (TMB) was added to each well. The plate was then incubated for 10 minutes in the dark, before applying 100 µL of the provided stop solution.

Using a commercially available ELISA microplate reader (BioTek Synergy HT), the completed assay was measured for absorbance at 450 nm, and blanked against the control well. Afterward, samples were individually transferred to polystyrene cuvettes that were

placed in a cuvette holder fixed permanently in the optical path to minimize variation due to geometric inconsistencies. A cuvette filled with 200 µL deionized water was used to normalize the RGB intensity values during image post-processing.

After data processing, the captured images were converted to absorption spectra that show clear concentration dependence across a range of wavelengths from 400 to 550 nm. From these spectra, either single wavelength measurements, akin to a microplate reader, or integrative absorption measurements can be calculated. After digital data analysis, IL-6 concentrations were observed to follow a sigmoidal dose-response curve, as expected (Figure 2.5). From the data collected, it can be observed that the smartphone-based absorption at 450 nm replicates the microplate reader measurements throughout the entire range of concentrations, validating our instrument as a portable, low-cost alternative to traditional benchtop apparatus. The integrative absorption has the same characteristic shape, and has a comparable Limit of Detection (LOD) lower than the minimum assayed concentration of .25 pg/ml. Validation of these techniques using the results from the traditional microplate reader via Bland-Altman analysis are discussed in Section 3.6.

2.3.3 Peanut Allergy Detection

The Ara group of peanut proteins consist of those that elicit allergic responses. While the specific proteins that an individual might be allergic to might vary, between 70 % and 90 % of individuals allergic to peanut products produce an immune response to the proteins Ara h 1, Ara h 2, and Ara h 6, a homolog for Ara h 2.[43] In the US, over 1% of the

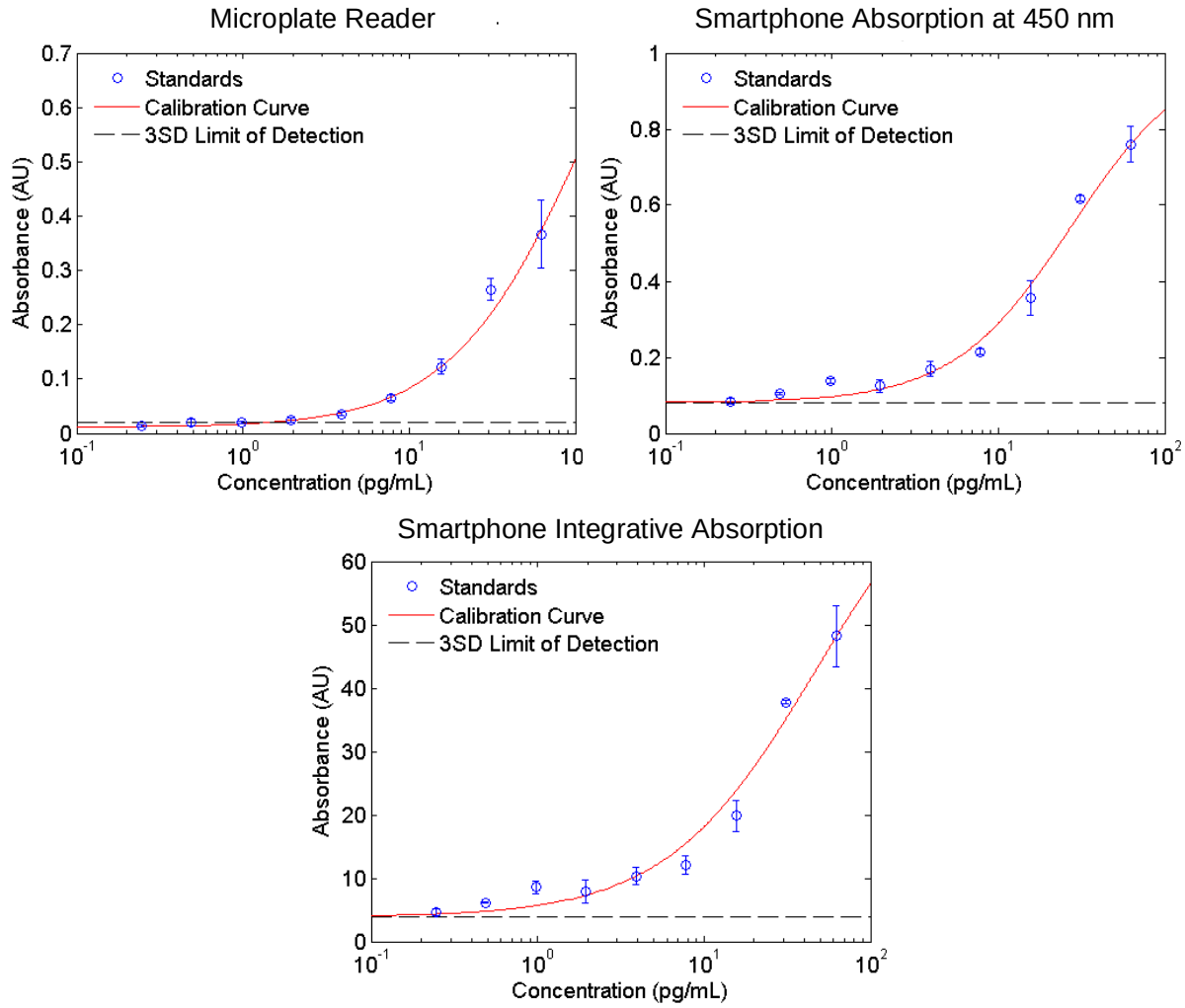

Figure 2.5. Concentration Dependence of Human IL-6. Samples were measured by an ELISA microplate reader, and then transferred to cuvettes to be measured by the smartphone instrument. Concentrations ranging from 0.25 pg/mL to 125 pg/mL were measured (n=2) along with a 0 pg/mL control (n=3). Calculations of the data collected by the smartphone were completed both at 450 nm, so as to be directly comparable to conventional ELISA data, and as the integrative absorption from 410 <λ< 500 nm. Limits of detection were calculated as three standard deviations above the 0 concentration measurement average.

population has a self-reported peanut allergy, and this rate seems to be increasing in children.[44] While many precautions exist to assist those with severe allergies to avoid peanut-based products, there is an increasing trend in the number of peanut allergy-related hospitalizations each year.[45] There is a high potential value in a portable smartphone-based test for peanut allergens present in food, but careful quantification is absolutely essential. To our knowledge, this work presents the first proof-of-concept of a portable peanut assay

that is capable of measuring peanut at concentrations less than the smallest measured No Observed Adverse Effect Levels (NOAELs).

A commercially available ELISA kit was purchased (R-Biopharm) for the quantification of peanut allergens Ara h1. Samples were taken from cookies purchased at two local bakeries, Insomnia Cookies and Schnuck's Grocer, as well as from pre-packaged vanilla Oreo® cookies. Samples were extracted per kit instructions: 1 gram of each cookie sample was ground and placed in a solution of extraction buffer diluted from the provided 10x concentrate. Extraction was completed at 60^{o}C for 10 minutes, followed by a 10-minute centrifugation at 2,500 g. The supernatant was then incubated, along with calibrated concentrations of peanut solution, in 400 µL wells with immobilized anti-Ara h 1 antibodies in triplicate. Enzyme conjugate, chromogen, and stop solutions were then added for 10 minutes each, with a 3x wash step in between. The entire process can be completed in under an hour.

The same preparation protocol developed for the IL-6 assay was again used for the Ara h 1 assay. The spectra were normalized to a water-filled cuvette during post-processing, and positioning was repeated. Lasers were used to recalibrate, and samples were measured in a similar fashion. After digital data analysis, standard Ara h 1 concentrations were also observed to follow a sigmoidal dose-response curve (Figures 2.6, 2.7). The limits of detection for the reported peanut assays were between .09 and .56 ppm. Once again, comparative validation was completed with a microplate reader via Bland-Altman analysis. Samples from peanut-containing cookies were found to have absorbances over that of the maximally assayed standard concentration (20 ppm), and so could not be

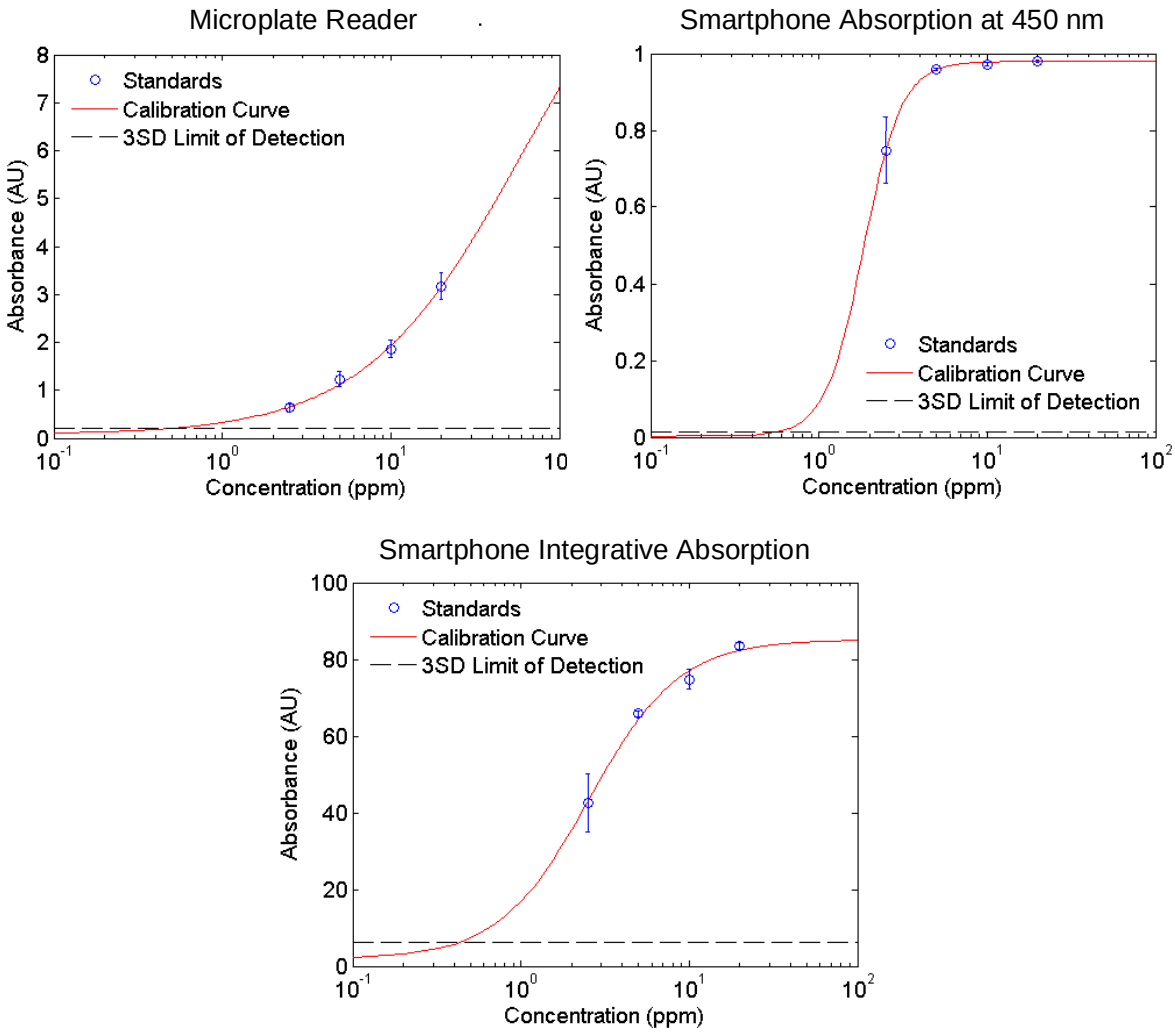

Figure 2.6. Concentration Dependence of Ara h 1. Samples were measured by an ELISA microplate reader, and then transferred to cuvettes to be measured by the smartphone instrument. Concentrations ranging from 2.5 ppm to 20 ppm were measured along with a 0 ppm control (n=3). Calculations of the data collected by the smartphone were completed both at 450 nm, so as to be directly comparable to the output of the ELISA microplate reader data, and as the integrative absorption from 410 to 500 nm. Limits of detection were calculated as three standard deviations above the 0 concentration measurement average.

quantitatively measured without further dilution. While neither Insomnia nor Schnuck's claimed that their sugar cookies were safe for consumption by people with severe peanut allergies, the sugar cookie from Schnuck's did, in fact, have an absorbance less than the assayed limit of detection (Figure 2.8). As expected, prepackaged sandwich crackers without a label indicating a risk of nut contamination tested below the assay LOD.

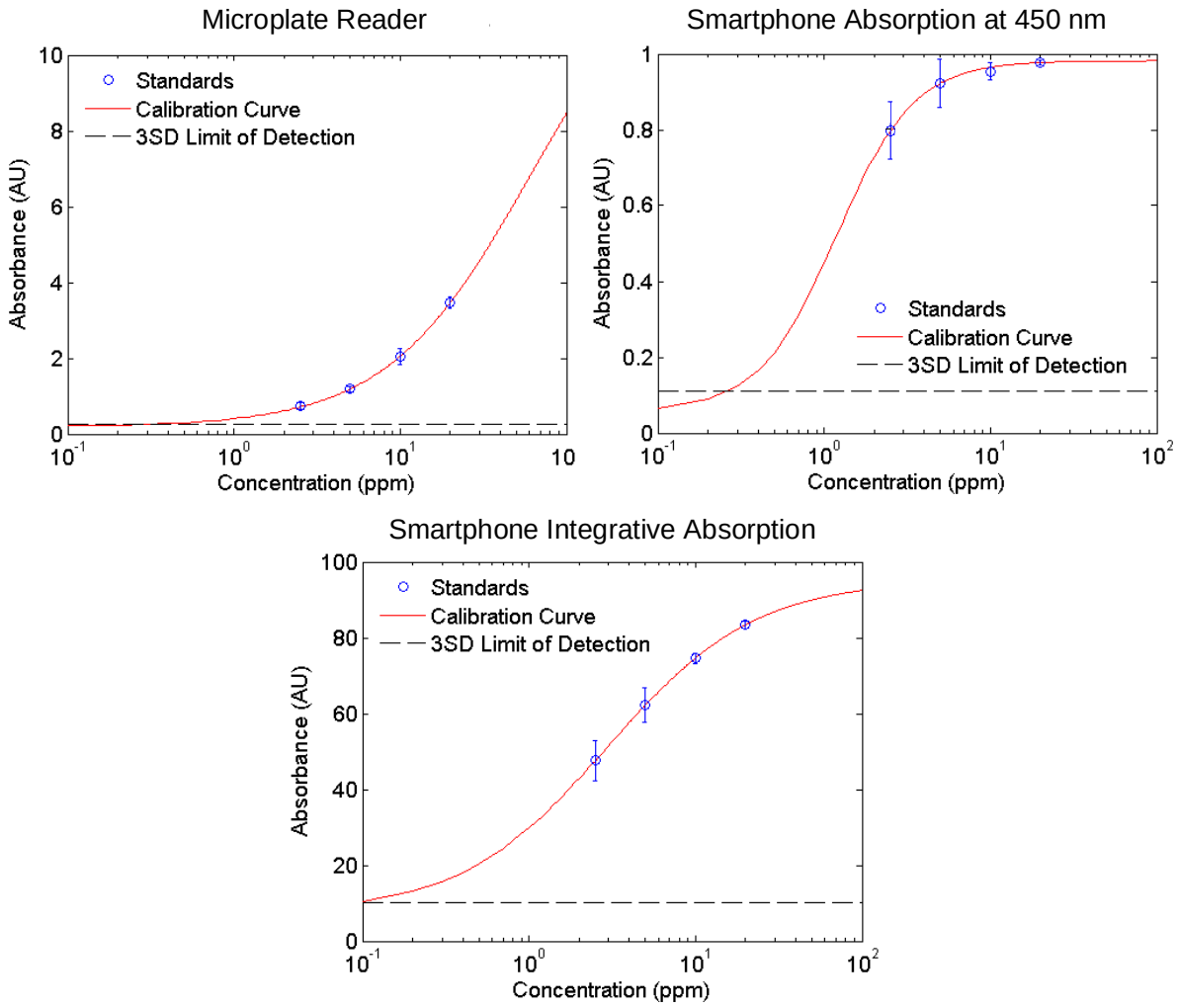

Figure 2.7. Second Experiment of the Concentration Dependence of Ara h 1. Samples were measured by a conventional microplate reader, and then transferred to cuvettes to be measure by the smartphone biosensor. Concentrations ranging from 2.5 ppm to 20 ppm (n=3) were measured along with a 0 pg/mL control (n=5). Calculations of the data collected by the smartphone biosensor were completed both at 450 nm, so as to be directly comparable to the output of a commercially available ELISA microplate reader data, and as the integrative absorption from 410 to 500 nm. Limits of detection were calculated as three standard deviations above the 0 concentration measurement average.

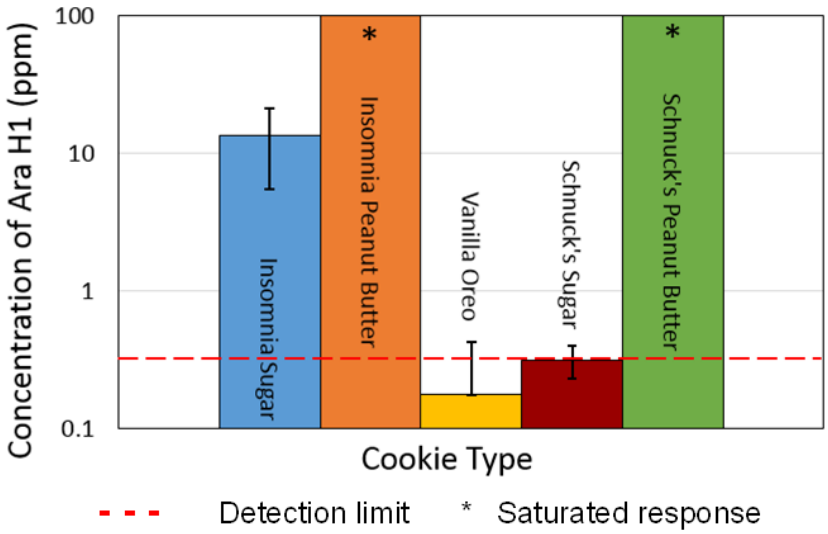

Figure 2.8. Quantification of Ara h 1 in Cookie Samples from Two Local Bakeries. Sample cookies were collected and contained separately in plastic to avoid cross-contamination. Samples were measured, ground, and proteins were extracted following manufacturer protocol. Vanilla Oreo® samples (n=3) and Schnuck's cookie samples (n=2) were assayed with data in Figure 5, and Insomnia cookies were assayed with data in Figure 6 (n=3). As the cookies were run on two different assays, only the higher LOD is shown.

* Peanut Butter cookies had concentrations of Ara h 1 higher than the maximum assayed standard concentration, so significant dilution would be required for accurate quantification.

2.3.4 Comparison of Smartphone Sensitivity and ELISA Microplate Reader

For each sample measured in the conventional microplate reader, a spectrum was generated from a series of 5 collected images. Both the absorption at λ=450 nm and the integrative absorption from λ=410 to 500 nm were calculated. All data points were fit with the same four-parameter logistic model described above. From the data collected, the absorptive LOD from either sensing modality appear to be in rough concordance, whereas the LOD obtained using the integrative absorption method is consistently 2-3x lower (Table 2.1) than that obtained by considering the absorption of only a single wavelength. This suggests that by taking advantage of the full spectral profile of the absorption peak resulting from the chromogen, it is possible to achieve a higher sensitivity than that obtained by observing a single wavelength. The availability of the full spectral absorption information

also enables the system to easily function with a broad range of chromogens that generate different colored solutions.

	ELISA Microplate reader	**Smartphone Absorption at 450nm**	**Smartphone Integrative Absorption**
Experiment 1	0.314 ppm	0.268 ppm	0.107 ppm
Experiment 2	0.529 ppm	0.560 ppm	0.269 ppm

Table 2.1. Comparison of detection limits of the Ara h 1 ELISA microplate reader, smartphone absorption at λ=450nm, and smartphone integrative absorption

In the realm of clinical medicine, the appearance of agreement between measurement techniques is not sufficient to support the adoption of a new instrument. In the field of diagnostics, understanding the agreement between the new device and the current gold-standard is both important and non-trivial. Recognizing that even gold-standard techniques have inherent measurement uncertainty; a simple correlation analysis will not accurately reflect the combined uncertainties. To address this issue, Bland and Altman developed a methodology that has become widely accepted as a viable technique, based upon the average measurements of the two techniques and the absolute differences at those averages.[46]

As ELISA absorbance measurements often have a lognormal distribution, a variation on the standard method using the geometric mean and log difference was applied to all non-zero values for each assay (Figure 2.9).[46-48] The log differences showed a dependence on the magnitude of the measurement, so a regressive approach was used to

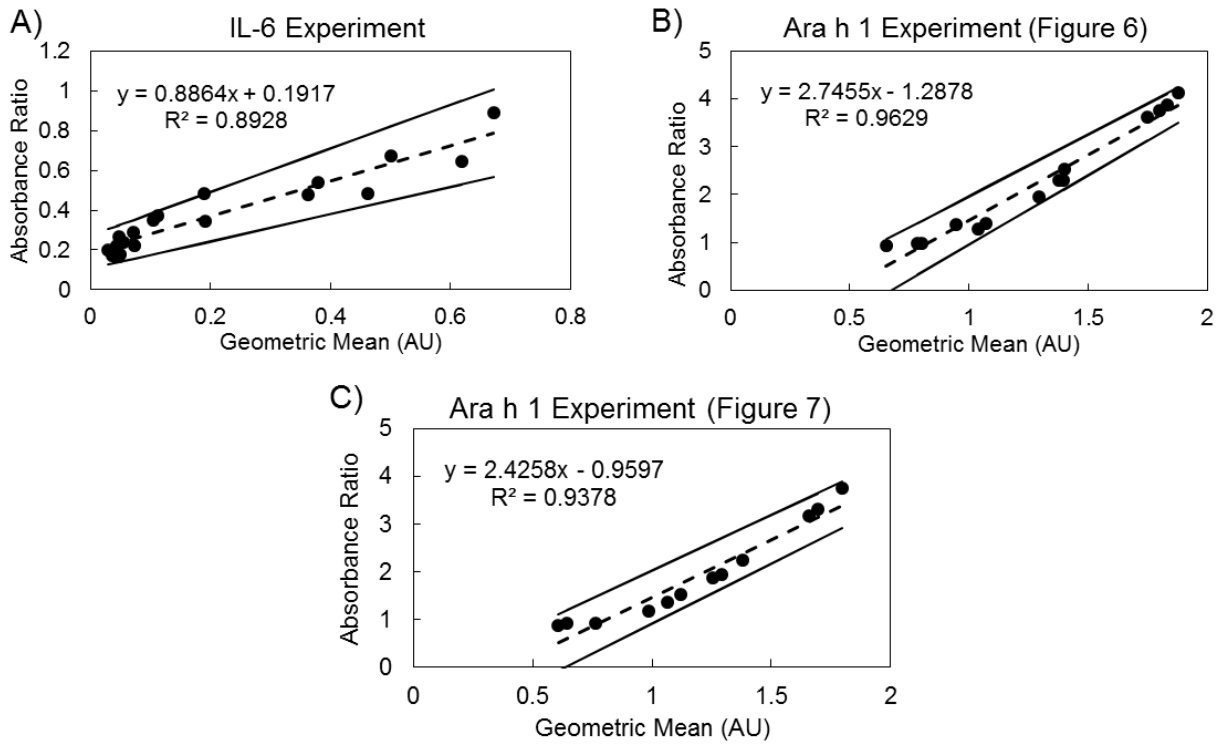

Figure 2.9. Validation of Smartphone Measurement Technique versus Microplate Reader via Bland-Altman Analysis. The lognormal quality of ELISA absorbances dictated the use of the geometric mean vs. log difference plot shown. All nonzero points are plotted, with the dashed line being the mean of the primary linear regression. Solid lines represent the 95% confidence limits of agreement, which contain all but one data point across the three separate experiments.

model the relation so appropriate limits of agreement could be attained.[49] The regression was modeled as

$$\hat{y} = b_0 + b_1\hat{x} \quad \text{(Eq. 2.1)}$$

where $\hat{x}$ is the vector of the geometric means of the two measurement techniques, $\hat{y}$ is the vector of absolute log differences, and b_0 and b_1 are the intercept and slope, respectively. For all three experiments, this provided a viable fit for the data; however, it was still necessary to see if the dependence on measurement magnitude continues into the residuals which are given by

$$r = c_0 + c_1 x \quad \text{(Eq. 2.2)}$$

where r is the vector of residuals, and c_0 and c_1 are the slope and intercept for the residual regression. The R^2 value for the IL-6 assay residuals was significant at .224, while the

values for the two Ara h 1 experiments were between .02 and .06. As the relationship between the residuals and magnitude of the measurement was found to be significant in at least one of the experiments, the model of the residuals was combined with the first model to provide the 95% limits of agreement. Assuming that these residuals follow a normal distribution, the limits of agreement can be calculated by combining Equations 3.1 and 3.2 as discussed by Altman:[50]

$$\widehat{a_1}, \widehat{a_2} = b_0 + b_1\hat{x} \pm \sqrt{\pi/2} * (c_0 + c_1\hat{x}) \quad \text{(Eq. 2.3)}$$

where a_1 and a_2 are the 95% limits of agreement. Of all data points assayed, only one point was found to be outside the ±1.96 S. D. limits of agreement (solid lines). These data demonstrate a high level of consistency between the conventional ELISA microplate reader and the smartphone-based spectroscopic absorbance measurements.

2.3.5 Discussion

The diagnostic potential for biomarkers such as IL-6 is significant. Tracking the post-operative serum levels of biomolecules to assess the chances of post-operative complications could potentially increase positive outcomes for those patients via early-detection,[38] and decrease required post-operative in-hospital recovery time. While long-term monitoring of biomarkers could likely provide valuable prognostic information, the associated load on hospitals and diagnostic laboratory facilities make any such testing at best expensive, and at worst, unrealistic. Similarly, the measurement of cancer-related biomarkers might prove a useful tracking mechanism for potential relapse or metastatic risk.[51] The development of a cheap yet reliable ELISA reader could facilitate the development of a broadly available test in clinic-type environments.

In contrast with medical diagnostic assays, allergen detection provides a consumer-based testing opportunity. While existing microplate readers are prohibitively expensive for individuals and designed specifically for laboratory settings, a handheld smartphone attachment is naturally amenable to an in-home testing environment. Though ELISA assays require multiple liquid-handling steps, there have already been several successful demonstrations of ELISA performed as a lab-on-a-chip technique that could be integrated into a low cost, disposable cartridge, readily read by an instrument such as the one described here. While significant work has gone into simplifying both the sample collection process and the liquid handling steps used in a traditional ELISA test, there is still a need for an instrument that can replicate the accuracy and repeatability of a microplate reader in a point-of-care system.

Current alternatives for assay readout are based on either visual inspection or non-spectral image analysis, neither of which provide the spectral resolution of traditional microplate readers. ELISA testing is dependent on this spectral resolution, as the chromogens that are being measured are characterized by non-uniform absorption spectra in the visible range. Non-spectral methods of color analysis are subject to the variations in intensity present across various wavelengths, usually binned into three RGB channels via a Bayer filter. By diffracting the wavelength of transmitted light along one of the physical dimensions of the CMOS sensor, we are able to separate the intensity information of the absorbed light from its wavelength, thereby allowing for the wavelength-specific quantification of chromogenic absorption. Furthermore, our technique is broadly applicable across all visible wavelengths of the spectrum, even in regions where RGB channels sometimes overlap, including both 450 and 492 nm, wavelengths where the

important ELISA chromogens TMB and OPD maximally absorb, and where RGB analysis cannot suffice.

While there is general consensus on the importance of minimizing peanut material in non-peanut-containing foods, surprisingly little work has been done to quantify the amount of peanut protein required to produce an allergic reaction in affected individuals. Literature review-based statistical modeling has produced a starting point for such efforts, but variations in testing modalities as well as an abundance of situations where NOAELs could not be determined due to observed allergic responses at the lowest assayed dosage have resulted in a large number of patient results being excluded.[52,53] One of the most promising studies of existing data was collected from clinical records of patients being tested, rather than from specific patient-recruited studies, which yielded an eliciting dose in 5% of the population (ED_5) of 4.2 mg peanut protein.[52] While there is uncertainty in some of the numbers prevalent in the literature, the overall range of subjective NOAELs reported (or estimated) is typically between .4 and 10 mg protein,[52,54-56] with objective ED_5 have been estimated as low as 1.5 mg.[57] For a reasonable maximal daily intake of 500g of food based upon a 2000-3000 calorie diet, this would translate to .8 and 3 ppm peanut protein for minimum reported NOAEL and ED_5, respectively, which are higher than the LOD for each of the testing methodologies used. Thus, we have successfully demonstrated a point-of-use testing modality that can plausibly be used to measure clinically relevant amounts of peanut.

While this set of experiments has focused upon the demonstration of a liquid-based color absorption assay in the context of an ELISA, the approach demonstrated here may be applied to any assay that results in the color change of a liquid. Colorimetric tests are

relatively common due to their ability to be qualitatively measured via visual inspection. Such tests are commonly used in testing liquids for pH, chlorination, and contaminants ranging from metals to organic material. While qualitative information is useful, spectroscopic analysis can provide quantitative information that is consistent across phone manufacturers and independent of operator or hardware-based differences, a significant improvement over both visually comparative methods and non-spectrally resolved imaging methods. Broadly, this instrument can perform any such test, assuming the absorption spectra exists within the visible range of wavelengths.

2.4 Label-free Biodetection using Photonic Crystal Sensors

While spectroscopic biological assays such as ELISA can be used for the detection of many biological analytes, their widespread adoption into scenarios outside the laboratory is hindered by the complexity of the assay protocol which often involves multiple liquid handling steps and conjugated antibodies.[58-61] Detection of an analyte via one of its intrinsic physical properties (dielectric permittivity, mass, conductivity, or Raman scattering spectrum – for example), called "label-free" detection,[62-64] is preferable for assay simplicity in terms of the number of reagents required, washing steps needed, and assay time.

Of all the label-free detection approaches that have been demonstrated, those based upon optical phenomena have been commercially preferred due to a combination of high sensitivity, low sensor cost, detection system robustness, and high throughput capacity. Adsorption of biomolecules, viral particles, bacteria, or cells onto the surface of an optical biosensor transducer results in a shift in the conditions of optimal optical coupling, which can be measured by illuminating the transducer surface and measuring a property of the reflected or transmitted light. Such a detection approach is robust, and has become economically advantageous due to the advent

of low cost light emitting diodes and semiconductor lasers. Surface plasmon resonance (SPR) based biosensors[65-69] and photonic crystal (PC) optical biosensors[70-75] are capable of detecting broad classes of biological analytes using their intrinsic dielectric permittivity. Each approach has been demonstrated using both large laboratory instruments and miniaturized (shoebox-sized) systems. However, no prior label-free optical biosensor instrument has been fully integrated with a smartphone, using the onboard camera itself as the detection instrument.

Here, we demonstrate the use of a smartphone to detect shifts in the resonant wavelength of a PC-based label-free biosensor. PC biosensors are amenable to readout by a smartphone, as they function as narrow bandwidth reflection filters that can be measured by illuminating them at normal incidence with collimated white light. The PC used in this dissertation was designed to produce a high efficiency resonant reflection at a wavelength in the visible spectrum (λ= 565 nm) in air. Adsorption of biomolecules on the PC surface results in a red-shift of the resonant peak. To enable the rear-facing smartphone camera to measure this resonant peak, we use a setup very similar to that used for absorption measurements. While the phone and the optical components are held in position, the PC sensor itself may be inserted and removed from a narrow slot within the cradle. Importantly, the system incorporates the ability to compare wavelength shifts from adjacent "active" and "reference" regions of the PC as a means for incorporating an accurate experimental control. To demonstrate operation of this sensor and detection system, we will analyse the concentration dependence of the Protein A-porcine IgG interaction.

2.4.1 Background on Photonic Crystals

Photonic crystals (PCs) comprise a broad class of optical structures that are composed of a subwavelength periodic modulation of refractive index. While these modulations have been

demonstrated in two and three-dimensional structures, this dissertation, both here, and in Chapter 5, will focus on specific applications of the simplest case: the 1-dimensional periodic grating.

As described in previous publications,[76,77] these gratings can be easily manufactured via nanoreplica molding in a UV-curable polymer on a disposable plastic substrate. Upon curing, this then provides a grating structure of the desired height, width, and period over which subsequent depositions of specific thicknesses of dielectrics can be made. For these experiments, SiO_2 and TiO_2 were used for low- and high-refractive index materials, respectively.

When collimated light is incident on the grating structure, a portion of the light is diffracted by the high-refractive index TiO_2 layer in a wavelength- and angle-dependent manner, according to the grating equation:

$$\Lambda(\sin(\theta_i) - \sin(\theta_d)) = n\lambda \qquad \text{(Eq. 2.4)}$$

where Λ is the grating period, n is the diffraction order, λ is the wavelength of light, and θ_i and θ_d are the incident and diffracted angles, respectively. Much of the light passes through without diffraction ($n = 0$), but some of the light undergoes first-order diffraction, which at normal incidence conveniently simplifies to

$$\sin(\theta_d) = -\frac{\lambda}{\Lambda} \qquad \text{(Eq. 2.5).}$$

Periodic waveguides such as this have been shown to have a specific resonance condition where the first-order diffracted light propagates as a guided mode due to total internal reflection when

$$2k_3 d + 2\Phi_{1,2} + 2\Phi_{2,3} = 2\pi m \qquad \text{(Eq. 2.6)}$$

where $k_3 = 2\pi/\lambda$ is the wavevector of the light perpendicular to the grating in the SiO_2, d is the thickness of the grating, m is the order of diffraction and $\Phi_{1,2}$ and $\Phi_{2,3}$ are the Fresnel coefficients

due to differences in refractive index between the waveguide (SiO_2) and surrounding layers.[78] At each interface of the waveguide that the internally refracted light hits, a portion of the light is refracted back out of the grating. Light that undergoes two instances of internal refraction before escaping the grating is angularly aligned with light that simply passed through the grating, but it has undergone a phase shift relative to its non-diffracted counterpart, resultant from the Fresnel coefficients of reflection and diffraction and the difference in path length, which is given by

$$\Phi = 2k_3 d + 2\Phi_{1,2} + 2\Phi_{2,3} + \pi \qquad \text{(Eq. 2.7)}$$

It is important to note that this path length difference results in the twice-reflected and non-reflected light being exactly π out of phase, yielding complete destructive interference.[79] Similarly, light that undergoes a single internal refraction before escaping the waveguide can be shown to completely constructively interfere, yielding effectively 100% reflection.

Assuming constant perpendicular illumination, the only factors that affect this resonant wavelength are the Fresnel coefficients, which are dependent on the relative refractive indices of the grating and waveguide layers. As biomolecules attach to the exposed surface of the PC, the effective refractive index of the TiO_2 is slowly increased in a quantifiable manner, which serves as the foundation for label-free quantification of biomolecular attachment (Figure 2.10). The Cunningham group has utilized this technique for a variety of analytes, including pancreatic cancer cytotoxicity screenings,[80] the presence of porcine rotavirus in biological samples,[81] and HIV viral load.[82]

2.4.2 PC Characteristics for Smartphone Biosensing

For these experiments, a one-dimensional grating structure was created on a disposable plastic substrate in UV-curable polymer via nanoreplica molding. As depicted in Figure 10, the

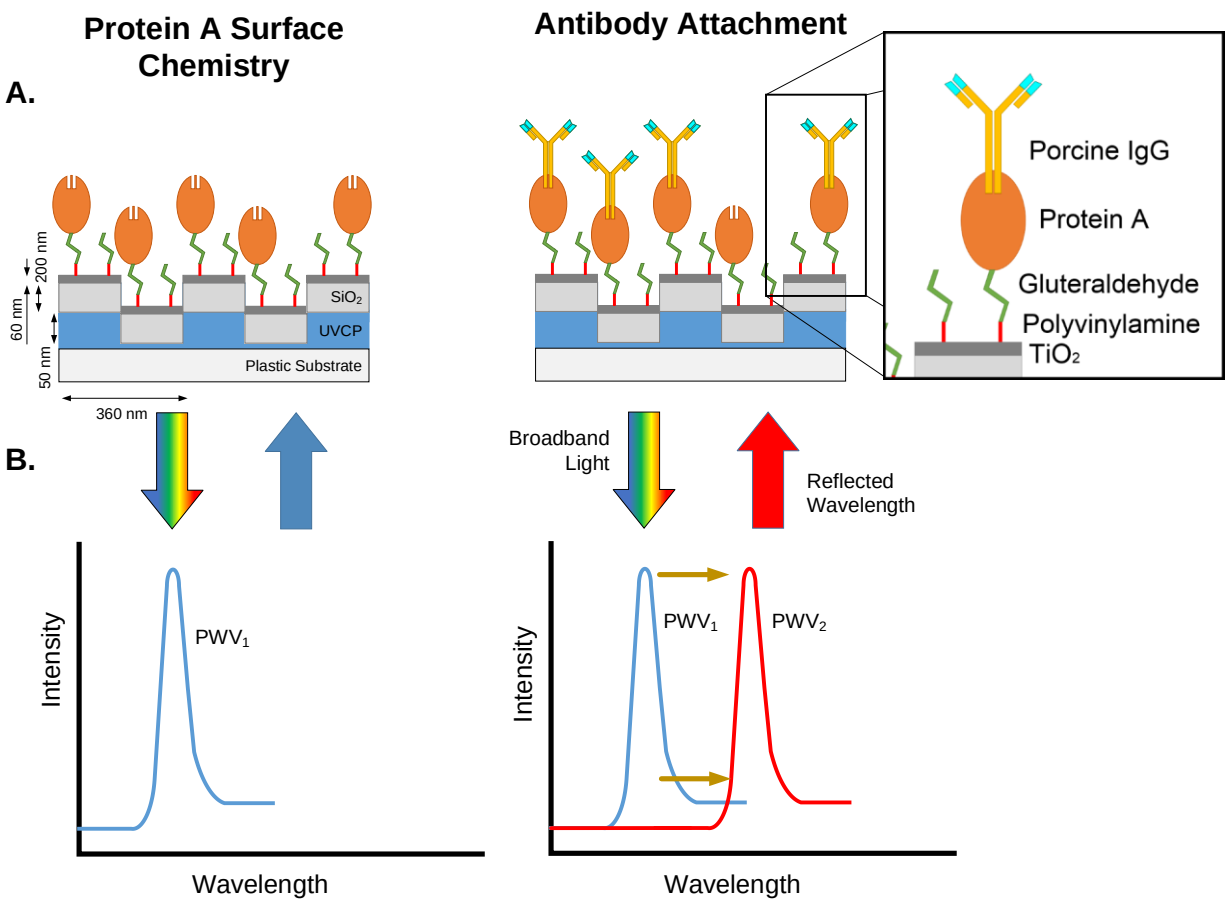

Figure 2.10. A. The nanopatterned PC biosensor surface is functionalized via PVA and glutaraldehyde surface chemistry to facilitate the capture of IgG molecules**. B.** The associated PWV undergoes a red-shift when antibodies attach to the surface and increase the effective refractive index of the TiO2 layer.

PC grating period was 360 nm and the depth was 60 nm. The polymer grating was subsequently over-coated with sputtered thin films of SiO_2 (t = 200 nm, refractive index = 1.54) and TiO_2 (t = 60 nm, refractive index = 2.35). After fabrication, the flexible plastic substrates were attached to standard 25 by 75 mm glass slides using double-sided, pressure-activated adhesive film. The grating dimensions and thin film thicknesses were designed to provide a 95% efficient narrowband reflectance with a central wavelength of $\lambda = 565$ nm and a resonance bandwidth (full width at half-maximum: FWHM) of $\lambda \sim 5$ nm when the surface of the PC is dry. Adsorption of biochemical molecules onto the surface of the PC results in an increase of the effective refractive index of the high refractive index waveguide layer, yielding a positive shift in the peak wavelength value (PWV) of the narrowband maximum of reflection efficiency (measured as a minimum in

transmission efficiency by the smartphone).[70] The magnitude of this shift can be directly correlated to the quantity of IgG present on the PC surface.

2.4.3 Measurement Protocol

To perform a label-free biological assay, the PC is initially prepared by immobilizing a capture molecule (such as an antibody, aptamer, or single-strand DNA sequence) that selectively recognizes the analyte in a test sample. The sensor surface is further prepared with a "blocking" step that prevents nonspecific adsorption of other molecules. The PWV of the sensor is measured prior to the addition of the target analyte to establish a baseline reading. Exposure of the sensor to the test sample results in adsorption of the analyte on the PC, which is followed by rinsing/drying the sensor to remove unbound molecules. A second PWV measurement is then taken and the difference in PWV is recorded as the shift due to the adsorption. The basic approach outlined in this protocol can be augmented by the incorporation of positive and negative experimental controls, including the use of a "reference" sensor that is prepared with an unmatched capture molecule, but still exposed to the test sample. Although all measurements reported here were taken with the PC surface in a dry state, the system could be further modified via the incorporation of a static liquid chamber or flow cell with the PC, so that the PWV shifts can be monitored kinetically.

2.4.4 PC-based Biodetection with a Smartphone

To demonstrate the ability of the sensor and detection instrument to perform a biodetection assay in which a layer of immobilized capture molecule is able to selectively capture a specific biomolecule of interest, we captured porcine immunoglobulin G (IgG) using an immobilized layer of Protein A. While not in the realm of the biotin-streptavidin interaction, Protein A/G-antibody reactions are some of the stronger interactions observed in physiological conditions.

To begin, the PC sensor was functionalized with an aldehyde-based surface chemistry to facilitate the attachment of Protein A. To prepare the surface for functionalization, the PC slide was thoroughly cleaned using an acetone/IPA/DI-H_2O wash, and then functionalized with a 10% solution of polyvinylamine in water at 40^o C for two hours. It was then washed 3x in ultrapure water, and incubated in a 25% solution of glutaraldehyde in water (Sigma Aldrich) for 4 hours at room temperature. After a subsequent 3x wash in ultrapure water and drying of the sensor surface, the PWV from 14 distinct locations on the functionalized PC surface were recorded by the smartphone detection instrument to establish the baseline PWV upon which subsequent wavelength shifts caused by the attachment of capture and target molecules would be compared.

Next, a custom-made polydimethylsiloxane (PDMS) gasket was adhered to the PC sensor surface to form 14 separate assay wells (diameter = 6 mm) over the 14 measurement locations. Each well was incubated with 60 µL of 0.5 mg/mL Protein A in .01M phosphate buffered solution (PBS; pH= 7.4) for 20 minutes. After Protein A immobilization, the wells were washed with PBS, the gasket was removed, and the PC sensor was dried. A second PWV reading was gathered from each location, in order to establish the PWV shift due solely to the attachment of the Protein A layer. Figure 2.11A shows the initial PWV associated with each of the 14 wells on a single PC

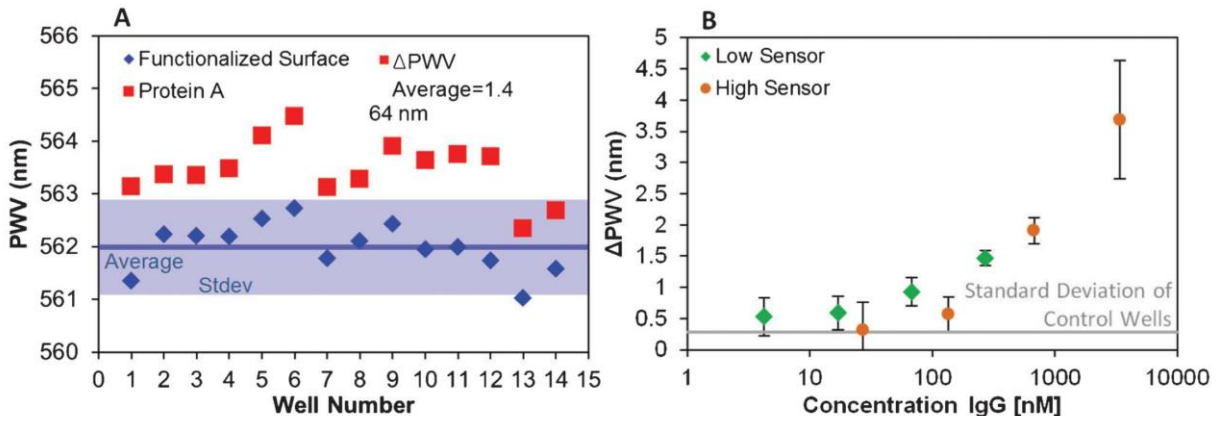

Figure 2.11. Concentration dependent PWV shift of porcine IgG antibody. A. Variation in slide functionalization versus Protein A deposition. **B.** Protein A was immobilized on two PC sensors to detect concentrations of porcine IgG antibody present in quantities between 1 nM and 5000 nM. N = 3 for assay wells; N = 2 for control wells.

sensor, and the PWV shift induced at each location by Protein A deposition, demonstrating the initial variability induced by the PC functionalization (average PWV = 561.99 nm, stdev = 0.464 nm), and the PWV shift induced by the Protein A deposition process (average ΔPWV= 1.46 nm, stdev = 0.288 nm). These results demonstrate that the surface chemistry for protein attachment used here introduces a greater degree of variability than the variability of the subsequently observed sensor measurements from the smartphone instrument.

Prior to the exposure of the PC sensor to the IgG analyte, the gasket was replaced, and the PC was rehydrated with 60 µL PBS in each well for 10 minutes. After aspiration, 60 µL of porcine IgG solutions were added to each well at concentrations ranging from 4.25 nM to 3.4 µM (Figure 11 B) and incubated for 10 minutes. After a rinse with 0.01 M PBS to remove unbound antibody, the PC sensor was dried and measured using the smartphone to calculate the ΔPWV induced by IgG attachment. Concentration-dependent PWV shifts were observed, with each IgG concentration being measured in triplicate. Intra-sensor variability is low (average stdev for triplicate measurements was 0.335 nm). The lowest IgG concentration tested (4.25 nM) was observable above the negative control (0 nM IgG), indicating the ability to clearly measure wavelength shifts of 0.16 nm above sensor-specific background noise on that sensor (data not shown) that is limited by assay-related variability, rather than by the wavelength shift resolution of the detection instrument. Despite its compact size and simplicity, the detection instrument can detect the presence of analytes in the nM concentration range with a "direct" assay. The limits of detection of the system can be reduced further through the use of a variety of tags, such as secondary antibodies[83] or nanoparticles[84,85] that can amplify the wavelength shift by factors of 5 - 1000 x.

2.4.5 Discussion

For the practical utility of the apparatus, it is important for future versions of the smartphone biosensor to have the ability to use wet samples by allowing for the use of thicker cartridges comprised of 3D wells, as opposed to the current methodology of current limitation of working with planar slides. The decision to take measurements of the PC surface in a dry state was dictated by the desire to measure sensors in as simple of a manner as possible, without the possibility for bulk refractive index effects, or the incorporation of fluid flow (with associated pumps and valves) into the instrument. Detection in a dry state also allows for the assay steps to be performed separately from the detection step in both time and physical location, which would be desirable for several of the real-world detection scenarios being considered at that time. Incorporation of a microfluidic channel into the sensor through the fabrication of a more sophisticated cartridge would enable liquid-based detection and the potential for measuring the kinetics of analyte binding without altering the fundamental measurement approach, but was not addressed as a part of this work.

The experiments used to characterize the smartphone detection instrument presented in this paper serve to demonstrate the feasibility of measuring PWV shifts from a PC biosensor, rather than focusing on the application of the system to complex test samples that contain many potentially interfering compounds. To address this issue for such applications, it will be necessary to incorporate reference sensors that can serve as negative controls to the effects of nonspecific binding. Such methods, commonly reported in the biosensor literature, should include multiple types of negative controls. First, as shown in this chapter, a detection experiment should include a sensor that is prepared with the capture molecule, but that is exposed to buffer rather than to the test sample. Secondly, the experiment should also include a sensor that is prepared with a capture

molecule that does not recognize the analyte (such as an antibody for a nonrelated antigen), and exposed to the test sample. The combination of these two experimental controls can determine the mass density of analyte molecules that are bound nonspecifically to the sensor surface from a complex media, while at the same time taking into account common mode error sources such as temperature variability or bulk refractive index variability.

2.5 Conclusions

In this chapter, we have demonstrated two usage cases for a novel smartphone-based spectrometer: absorption measurements for use with standard ELISA procedures, and PWV measurements for use with photonic crystal based label-free assays. In the first part of this chapter I described the successful detection of human IL-6, an important cancer biomarker, and Ara h 1, one of the principle peanut proteins responsible for causing a reaction. Limits of detection were found to be comparable to those from the standard microplate reader, and the high level of agreement between the two sensing methods was demonstrated via Bland-Altman analysis. Finally, cookies from two local bakeries were tested for cross-contamination with peanut ingredients, and the instrument was demonstrated as a practical tool for detecting clinically relevant concentrations of allergen.

In the latter half of the chapter, the instrument was modified to provide polarized light which could be used to illuminate a photonic crystal at its resonance condition, providing a narrowband reflection phenomenon that redshifts as biomolecular adsorption takes place on the PC surface. As demonstration of its biological utility, the concentration dependence of the Protein A-IgG interaction was investigated. Concentrations of less than 1 μg/mL were successfully quantified.

Absorption measurements comprise a large portion of the canonical optical diagnostic methodologies. PC-based techniques, while significantly further behind in commercial development, offer several key benefits, namely the simplification of assay protocol due to their label-free nature. In between the two, though, sits an important body of work within the realm of optical biosensing that should be mentioned: fluorescence-based assays. There are a handful of interesting and useful diagnostic tests that can be completed with the use of fluorescent reporter probes including Förster resonant energy transfer, fluorescent lifetime, molecular beacon, and fluorescent polarization assays. This modality was integrated with our prototype system via augmentation with a few external pieces on an optical bench. One of the principle requirements of any fluorescent assay is the orthogonal illumination of the sample to minimize noise due to the light source in the fluorescent signal. With this modification, new types of assays were added to those demonstrated here, further expanding the capabilities that the instrument can provide in a point-of-care environment.

While expanding capabilities is important, ease-of-use and simplicity of design are two of the most important attributes for a POCT device. A single instrument that could be used without significant modification for absorbance, fluorescence, and PC-based measurements, would provide a great benefit for clinicians. In addition to simplicity of use, it would decrease the costs associated with the testing increase portability. In the next chapter, such a device will be described from initial design through proof-of-concept demonstrations.

CHAPTER 3: DEVELOPMENT OF A CONSOLIDATED TRI-ANALYZER FOR POINT-OF-CARE DIAGNOSTICS[1]

3.1 Introduction

To date, reported examples of smartphone-based IVD detection instruments are only capable of carrying out a single type of analysis, and with a few exceptions[9,86] are capable of very limited multiplexing of tests. Many laboratory-based microplate readers function as a "multi-mode" instruments. These systems can transition between spectrometric absorption analysis (as used in ELISA assays), fluorometric analysis (as used in molecular beacon assays, fluorescent polarization (FP) assays, and luminescence-based assays), and, in the case of one product (PerkinElmer EnSight) label-free optical biosensor assays. The ability of a detection system to easily transition between these modalities is a desirable one, as it enables the user to purchase only one instrument, and to use a common liquid handling format and software interface across a variety of applications. In the previous chapter, I demonstrated that optical paths designed with specific measurement modalities using the rear-facing CMOS sensor of a contemporary smartphone are capable of measuring biological analytes with comparable ranges and limits of detection to those of standard laboratory analyzers, and based upon those early experiments, I now seek to combine three of these application-specific devices into a more-universal point-of-care testing device.

In this chapter, I report, to my knowledge, the first example of a smartphone-connected detection instrument that can measure the output of three distinct spectral biosensing modalities using two separate yet complimentary light paths.[87] The three modalities represent a large fraction of all commercially available IVD tests for which a liquid sample changes color, or in which a

[1] This Chapter contains work previously published as outlined in both the Acknowledgements and References.

liquid sample generates light as a visible indicator of the test's outcome. The system is capable of performing spectral analysis of:

- **Optical Transmission** of light through a test sample at specific wavelength(s).This measurement modality is commonly used in ELISA assays, liquid phase plasmonic nanoparticle-based tests including surface plasmon resonance (SPR) and localized surface plasmon resonance (LSPR),[88-90] latex (or other nanoparticle-based) agglutination tests (LAT),[91] and transmissive surface-based SPR, LSPR, and photonic crystal (PC) based tests.[16,81,90] ELISA tests are a mainstay of contemporary biosensing tests, with ready-to-go kits available for thousands of different biological targets.
- **Reflectance spectroscopy** of light against a resonant optical transducer, as used in reflective label-free optical biosensing techniques such as SPR, PC, or reflectometric interference spectroscopy (RIFS). While these direct binding label-free approaches do not currently have commercially available assay kits associated with them, they have been applied to thousands of biological analytes due to their simplicity and speed.[92]
- **Intensity spectroscopy** from photon-generating assays such as those based upon fluorescence, chemiluminescence, bioluminescence or quantum-dot (QD) emission. A broad variety of biosensing assays have such a readout, including fluorescence or chemiluminescent immunoassays (FIA, CLIA), fluorescent polarization (FP), Forster resonance energy transfer (FRET) as well as several molecular diagnostics, including polymerase chain reaction (PCR) and related loop-mediated isothermal amplification (LAMP).

Together, we estimate that these modalities can perform the necessary spectral readouts of 90-95% of commercial immunoassays,[93,94] the exception being radioimmunoassays (RIAs). In

particular, as traditional ELISAs are being replaced by FIAs and CLIAs,[95] the ability to easily switch between measurement modalities makes this system capable of maintaining utility for a variety of applications, and a useful opportunity to potentially compare different tests for the same analyte on the same point-of-care device.

The Spectral Transmission-Reflectance-Intensity (TRI)-Analyzer takes advantage of the fact that all three modalities share the requirement to measure changes in the spectrum of light that is either absorbed, reflected, or emitted during the course of each type of IVD test. Our approach allows the user to select from one of two light paths: illumination of the assay with either the internal white LED of the smartphone that is typically used for "flash" exposure photography, or instead with an inexpensive green laser diode. Accurate spectral analysis is performed by collecting light from the assay into an optical fiber, whose distal end directs light through a diffraction grating into the smartphone's rear-facing internal camera. The optical components are arranged wholly within a 3D-printed plastic cradle, containing a slot through which an assay cartridge is inserted.

For many clinically relevant assays, multiple samples, replicates, positive/negative controls, and/or standard calibration solutions are required. Few smartphone-based sensing platforms have demonstrated this capability beyond taking pictures of multiple colored samples and performing RGB-based color processing. By converting the smartphone camera into a spectrometer, we lose the spatial discrimination that would allow simultaneous measurement of multiple samples. Instead, multiplexing is achieved using a cartridge comprised of a linear series of liquid compartments that slides through an opening in the back of the cradle. By pairing this linear motion with the smartphone's ability to capture video, the spatial dimension separating the liquid chambers in the cartridge can be reconstituted with video post-processing, allowing for the

rapid and user-friendly measurement of multiple samples with a single motion, similar to swiping the magnetic strip of a credit card across a magnetic read head.

Each sensing modality utilizes a unique cartridge configuration with the same overall form factor. Both Transmission and Reflection modalities rely on a bifurcated illumination-collection fiber optic assembly that allows light from the smartphone flash to pass through a transparent cartridge and reflect off a stationary mirror positioned within the cradle or interact with a PC biosensor that operates as a wavelength-selective resonant mirror at the cartridge's back wall, which is coated in an opaque dye to prevent reflection by the stationary mirror. The Intensity modality uses cartridges with a transparent bottom to allow for orthogonal fluorescent excitation of the sample chambers. All three modalities then collect the reflected light via the collecting fiber of the bifurcated fiber assembly which is then transmitted to the rear-facing camera of the smartphone.

Importantly, the detection approach enables the user to "swipe" the cartridge through the instrument while the smartphone records video at 60 frames/second, and software can identify the frames from the video that represent images gathered while the center of each chamber is aligned with the illumination/read head. Thus, the user is freed from the necessity of performing accurate alignment of the cartridge's liquid chambers within the instrument, and the cartridge can be read in a similar manner to the approach used for scanning a credit card past a magnetic stripe reader. Multiplexing in this fashion enables a single cartridge to contain experimental controls, replicates, and a series of active tests.

In this chapter, I demonstrate the Spectral TRI-Analyzer first for representative tests that verify its capabilities to measure liquid absorption spectra, PC biosensor resonant reflection spectra and fluorescence spectra. Then, using commercially available diagnostic assay kits for

colorimetric output (ELISA) and fluorescence output, we validate the instrument's two light paths and demonstrate that the Spectral TRI-Analyzer provides equivalent limits of detection (LOD) for reading the same assay with a commercially available 96-well microplate reader. While there exist many opportunities to optimize assays for use with the TRI-Analyzer system, the focus of this chapter is on the demonstration of ease of translation of the thousands of existing, readily adaptable, commercial assays on the market. Diagnostic assay kits for the PC biosensor modality are not commercially available.

We chose our assay application demonstrations to represent tests that have important implications for maternal and neonatal health in developing parts of the world where a POC test would have enormous value. First, we perform an ELISA assay for detection of fetal fibronectin, a biomarker protein test for expectant mothers that is diagnostic for spontaneous pre-term birth. Next, we perform a fluorescence-based assay for phenylalanine, a biomarker used to diagnose phenylketonuria, a life-threatening but manageable genetic condition, in newborns.

3.2 Optical Design and Fabrication

An important design requirement for the TRI-Analyzer was to make the approach easily adaptable to any smartphone with a rear-facing camera and rear-facing flash LED through small mechanical adjustment to the cradle body, but without adjustment of the core optical components. Thus, we chose to use optical fibers to bring light from the LED to the test sample, and to bring light from the test sample to the camera. In principle, the core optical components of the system would be identical for any smartphone, with two simple changes: 1) the phone interface is modified to use the physical dimensions of the phone to align the sensing fiber with the rear-facing camera and 2) the illumination fiber would be routed to collect light from the smartphone flash. As shown in Figure 3.1, the distal end of the "illumination" fiber (100 μm diameter, multimode) is placed

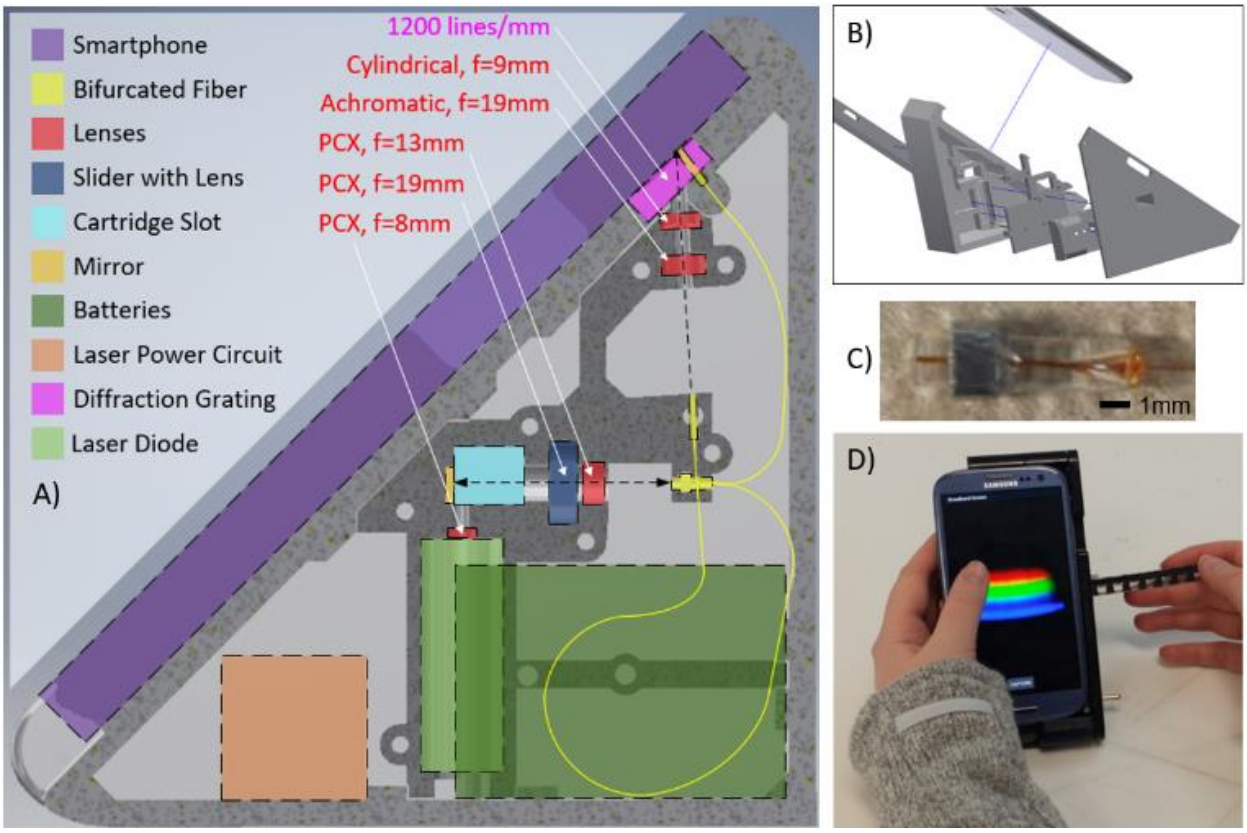

Figure 3.1. Design of Spectral TRI-Analyzer. A) Schematic of internal layout for optical and electrical components. A custom bifurcated fiber (100um core with d=1.8 mm glass capillary tube (proximal) and 2x d=1.25 mm ceramic ferrules, Coastal Connections) was used to compact the light path into a handheld device. Fiber is arranged to maximize bend radius, increasing long-term stability. B) 3D CAD model was created, comprised of 5 plastic parts printed via stereolithography. Two halves of optical housing maintain lens alignment and optical chamber isolation. All portions of cradle were designed to slide together and attach with M3x0.5 machine screws. C) Glass capillary tube with bifurcated fibers and metal nut used to align the fiber in the cradle. D) Image of final device in use with absorption cartridge.

directly in front of the flash LED to direct white light through the test sample for the Transmission and Reflectance modalities. The other "sensing" fiber (100 µm diameter, multimode) collects light transmitted through the test sample, reflected from the PC, or emitted by fluorophores at its proximal end and directs it toward the rear-facing smartphone camera, oriented at a 41.3-degree angle. The light emerging from the sensing fiber is collimated by an aspheric lens (EFL = 19 mm) and then focused in the non-spectral dimension with a cylindrical lens (EFL = 9 mm) before passing through a 1200 lines/mm transmission diffraction grating (Edmund Optics 49-578) held within the cradle body directly over the opening of the rear-facing camera. The light is focused to optimize use of the CMOS pixels in the non-spectral dimension allowing for increased sensitivity.

The proximal ends of the sensing and illumination fibers are gathered together in a bifurcated configuration, so they are directly adjacent and held within a glass capillary tube that is mounted in a slot within the cradle body. The optical fiber assembly is the only custom-made component of the system, due to the specific fiber length requirements (71 mm for the illumination fiber and 137 mm for the sensing fiber) and ferrules on the distal ends. Due to the accuracy of the 3D printing technology used to generate the cradle (FormLabs, Form 2 at 50 µm resolution), all optical components (lenses, reflection mirror, optical fiber assembly, and green LED) may be placed into their respective holding locations in correct optical alignment without further modification and minimal tuning of the system with set screws for each of the fiber terminations.

For transmission and reflection modalities the smartphone flash serves as the light source. It is collected by one of the two distal ends of the bifurcated optical fiber, and expanded to a collimated beam with a plano-convex lens (Figure 3.2). After passing through the sample chamber, either complete reflection (Transmission) or wavelength-selective reflection (Reflection) results in the signal passing through the sample once again and being focused on the image of the proximal end of the sensing fiber for Transmission or Reflection modalities, respectively. The mirror is mounted and aligned inside the cradle, where it serves as the default reflection surface. For the Intensity modality, a 532 nm laser diode (10 mW, 3V), similar to those found in green laser pointers, is shone orthogonally to the main optical path of the instrument. With the flash turned off, the collecting light path of the instrument is augmented with an additional lens which serves to focus the collection to a point close to the rear face of the cartridge. This lens is inserted into the optical path by pressing a button on the exterior of the cradle, which slides the lens into the correct position. The laser is focused within the test sample at the same point within the

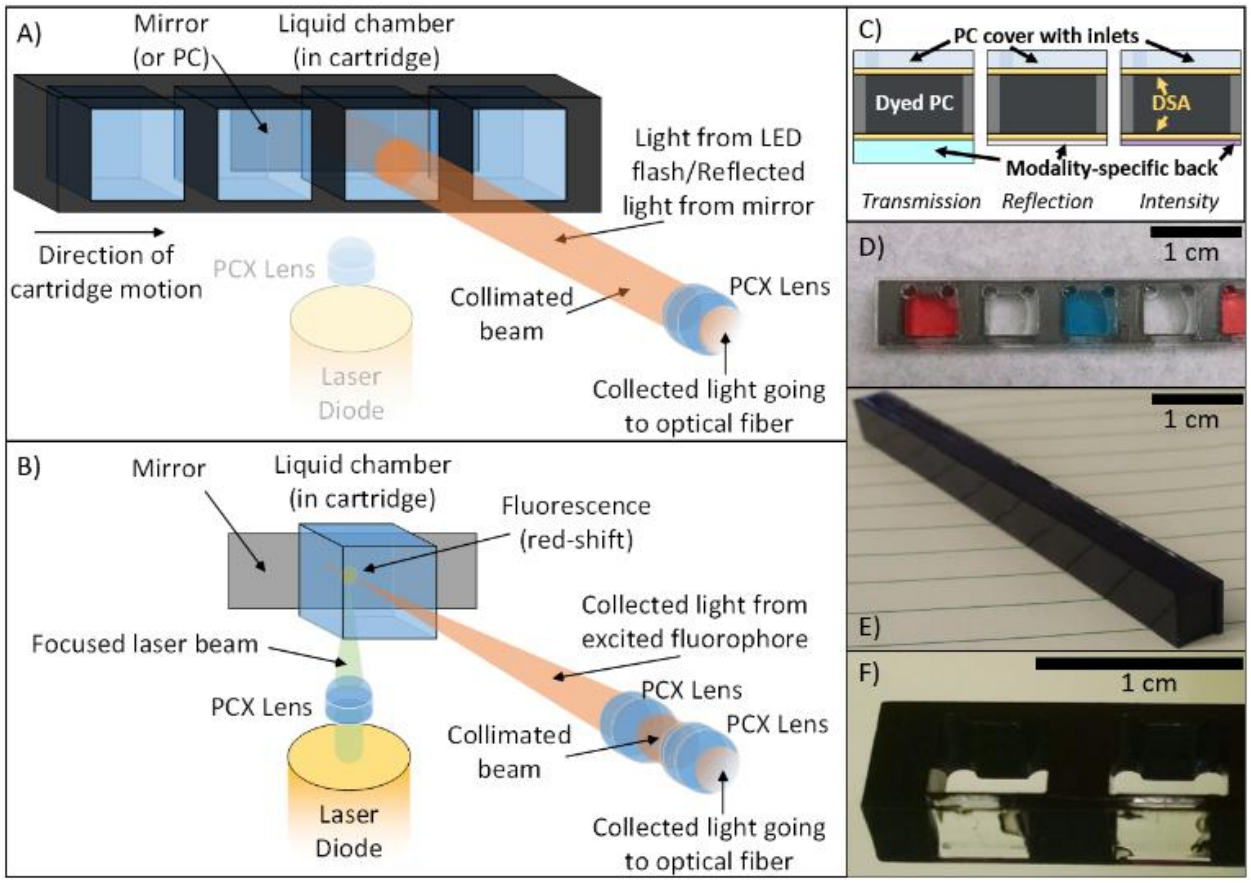

Figure 3.2. Two principal light paths and cartridges for each of the three modalities. A) Reflection (PC-only) and Transmission (absorption or PC) optical pathway. Collimated light from the on-board smartphone flash is directed through the sample chamber. For reflection-based PC measurements, a back-coated cartridge prevents transmitted light from being collected. For transmission measurements, light is reflected by cradle mirror directed toward the collection fiber. B) Fluorescence/Luminescence Intensity optical pathway. A laser pointer diode is co-focused to a point near the back-side of the cartridge where the collection fiber is similarly focused via addition of a single plano-convex lens into the optical path via a SLA-printed slider actuated from outside the cradle. Additional cartridge wells/housing was removed for clarity in B). C) "Sandwich" style cartridge fabrication alternating plastic or glass substrates with double-sided-adhesive (DSA) showing how different backings facilitate different modalities. D) Transmission cartridge showing inlet/outlets and optically-isolated chambers. E) Dyed PC for label-free Reflection measurements. F) Close-up of Intensity cartridge demonstrating selectively-dyed cartridge body allowing for bottom-illumination with 532 nm laser diode.

cartridge at which the collection lens is also focused to provide for maximal fluorescence collection.[96]

All optical components were optimized via non-sequential optical simulation (Zemax), with total optical efficiency prioritized for the Intensity modality's optical configuration. The 3D-printed cradle is comprised of two housing pieces held together with steel fasteners to robustly

maintain optical alignment. Holes were threaded with an M3 tap, and final clearances of moving parts were adjusted by hand to allow for smooth sliding before mounting and alignment with machine screws. Optical alignment was completed first with the transmission/reflection light path, and then with the intensity light path, using a cartridge with rhodamine 590 chloride (Exciton) laser dye to visualize the optical paths.

The laser diode is powered by a custom circuit providing a constant-current to the diode from three on-board AAA batteries, based on a LED flashlight control circuit (Texas Instruments). This circuit is soldered on a small protoboard, and attached to a switch accessible from the outside of the cradle (visible in Figure 3.1D).

To interface with the cradle, custom cartridges were designed to facilitate introduction of samples to the light path. While all based on the same fundamental construction, each modality requires slight modifications to the cartridge design (Figure 3.2 C-F). The cartridge bodies for each modality are comprised of a laser-cut acrylic sheet. This acrylic sheet provides the separation between chambers, and the overall structure for the cartridge, which can be modified to support different sample measurement cross-sectional areas, sample volumes, and chamber spacings. For our experiments, we selected a chamber spacing that would allow for user-friendly sample manipulation with an 8-channel multipipette. Laser-cut 50-μm thick double-sided adhesive (DSA) (3M, Optically Clear Adhesive 8212) is applied to both sides and a thin acrylic cover with laser-cut access ports is adhered to the front of the cartridge, as shown in the cross section of Figure 3.2C. The back of the cartridge is comprised of glass (Transmission cartridges), acrylic film (Intensity cartridges), or PC-coated polycarbonate film (Reflection cartridges). Depending on the modality, different portions of cartridges are dyed with opaque black dye (Dykem 81724) (Figure 3.2E-F) to prevent optical communication between adjacent fluid compartments and to provide a

clear boundary between cartridges for automated sensing of the compartments as they pass the illumination/read head during video-based cartridge scanning. To provide consistent positioning of the cartridge in the light path, a copper spring is attached to the collection-end of the cartridge chamber, so the cartridges are pressed firmly against one wall of the cradle's slot.

A custom Android app was developed to assist with data collection. This app sets parameters, including exposure time and focal length, to constant values to provide for inter-assay consistency and to facilitate data collection. After the assay of choice has been completed and is ready to be measured, the App allows the user to choose the number of samples, standards, and replicates before walking the user through collection steps for each liquid chamber and/or cartridge.

Qualitative proofs-of-concept for each of the three modalities were completed with prepared test liquids in the cartridge chambers (Figure 3.3). To demonstrate Transmission measurements, we prepared a series of diluted yellow food dye (McCormick) to a range such that measurable optical absorption was observable on the system (~1:1000), and then performed serial dilutions to observe concentration-dependent absorbance (Figure 3.3A). Note that, as the dye absorbed primarily wavelengths in the blue portion of the spectrum, the blue wavelengths are removed from the image as the dye concentration increases. Difficulties in aligning the sample chamber with the optical path for low concentrations of yellow dye resulted in a high standard deviation, which was addressed with dyed cartridges as shown in Figure 3.2D (data not shown). To demonstrate the Reflection modality, we used a PC-integrated cartridge and introduced mixtures of 0%, 20%, 40%, 60%, and 80% ethanol (EtOH) in water to manipulate the bulk refractive index of the liquid in contact with the PC (Figure 3.3B). Note that only a narrow band of wavelengths are efficiently reflected by the PC into the sensing fiber, representing a narrow

bright red band in the spectrum image gathered by the phone's image sensor. A single cartridge was filled with water, followed by the 5 ethanol concentrations to normalize for intra-sensor variation in starting resonance wavelength. By taking the middle row of pixels from the raw images, we observed a clear relationship (R^2 =.986) between the change in peak wavelength value (PWV) reflected from the PC with the addition of EtOH solutions and the refractive index of the liquid inside the fluid compartment, corresponding to a 114.0 nm/RIU bulk refractive index sensitivity. Finally, to demonstrate the Intensity modality, we used the laser to excite the

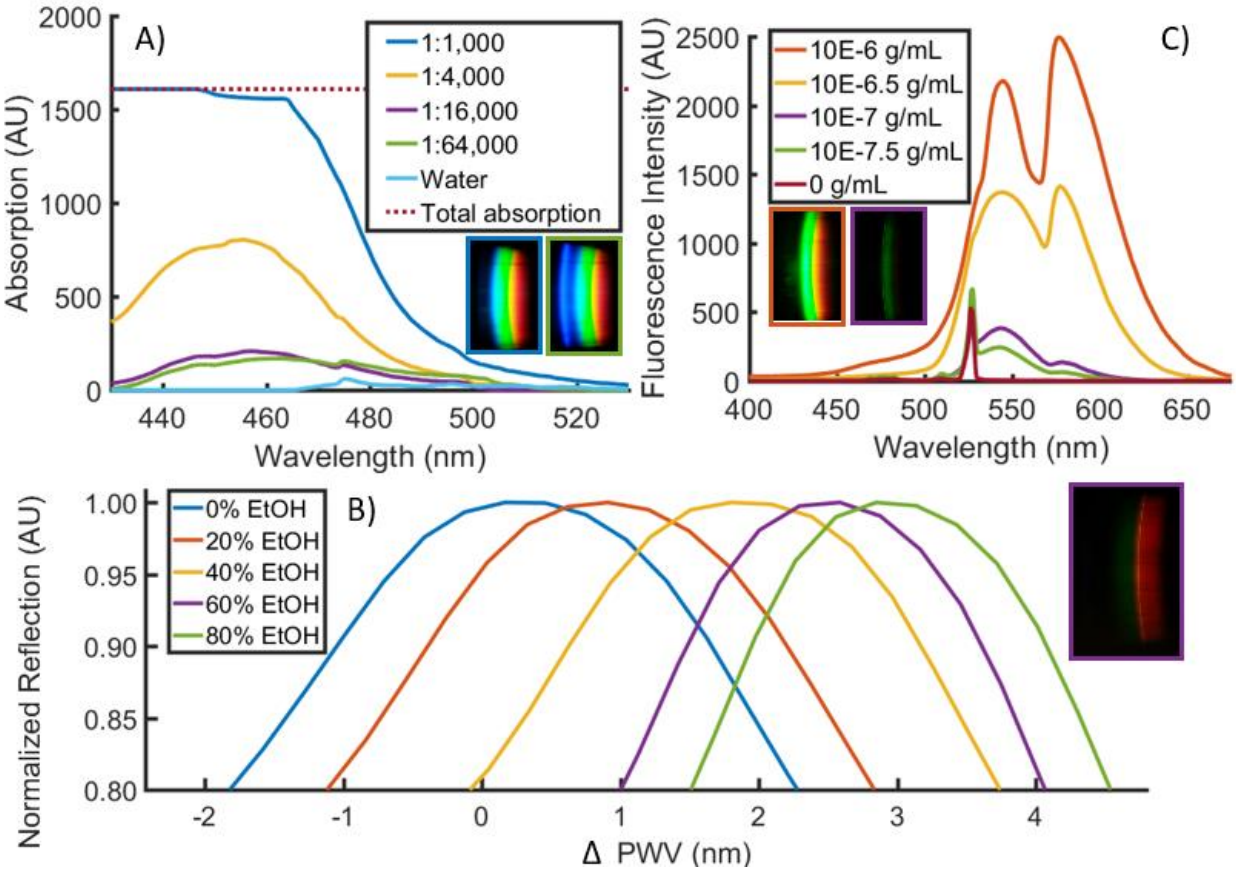

Figure 3.3. Qualitative proof-of-concept of 3 principal modalities. A) Transmission. Yellow food dye was diluted in water at concentrations ranging from 1:1,000 to 1: 64,000, a 64x concentration range. Absorption was measured by subtracting sample transmission from that of water. Observable absorption occurred in the blue region (400-500nm) of the spectrum. Inset raw images correspond to concentration of yellow dye of their outline. B) Reflection. 0-80% mixtures of ethanol in water were prepared and introduced into a PC-based cartridge, producing narrowband reflection in the 580 nm range. Measurements of each cartridge chamber filled with water were subtracted from measurements of those chambers filled with ethanol solutions to produce ΔPWV shifts. Inset raw image corresponds to concentration of ethanol of its outline. A central line of pixels was used to produce spectra shown. C) Intensity. R6G dye was diluted in water and excited with the on-board laser diode. Inset raw images correspond to concentration of R6G of their outline.

fluorescent emission of rhodamine 590 chloride (R6G) (Exciton) within a cartridge configured for Intensity measurements. The dye was diluted to concentrations between 10^{-6} and $10^{-7.5}$ g/mL, and resultant images were processed to generate fluorescence intensity spectra (Figure 3.3C). Note that the green emission from R6G is clearly visible over the entire range of concentrations, the intensity is concentration dependent, and that, due to the orthogonal illumination, a minimal amount of light from the laser diode illumination source is present within the fluorescence emission spectra, even at low R6G concentrations.

3.3 Validation of the Spectral TRI-Analyzer with Commercial Diagnostic Tests

To demonstrate the capabilities of the system, we selected a representative assay for each light path with a common theme of IVD tests performed in the context of maternal and child health. Recognized as two of the eight Millennium Development Goals (MDGs) by the UN, maternal and child health has remained one of the primary foci of global health strategies. As we transition from the MDGs to the recently released Sustainable Development Goals (SDGs), the WHO released a retrospective analysis of our successes and remaining challenges in the realm of health around the world. From that report, most of the major successes coming out of the health related MDG efforts have been related to infectious diseases, while most of the largest shortfalls are within the realm of maternal and child health. Many countries have initiated subsidized maternal and child health programs, and health outcomes have improved; however, there is significant work to be done to improve outcomes for mothers and children alike, which motivates the specific applications we have selected to demonstrate in this chapter.[97,98]

3.3.1 Transmission/Reflection Light Path: Fetal Fibronectin ELISA Assay

According to the WHO, over 10% of babies born each year are preterm, and complications arising from these births constitute the single leading cause of death in children under the age of

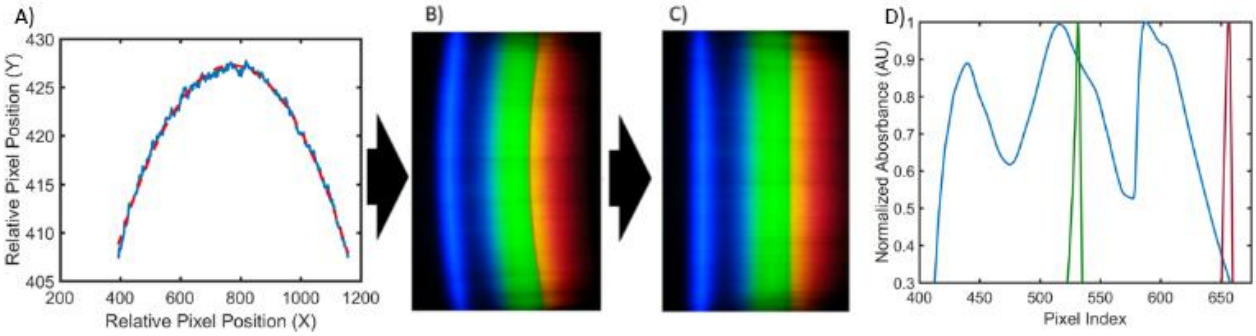

Figure 3.4. Spectrum Processing. A) Boundary of the red channel is found in every row of the image and a circle is fit (B). C) Straightened spectral image used to generate a single data spectrum. D) Laser pointers are used to determine pixel-to-wavelength conversion as reported previously.

5.[99] While multiple strategies exist to reduce complications associated with preterm births, diagnosis can often be challenging.[100] Fetal fibronectin is a glycoprotein that has a high negative predictive value for spontaneous preterm birth.[101,102] Particularly when combined with a physical measurement of the cervical length, fetal fibronectin is an important diagnostic indicator to facilitate treatment, continued monitoring, or hospital referral of at-risk mothers. While rapid lateral flow-based assays exist, they are not quantitative, and require specialized proprietary readers.[103,104] Serological detection of fFN is routine in a laboratory setting, and the translation of a fFN test to a point-of-care diagnostic would provide useful information to health care providers, particularly with populations at-risk for pre-term births.

For fFN detection, a commercially available ELISA kit was purchased (CUSABIO) and used to generate standard curves, as well as measure spiked serum concentrations within physiologically relevant ranges. Kit reagents were prepared following manufacturer instructions, and reactions were completed in the included 96-well microplate. Standard concentrations were serially diluted and run in triplicate at concentrations ranging from 4 to 1000 ng/mL. Spiked plasma samples were created at a concentration of 50 ng/mL from human plasma (n=3). All samples were added to the microplate, and ELISA steps were completed per manufacturer directions. After the addition of stop solution, the samples were immediately read in a benchtop

96-well plate reader (BioTek, Synergy HT), and then transferred to a sample cartridge with a multichannel pipette.

Filled cartridges were measured using the developed App to take five images of each sample as it was slid through the cartridge slot. The cylindrical lens that extends the non-spectral dimension of spectra onto the image sensor introduces spherical aberration, resulting in a curved appearance of the resultant spectrum images, as shown in Figure 3.4A-B. As this is a function of internal optics and not the alignment of the smartphone and the cradle, the curvature observed is constant throughout multiple measurements and multiple phone removals/insertions (data not shown). By fitting the pixel locations of where the red filter drops off (~580 nm) in each spectral row to a circular arc, spectra can be linearized and then summed in the non-spectral dimension (Figure 3.4C). The result is a spectrum where pixel distance corresponds directly to wavelength, a relationship that can be interpolated from measuring two known lasers with the smartphone system and interpolating the wavelengths in between (Figure 3.4C). Finally, to adjust for overall intensity variation resulting from imperfect cartridge alignment with the optical path, a linear scaling least-squares fit was performed on the spectrum above 500 nm (outside the region of interest of our chromogen absorbance) when compared to a broadband spectrum (measured with ultrapure water). Resultant normalized transmission spectra were subtracted from the same broadband spectrum, resulting in absorption spectra (Figure 3.5). Similar limits of detection were observed between the 96-well microplate reader and Spectral TRI-Analyzer, both well under the minimum assay detection range (25 ng/mL), with the lowest discernable assayed concentration being 37.0 and 12.3 ng/mL, respectively. Bland-Altman analysis was performed on the measurements from the 96-well plate reader and the Spectral TRI-Analyzer, and all data were shown to be well within the 95% confidence intervals (Figure 3.6).

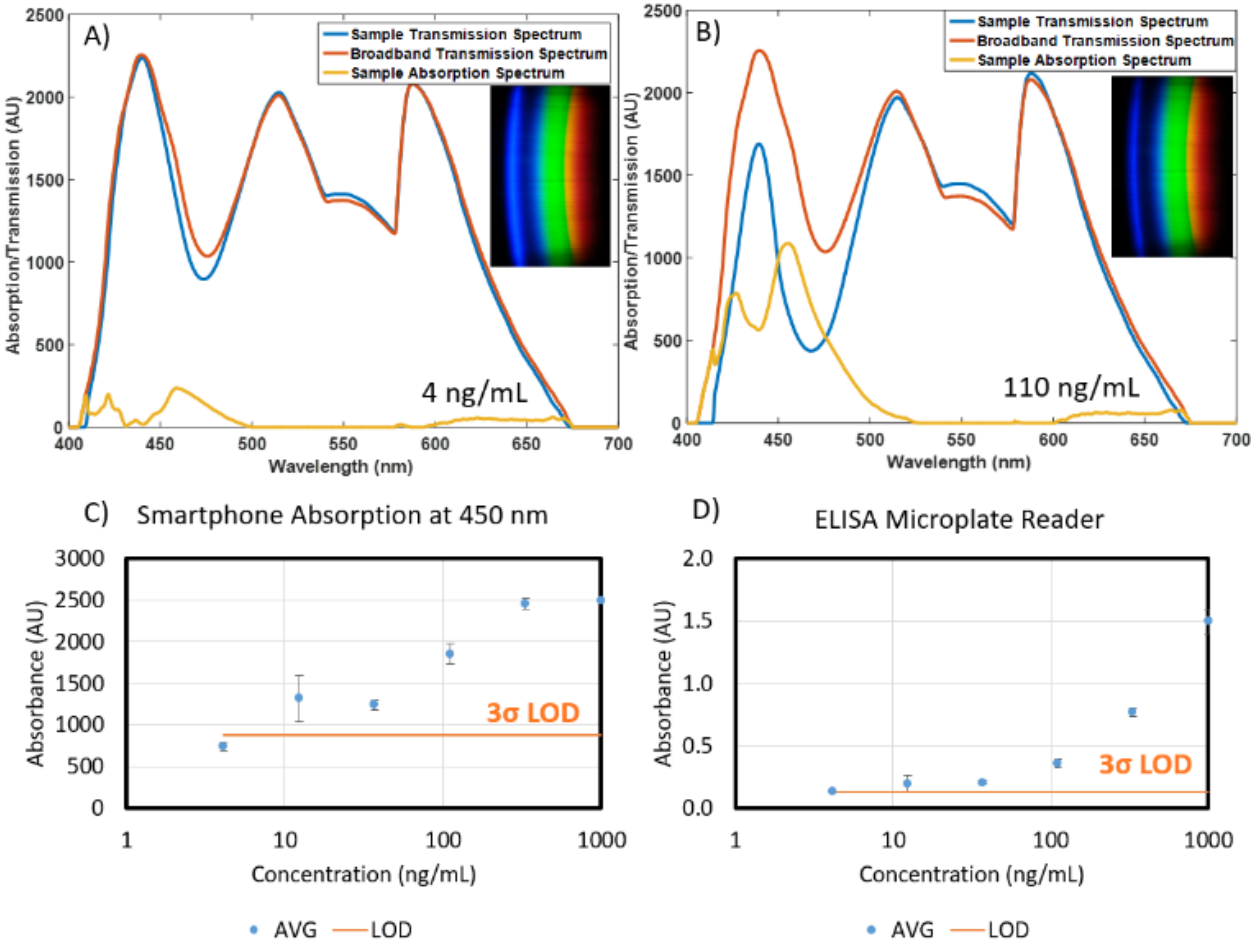

Figure 3.5. A) and B) Sample transmission spectra, absorption spectra, and raw RGB image data (insets) for 4 and 110 ng/mL samples of fFN, respectively. C) and D) Comparative dose-response curves for spectral TRI-analyzer and 96-well microplate reader. Standard concentrations from 4 to 1000 ng/mL were assayed along with a human serum sample spiked at 50 ng/mL (not shown). Limit of detection was determined as 3 standard deviations over the mean of zero concentration standard (n=3).

3.3.2 Intensity Light Path: Phenylalanine Fluorescent Assay

The prevention of phenylketonuria-associated mental deficits been recognized at one of the largest public health successes of the past 50 years with over 4000 lives saved since screening methods began in the US 50 years ago.[105] Global prevalence is regionally varied, ranging from 1/200,000 in Finland to 1/2,600 in Turkey.[106] Traditional newborn screening techniques are based on a heel prick, originally used for bacterial metabolic assay, but now often run via mass spectroscopy.[107-109] Benefits of translating newborn birth screening tests to a smartphone-based

point-of-care device including cloud-integration and data storage, familiarity of user-interface, cost-effectiveness and portability, directly map to challenges identified by the US Department of Health and Human Services, including the feasibility of statewide surveillance, tracking, and reporting, the roles and responsibilities of a broad and varied user base, and the cost and number of tests needed.[110]

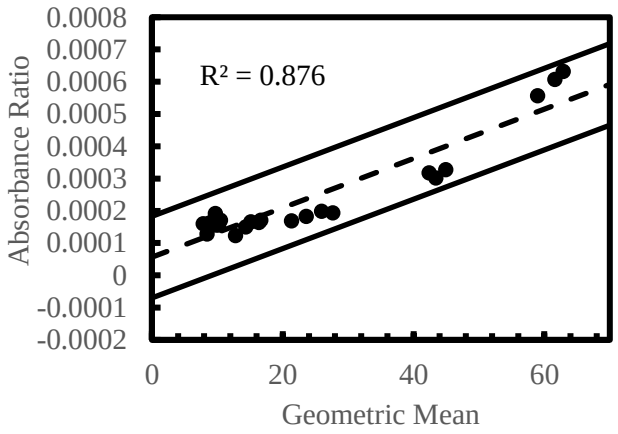

Figure 3.6. Bland-Altman Analysis of Spectral TRI-Analyzer compared with standard microplate reader for readout of fFN assay. A variation on the standard Bland-Altman method using the geometric mean and log difference was applied to all non-zero values for each assay (Bland). The log differences showed a dependence on the magnitude of the measurement, so a regressive approach was used to model the relation, as described by Bland (mean of regression shown with dashed line). ±1.96 S.D. limits of agreement are shown as solid lines.

A commercially available assay kit was purchased (Sigma Aldrich) for the quantification of human phenylalanine. The phenylalanine standard was reconstituted in water, and serially diluted to concentrations of 0.8, .6, 0.4, 0.2, 0.1, 0.05, and 0 nmol/well. Human serum samples were deproteinized using a 10kDa MWCO spin filter before being diluted with assay buffer and added to wells in triplicate (n = 3). The samples were pre-treated for 10 minutes at room temperature with tyrosinase to control for background interference. A sample/standard reaction mixture of developer, enzyme mix, and buffer was added to each of the wells per manufacturer directions. The solutions were allowed to incubate, covered and protected from light, for 20 minutes at 37 C. Using a commercially available 96-well microplate reader (BioTek, Synergy HT), the completed assay was measured for fluorescence, exciting at λ=535 nm and measuring at λ =587 nm. Samples were then transferred to cartridges, as described previously, and measured for fluorescence using the Spectral TRI-Analyzer.

For data acquisition of the fluorescence data, an improved data collection procedure was developed. For absorption-based measurements, the stability of light output is time insensitive; however, with fluorescent dyes, both excitation intensity variation resulting from commercial laser diodes (even after circuit-based feedback control) and fluorophore photobleaching result in a time-dependence of our measurements. To mitigate these variances, we developed a post-processing method that allows us to capture data as a video as the user slides the cartridge through the cradle, thereby reconstituting the spatial dimension in which the multiple sample chambers are introduced into the light path. By analyzing mean pixel value across each frame of the video, contiguous framesets of signal corresponding to each of the sample chambers in the cartridge could be identified (Figure 3.7). The center 80% of these frames were averaged, and used as an image to generate a spectrum, as done with the ELISA data. These spectra were then normalized using the measured integrated area of the excitation laser of the sample chambers before assay completion. This normalization method was validated using Bland-Altman Analysis (Figure 3.8). The resultant fluorescence spectra resulted in a clear dose-response curve with a comparable limit of detection to that of the commercially available plate reader (Figure 3.9). The limit of detection for the Spectral TRI-Analyzer was less than the lowest assayed concentration (0.5 nmol), while the limit of detection for the 96-well plate reader

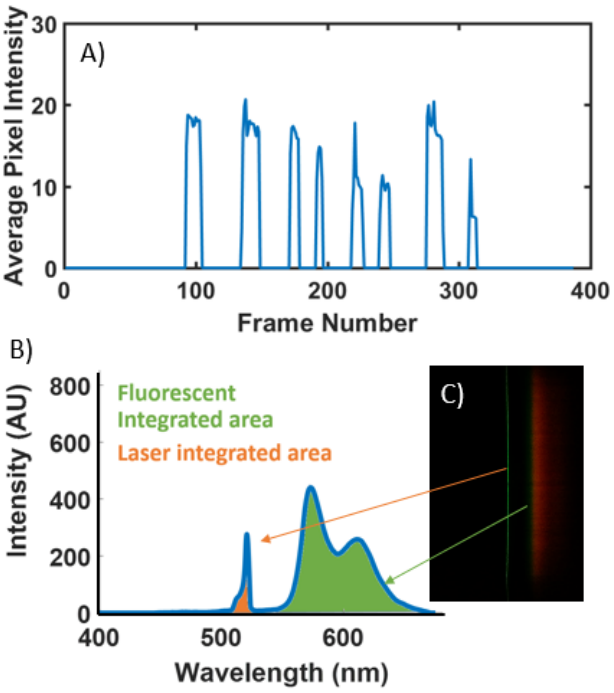

Figure 3.7. Video Processing and Normalization. A) Average pixel intensity of a data-collection video showing clear demarcation of 8 sample wells. B and C) Example fluorescent spectrum showing regions used to normalize the data.

was between 0.5 nmol and 1.0 nmol. We observe saturation of our signal at higher analyte concentrations, suggesting our system may have a lower dynamic range than the microplate reader.

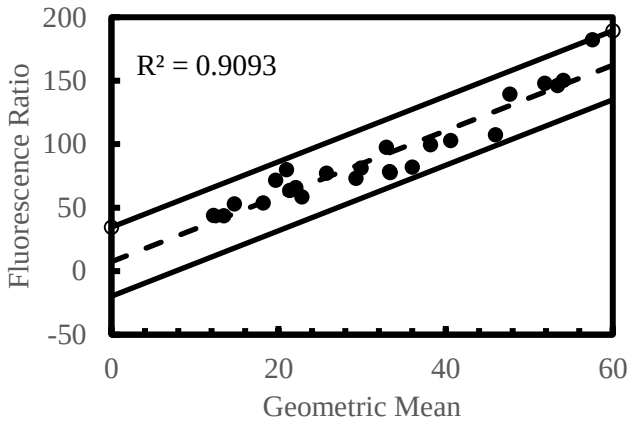

Figure 3.8. Bland-Altman Analysis of Spectral TRI-Analyzer compared with standard microplate reader for readout of phenylalanine assay. A variation on the standard Bland-Altman method using the geometric mean and log difference was applied to all non-zero values for each assay. The log differences showed a dependence on the magnitude of the measurement, so a regressive approach was used to model the relation, as described by Bland (mean of regression shown with dashed line). One point was found to be outside the ±1.96 S.D. limits of agreement (solid lines).

3.4 Conclusions

Our unique Spectral TRI-Analyzer system demonstrates the breadth of IVD assay possibilities and applications that can be achieved within a single instrument. Each of the three optical biosensing modalities offers up a wide array of existing assays that have been developed for the laboratory setting that can be rapidly translated to be used with such a POCT device.

The development of this device takes advantage of both the rapid improvements to smartphone hardware and software as well as the significant improvements in resolution and affordability of SLA-based 3D printing.

Over the past ten years the rise of low-cost, consumer-grade 3D printers has resulted in the "maker community" developing into a 5.1-billion-dollar industry. The first wave of consumer products was comprised of FDM-based additive technology due to its ease of use, lack of mess, and minimal danger. SLA, by comparison, has remained largely in the industrial/research realm, though continued improvements in technology suggest that it could find a home in the consumer marketplace. Now capable of achieving 10-100 μm resolution, consumer grade SLA-based technology has entered the realm of positional accuracy of traditional table-top optics mounting.[96]

Together, the disruptive technologies of smartphones and 3D printing pose a unique opportunity for the rapid development of low-cost point-of-use biosensing devices. Traditional optical alignment requires significant amounts of expensive hardware and bulky interfacing equipment to position lenses and other components in custom alignments. 3D printing presents a unique benefit in being able to rapidly produce custom mounts and interfaces. By coupling these two technologies together, we have demonstrated an exciting frontier of rapid-prototyped, low-cost, smartphone-based optical devices for use at the point of care. Additional TRI-Analyzers have been made quickly and cheaply for distribution to collaborators in a way that benchtop-based proof-of-concept optical systems simply cannot.[96]

This demonstration paves the way for a variety of prototyping applications in optical system design where 3D-printed optical mounts could augment or even replace conventional benchtop optical assembly and alignment. In particular, within the realm of optical biosensors designed for the point-of-care, this presents significant potential to create new optical systems that can proceed from computer simulation directly to handheld prototype.

Similarly, we have demonstrated a rapid-prototype-friendly method for micro- and milli-fluidic cartridges for use with mobile biosensing devices. By linearizing fluid chambers into multi-sample cartridges, we can provide simple multiplexing which is useful both for assays requiring

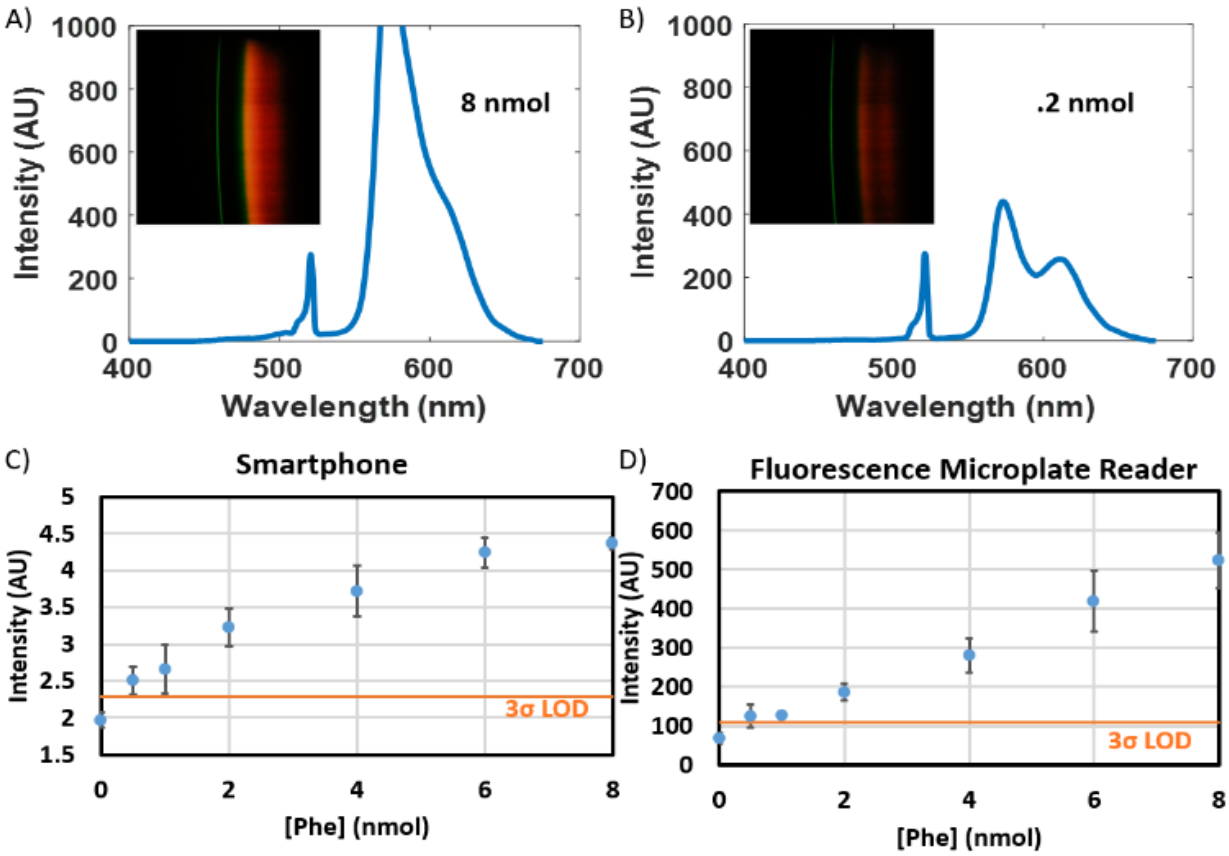

Figure 3.9. Results of Phenylketonuria Assay. A) and B) Sample transmission spectra, absorption spectra, and raw RGB image data (insets) for .8 and .2 nmol samples of phenylalanine, respectively. C) and D) Comparative dose-response curves for spectral TRI-analyzer and 96-well microplate reader. Standard concentrations from 0 to 8 nmol were assayed. Limit of detection was determined as 3 standard deviations over the mean of zero concentration standard (n=3).

multiple standards or controls, or situations where many samples might be run at once. The simplicity of our laser-cut acrylic sheet and DSA assembly opens the door for a myriad of other possible cartridge configurations, including increasing the number of sample chambers per cartridge for further multiplexing, or incorporating other microfluidic assay steps such as sample lysis, mixing, or other mainstays of microfluidic-chip based technology. For example, the specific dimensions and layout of our cartridges was designed to maximize convenience for interfacing between the assay solutions run on our benchtop comparison instruments that used a 96-well plate format by having sample ports spaced and sized to match the end of an 8-well multichannel pipette.

In the demonstration of our system with existing commercial assays we sought to exemplify the sorts of laboratory-grade tests that could be directly transferred to the point-of-care. Thousands of these kits exist that rely on optical readout of sandwich immunoassays with either absorbance or fluorescence-based reporting molecules (ELISA, FIA, CLIA), and many new assays are being developed based upon other novel techniques, including those using bioluminescence, SPR, PCs or other selective-resonance phenomena.

Video-based capture of sample signals is a natural complement to our developed linear cartridge, further simplifying multi-analyte multiplexing into a more user-friendly interface. This represents a novel data collection method that represents yet another natural benefit of harnessing extant smartphone imaging technology for spectral analysis and biosensing applications. To our knowledge, no such video-based multiplexing of spectral data has been described. The developed image processing holds potential for further expansion into future devices that can take advantage of such a 'swipe' based interface. The swiping of a credit card is a ubiquitous motion that readily simplifies multiplexed sample measurements compared to those in a typical cuvette-based measurement system.

The presented results of both proof-of-concept assays demonstrate that the Spectral TRI-Analyzer can replicate the sensitivity of conventional benchtop laboratory instruments. In both assays, our smartphone-based system could detect concentrations of assayed analyte less than those detected on a conventional laboratory instrument. The single largest compromise observed with our system was a decrease in dynamic range for the assays. In the fFN experiment, near-complete absorption of light at 450 nm at high concentrations resulted in signal saturation. For this particular assay, this would likely be acceptable as threshold ranges from literature range from 10-200 ng/mL[111-113]. Similarly, in the phenylalanine assay, our instrument did not produce a linear

dose-response curve, instead demonstrating a saturation-curve relationship at higher concentrations. Likely using a 4-parameter logistic growth curve instead of a linear fit would allow for appropriate unknown concentrations to be determined using our system, but as shown by our Bland-Altman analysis for this data, even the unknown concentration in our serum sample was shown to be measured with agreement between it and our benchtop analyzer. This level of agreement was demonstrated for both assays at all concentrations, suggesting that our device can successfully reproduce the expected assay measurements from identical samples.

A key challenge in developing any successful IVD for use at the point-of-care is achieving a device that is financially feasible. To construct a single system, the cost of components of our system was approximately $550. Many previous proof-of-concept demonstrations have focused on a single usage case, which significantly decreases the cost effectiveness of any diagnostic device. The broad applicability of our device provides a necessary linkage between early proof-of-concept work (Chapter 2) and the future possibility of truly portable POC devices being developed at the frontiers of bioengineering (as the one described in Chapter 5). Demonstrated here is just one example set of related tests that individually might not result in a commercially viable IVD device, but together, provide a powerful opportunity to distribute maternal and child health monitoring from central laboratories to clinics and health outposts worldwide. These experiments represent the end of the academic engineering process, with a successful translation arrangement with a corporate partner who will continue to commercialize the underlying technology for applications in both human and animal health arenas. In the next half of this dissertation, I will present a new iteration of the engineering design process. This time, instead of translating mature laboratory instruments to the POCT paradigm, I hope to inject point-of-care considerations into the initial phases of cutting edge of biosensor development.

CHAPTER 4: HIGH-SENSITIVITY BIODETECTION: PHOTONIC CRYSTAL ENHANCED MICROSCOPY[1]

4.1 Introduction

As discussed in Section 2.4, photonic crystals present a unique biosensing opportunity to observe attachment-based events without the use of labels, dyes, or amplification. In Chapters 2 and 3, we discuss the bulk properties of PC biosensing, where many individual attachment events affect the PC resonance condition of a region-of-interest on the PC sensor. When using the imaging sensor of a smartphone as previously described, we convert one of the dimensions of the imaging sensor to a spectral dimension, which results in the loss of one dimension of spectral information. This means that the resultant PWV images represent the average PWV shift of the entire illuminated area. In the pursuit of high-sensitivity, low-concentration detection of biomolecular interactions, it is possible to alter this illumination area to a narrow line, which can then be scanned across a surface, thereby allowing us to reintroduce the second spatial dimension previously sacrificed. This third dimension is generated by moving a PC sensor incrementally and taking serial images, which can then be reconstituted. The spatial resolution afforded by this change results in a device (termed the Photonic Crystal Enhanced Microscope, or PCEM)[114] that can move from millimeter-scale ROI analysis to micrometer-scale resolution of biological attachment events, making it a unique tool for label-free detection of cellular processes, as will be discussed in this chapter. Then, in Chapter 5, we will investigate the limits of spatial resolution for the PCEM, demonstrating nanometer-scale individual attachment events, providing a unique opportunity for digital detection of protein and other subcellular interactions. That work will

[1] This Chapter contains work previously published as outlined in both the Acknowledgements and References.

enable the development of a similarly spatially-resolved smartphone-based instrument for point-of-care applications. To explore the micrometer-scale capabilities of the PCEM, we will look at cell-surface interactions and how they change over time *in vivo*, taking advantage of the truly label-free capabilities of the instrument.

Cell membrane interactions with surfaces are fundamental aspects of many *in vivo* biological phenomena including differentiation, growth, apoptosis, tumor metastasis and injury response[115,116]. Characterizing these processes in the laboratory traditionally involves fluorescent dyes, fluorescent proteins, histological stains, or fixation. Such approaches are either cytotoxic, or temporally constrained by the effects of fluorescence photobleaching. While these techniques elucidate the mechanics and outcomes of cellular processes, the lack of long-term, time-course data collection poses a serious compromise to the study of natural cell behavior during processes that occur over extended time scales like cell invasion[117] and chemotaxis[118].

In order to address the challenges inherent in label-based cell imaging techniques, label-free microscopy technologies have been demonstrated as effective tools for measuring an increasingly diverse range of cellular processes[119-122]. Label-free microscopy involves a biosensor transducer surface that generates an electrical or optical signal when cells interact with it. Biosensors measure intrinsic cellular properties (such as dielectric permittivity) that can be used to determine the number of cells in contact with the transducer, or to determine the distribution of focal adhesion points. Such transducers may be prepared with surface coatings that either selectively capture specific cell populations through interaction with proteins expressed on their outer membranes or mimic the *in vivo* microenvironment within tissues.

Due to the fundamental importance of cell-surface interactions, several technologies have sought to quantify and image cell membrane adhesion. Surface Plasmon Resonance imaging

(SPRi)[123] is capable of detecting cell attachment to a gold surface by measuring changes in the intensity of front-reflected light at a fixed angle and wavelength, but practical limitations degrade image quality. SPRi requires illumination to pass through cell structures, which introduces changes in reflected light intensity that are not related to cell surface attachment, and the lateral propagation distance of surface plasmons limits spatial resolution[124]. Interpretation of SPRi images is complicated by the variability of reflected light intensity introduced by scattering, inhomogeneity of the light source, and nonuniformity of the sensor surface[125], while non-normal light via prism coupling hinders the quality of focus[126]. Atomic force microscopy (AFM)[127] has been used to study surface morphology and mechanical properties of cells by using a probe tip to collect localized force response. While it provides information about biological surfaces by making measurements from above, AFM does not analyse the interaction between cells and their substrates. In addition, as a probe scanning approach, the throughput of AFM is limited, enabling the study of only a small number of cells at once.

In this chapter, we demonstrate photonic crystal enhanced microscopy (PCEM) as a label-free biosensor-based cell attachment imaging approach that quantifies cell-surface interactions with spatial resolution sufficient for monitoring intra-cell attachment distribution, and temporal resolution sufficient for generating time-lapse movies during processes that include chemotaxis, apoptosis, differentiation, and division. Critically, these studies can be performed on extracellular matrix (ECM) protein functionalized substrates, retaining the capacity to define the chemistry of cell-matrix interactions. The system is integrated with an incubator, enabling long-term monitoring of cell attachment over substantial time scales (hours to days) without interruption of the culture environment. The key innovation enabling these capabilities is the use of noncoherent illumination of a photonic crystal biosensor and a spectroscopic scanning system that couples with a microscope

objective. Here, we demonstrate label-free time-lapse imaging of the attachment and chemotaxis of dental stem cells using PCEM. Single-cell movement and filopodial extension are easily identifiable, yielding significant potential for the future investigation of numerous cellular processes including tumor cell metastasis and stem cell differentiation. While still an *in vitro* environment, the elimination of cytotoxic fluorophores and reporter molecules allows for the controlled study of complex biological processes over extended time periods.

4.2 Photonic crystal biosensor surface engineered specifically for cell attachment

Photonic Crystal (PC) biosensors have recently been demonstrated as a highly versatile technology for a variety of label-free assays including high-throughput screening of small molecule-protein interactions, characterization of protein-protein interactions, and measurement of cell attachment modulation by drugs[128-130]. A PC is a sub-wavelength grating structure consisting of a periodic arrangement of a low refractive index material coated with a high reflective index layer (Figure 1). When the PC is illuminated with a broadband light source, high order diffraction modes couple light into and out of the high index layer, destructively interfering with the zeroth-order transmitted light[79]. At a particular resonant wavelength and incident angle, complete interference occurs and no light is transmitted, resulting in 100% reflection efficiency.

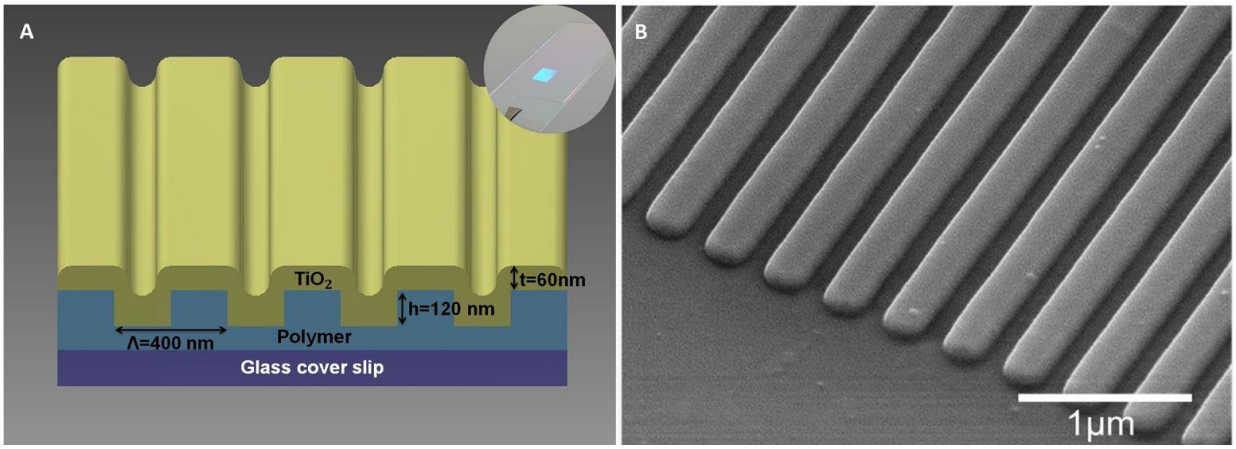

Figure 4.1 (a) Schematic diagram of the photonic crystal (PC) biosensor. A PC sensor is comprised of a replica molded polymer grating overcoated with a high refractive index thin film of TiO2. Inset: Photo of a PC fabricated upon a glass cover slip. (b) Scanning electron micrograph of the PC surface.

The resonant wavelength is modulated by the addition of biomaterial upon the PC surface, resulting in a shift to a higher wavelength. The electromagnetic standing wave that is generated at the PC surface during resonant light coupling inhibits lateral propagation, thus enabling neighboring regions on the PC surface to display a distinct resonant wavelength that is determined only by the density of biomaterial attached at that precise location. By measuring the resonant peak wavelength value (PWV) on a pixel-by-pixel basis over a PC surface, an image of cell attachment density may be recorded. PWV images of the PC may be gathered by illuminating the structure with collimated white light through the transparent substrate, while the front surface of the PC is immersed in aqueous media.

The advantages of PC-based surfaces for cell attachment imaging are compelling. As a label-free technology, cell attachment to a PC sensor is measured without the use of dyes or stains, so a population of cells can be measured repeatedly without disrupting their culture environment. The detected output signal is highly quantitative, providing measurements that are repeatable between sensors, instruments, and laboratories without photobleaching. PC biosensors are fabricated from inexpensive materials and require only low intensity illumination from beneath the sensor, so no electrical or physical contact between the sensor and the detection system occurs, and illumination does not pass through the cell body, the cell media, or the liquid-air meniscus of a microplate well. The PC biosensor strictly limits lateral propagation of resonantly coupled light, enabling imaging-based detection with resolution sufficient for measuring subtle variations in cell adhesion strength within a single cell, without needing to pre-tune the sensor to a particular resonant coupling condition, as in SPRi. PC biosensor imaging provides information that is fundamentally different than that provided by an optical microscope, as the sensor responds to local variation in cell attachment strength to the transducer surface. The sensor can be prepared

with a variety of surface functionalizations (such as matrix coatings, antibodies, and peptides) and thus can be used as a tool for measuring how cell attachment to surfaces is modulated by drugs, growth factors, or other environmental factors.

4.3 Hyperspectral imaging microscope detection instrument

A schematic diagram of the PCEM instrument is shown in Figure 2. The system is built upon the body of a standard microscope (Carl Zeiss Axio Observer Z1), but in addition to ordinary bright field imaging, a second illumination path is provided from a fiber-coupled broadband LED (Thorlabs M617F1, $600 < \lambda < 650$ nm). The fiber output is collimated and filtered by a polarizing beam splitter cube to illuminate the PC with light that is polarized with its electric field vector oriented perpendicular to the grating lines. The polarized beam is focused by a cylindrical lens

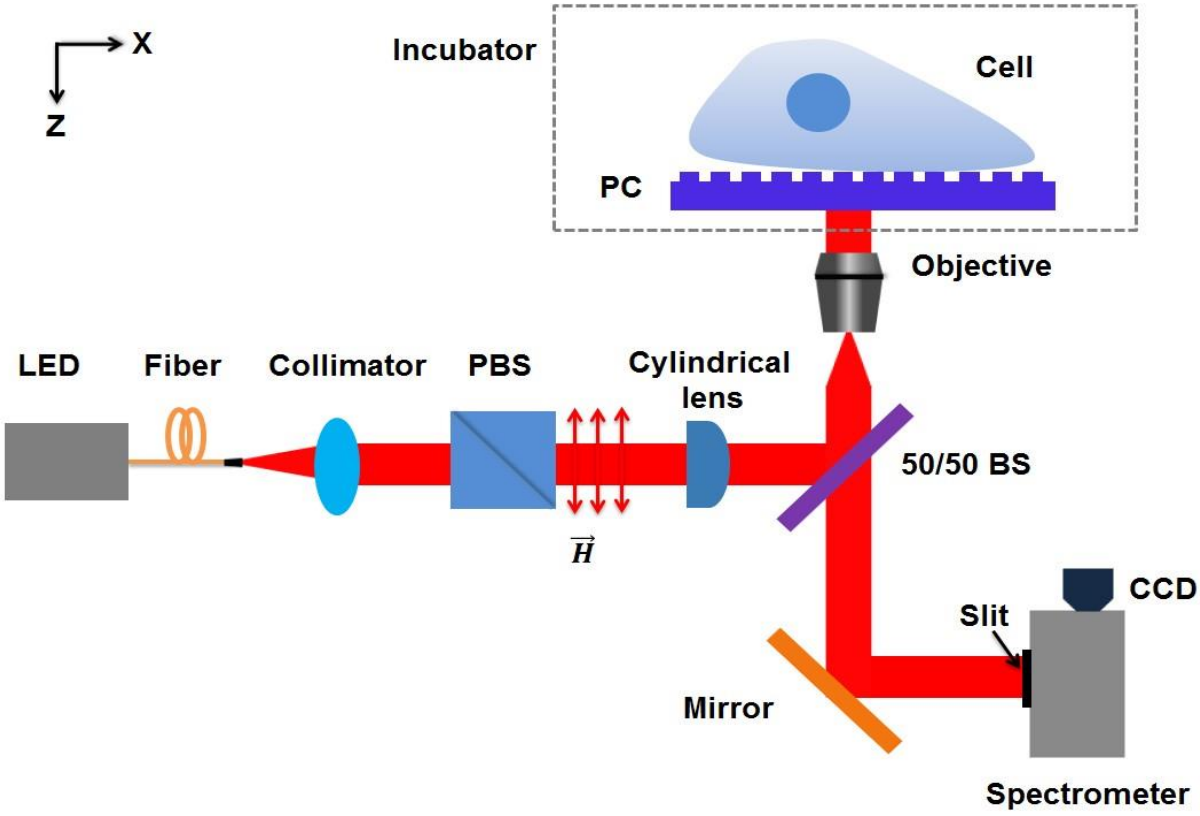

Figure 4.2: Instrument schematic of the PCEM. Illumination from a fiber-coupled LED is collimated and passed through a polarizing beamsplitter (PBS) to create a pure electric field polarization perpendicular to the PC grating. A cylindrical lens focusses the light to a line at the back focal plane of the objective. The PC resonantly reflects only a narrow band of wavelengths, which are collected through the entrance slit of an imaging spectrometer.

(f=200 mm) to form a linear beam at the back focal plane of the objective lens (10x, Zeiss). After passing through the objective lens, the orientation of the line-shaped beam is rotated to illuminate the PC from below at normal incidence. The reflected light is projected, via a side port of the inverted microscope and a zoom lens, onto a narrow-slit aperture at the input of an imaging spectrometer. The width of the adjustable slit was set to 30 μm for the work reported here. Using this method, reflected light is collected from a linear region of the PC surface, where the width of the imaged line, 1.2 μm, is determined by the width of the entrance slit of the imaging spectrometer and the magnification power of the objective lens. The system incorporates a grating-based spectrometer (Acton Research) with a 512 × 512 pixel CCD camera (Photometrics Cascade 512). The line of reflected light, containing the resonant biosensor signal, is diffracted by the grating within the spectrometer (300 lines/mm) to produce a spatially resolved spectrum for each point along the line.

Therefore, each pixel across the line is converted to a resonant reflection spectrum, containing a narrow bandwidth ($\Delta\lambda \sim 4$nm) reflectance peak from the PC. The Peak Wavelength Value (PWV) of each peak is determined by fitting the spectrum to a 2nd order polynomial function, and then mathematically determining the maximum wavelength of the function. By fitting all 512 spectra, in a process that takes 20 msec, a line comprised of 512 pixels is generated that represents one line of a PWV image of the PC surface. With an effective magnification of 26x, each pixel in the line represents a ~ 0.6 μm region of the PC surface and 512 such pixels cover a total width of ~300 μm. To generate a two- dimensional PWV image of the PC surface, a motorized stage (Applied Scientific Instruments, MS2000) translates the sensor along the axis perpendicular to the imaged line in increments of 0.6 μm/step. Using this technique, a series of lines are assembled into an image at a rate of 0.1 sec/line and the same area on the PC surface can be scanned

repeatedly. Each image is comprised of 512 by *n* pixels, where *n* can be selected during each scan session, and each pixel represents a 0.6 x 0.6 μm region of the PC surface. A biosensor experiment involves measuring shifts in PWV. A baseline PWV image is gathered before the introduction of cells, when the PC is uniformly covered by cell media, which is aligned and mathematically subtracted from subsequent PWV images gathered during and after cell attachment.

4.4 Characterization of the PC sensitivity and resonant wavelength stability under cell culture conditions

In preparation for cell attachment demonstrations, the ability of the PCEM to measure shifts in the bulk refractive index of the cell media was established. First, exposing the entire PC surface to distilled water (n = 1.333) and subsequently exposing the same sensor to isopropyl alcohol (n = 1.377), we confirmed that an individual pixel within a PCEM image demonstrates high reflection efficiency and narrow resonant reflection bandwidth. The PWV shift measured from a single pixel exposed to both media yielded a bulk refractive index sensitivity of $\Delta\lambda/\Delta n$ = 102 nm/RIU.

A series of PWV images were gathered over a 12-hour period to demonstrate PWV stability with the PC exposed to cell media at the elevated temperature (T = 37 ˚C) and 5% CO_2 environment used for biological studies. Ham's F12 media (Invitrogen) was placed in a PDMS well attached to the PC surface. The average PWV shifted by only 0.12 nm over 12 hours, and the standard deviation of PWV within an image of a PC uniformly exposed to cell media was 0.09 nm.

The most commonly used method for identification of differentiating stem cells is the labor- and time-intensive methylcellulose assay, which only reveals the identity of the colonies weeks after commitment occurs[131-133]. Furthermore, this approach requires cells to be resuspended

in liquid phase, thereby altering many of the environmental cues that yielded the observed differential development. Using PCEM, it is possible to capture the dynamics of cell morphology and cell-matrix interactions during complex processes such as stem cell differentiation under real-time conditions (with less than 60 seconds between subsequent images). Such a tool would be critical for examining the potential of cell attachment signatures as a proxy for stem cell lineage commitment, particularly considering such analyses could be performed without disturbing the extracellular environment.

As cells attach and spread, positive PWV shifts are observed due to an increase in the concentration of cellular material within the evanescent field region of the PC. A PWV image for human pancreatic cancer cells (Panc-1) is compared to a brightfield image of the same cells in Figure 4.3. Morphological profiles are consistent with healthy, attachment-dependent cells. Representative spectra are shown from inside and outside the cell region, demonstrating a definitive whole-spectrum shift of the characteristic resonant peak. Clearly visible boundaries of ~ 0.5 nm PWV shifts demonstrate the ability of PCEM to provide information about the geometry of attachment, which has been shown to have significant implications for both the classification of differentiating stem cells[134], and the metastatic potential of tumor cells[135]. In addition, sub-cellular variation of PWV is indicative not only of the presence of cellular adhesion, but also modulation in the strength of attachment. For example, cell '2' in Figure 4.3 shows a gradient in cell attachment strength from left to right. A region of greater PWV shift along the leading edge suggests the formation of lamellipodia, indicating a higher concentration of intracellular matter than is present in the rest of the cellular attachment footprint. As it can be assumed that the majority of this lower-PWV shifted footprint occurs under regions of cytosol, the increased PWV of the cell boundary, especially in these protrusions, most likely can be attributed to the formation of actin bundles at

sites of focal adhesion, a process thoroughly documented via traditional, yet cytotoxic, fluorescent staining techniques.[136-138]

4.5 Label free imaging of stem cell attachment and drug-induced apoptosis

Next, murine dental stem cells (mHAT9a) were cultured and allowed to attach to a PC surface prepared with fibronectin over a period of two hours (Figure 4.4a). From the series of PWV

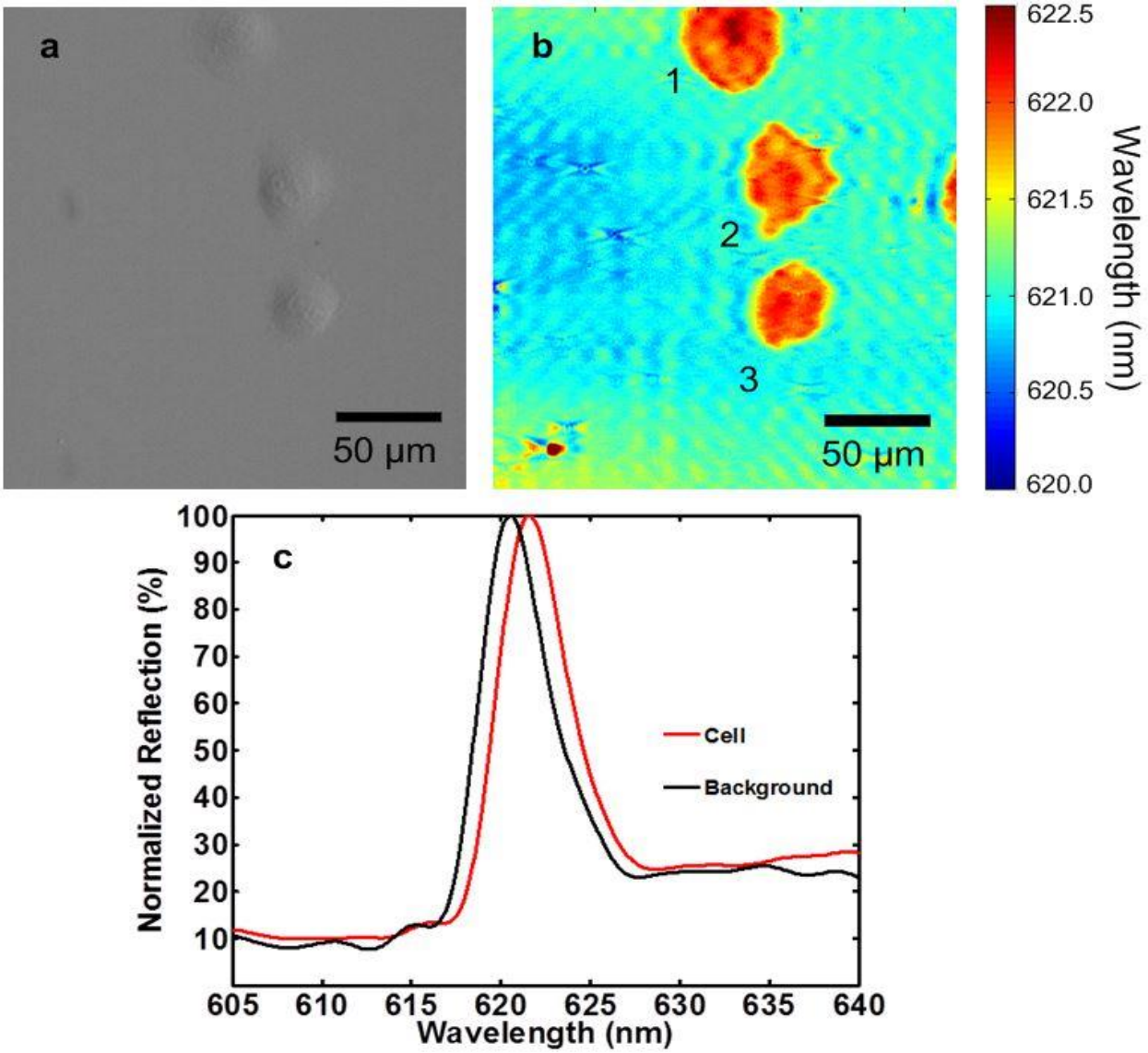

Figure 4.3 (a) Bright field and (b) PWV imaging of Panc-1 cells attached to the PC surface. Cells were seeded onto a fibronectin-coated sensor and allowed to incubate for 2 hours before imaging. Lamellipodial extensions are visible, especially from cell 2, demonstrating the ability of PCEM to resolve regional differences in single-cell attachment. Darker shading indicates regions of higher protein concentration, and is present in regions near the boundary of lamellipodia formation, consistent with the creation of actin bundles. (c) Representative regions of cellular attachment. Selected areas of the PWV image from beneath a cell show the PWV shift of a typical Panc-1 cell is ~1.0 nm, and consistent throughout the entire spectrum at those locations.

images gathered at 3 minute intervals, initial attachment times can be identified within the 3-minute period of image acquisition. Cells are observed attaching to the treated surface, with initial attachment characterized by small, round areas of PWV shift, consistent with spherical cells exiting suspension. As time progresses, average cell diameter increases, and membrane boundaries become more irregular as cellular processes begin to extend from cell bodies. Many cells maintain highest shifts at their periphery, which is consistent with the high concentration of cytoskeletal protein necessary for boundary maintenance and lamellar extension[139]. Random locomotion is observable, which reveals that cellular detachment results in a full recovery of initial PWV values when a cell moves to a new location. We observe no preference for the cells to extend themselves or to move along the direction of the PC grating.

Cellular apoptosis and detachment were also studied. Using another fibronectin-treated PC biosensor, mHAT9a cells were allowed to attach to the sensor surface for 3 hours. A final concentration of 2 μM staurosporine, shown to induce apoptosis via protein kinase inhibition[140,141], was added to the cell chamber and mixed for 15 seconds. Cells were imaged every 20 minutes for 18 hours (Figure 4.4b). Initial cells appear healthy, with various filopodia extending radially from cell bodies. As time progresses, the footprint of the cell bodies decreases, and several of the cells appear to detach completely. Other cells appear to undergo apoptosis prior to detachment, leaving behind remnants of cell membrane, which still produce a detectable PWV shift. The breakdown and modification of cell-cell and cell-ECM interactions is of great importance to answering questions about the progression of cancer cell detachment and metastasis from primary tumor sites.

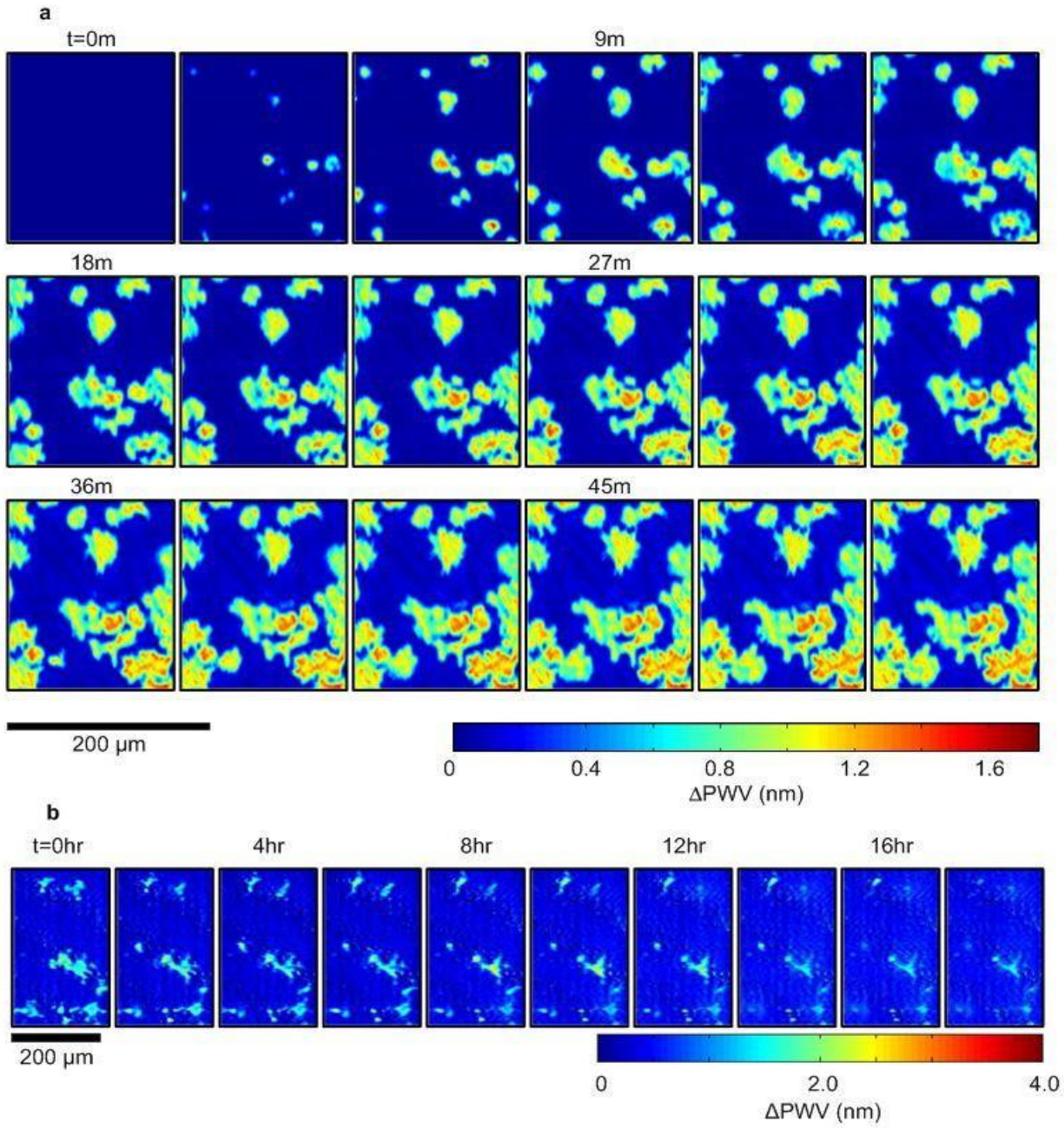

Figure 4.4 (a) Time lapse PWV images of cellular attachment of mHAT9a cells. Cells were seeded at 20,000 cells/ml on a fibronectin-coated sensor surface. After 3 minutes, regions of initial cell attachment appear as small, round regions, consistent with spheroid, trypsinized cells coming out of suspension and attaching to a surface. As time progresses, both the size of the cells and intensity of the PWV shift induced by them increases, indicating a higher localization of cellular material at the sensor surface, which can be expected during cell spreading. Finally, once cells are sufficiently attached, cellular processes can be observed sensing the cells' microenvironment in all directions. The outer irregular boundaries of the cells have a relatively low PWV, consistent with thin, exploratory filopodia, accompanied by a more heavily attached region slightly immediately adjacent in the cell interior, likely a result of actin bundle formation. (b) Time lapse PWV images of mHAT9a apoptosis and detachment. Cells were seeded at 8,000 cells/ml onto a fibronectin-coated sensor surface. Cells that detach can be observed by the gradual retraction of filopodia and overall cell rounding before the PWV shift disappears entirely. Some cells appear to undergo apoptosis while still attached, leaving remnants of cell membranes and protein on the sensor surface. ΔPWV data was attained **via background subtraction from initial image taken before cell attachment (t = 0).**

PCEM is unique in the fact that the biosensor response is a direct quantification and 2D localization of attachment at the single cell level, as opposed to indirect methods of staining for actin bundle formation or even ensemble averaging of bulk dielectric properties. This direct observation available over a time scale of hours to days provides a natural tool for the future study of cancer cell detachment and metastasis.

4.6 Label free imaging of stem cell chemotaxis

We next sought to validate the use of PCEM imaging in examining cell-mediated chemotaxis. The importance of stromal cell-derived factor-1 (SDF-1α) in the directed chemotaxis of differentiating cells is well-known for a myriad of situations including hypoxic ocular neovascularization, capillary formation and adipocyte differentiation in human adipose tissue, and bone regeneration in traumatic brain injury[142-144]. More recently, SDF-1α and its effect in attracting CXCR4 receptor positive cells have been investigated in dental healing and regeneration. However, current mechanisms for studying the recruitment of dental stem cells have been based on fixing and staining cells[145,146]. As the observed migration occurs on the order of days, label-based assays are not feasible for extended time course studies. PCEM provides an opportunity to monitor such events as they occur.

We examined mHAT9a chemotaxis in response to beads soaked in SDF-1α, a chemoattractant to which the receptor CXCR4 is sensitive[147] (Figure 4.5). After a bead was placed on the sensor surface, attached cells were observed to move in the direction of the eluting bead. Probing lamellipodia extend in multiple directions around the cell, but only projections formed in the direction of the bead are maintained by the migrating cells. Attachment in the trailing edge of the cell decreases over time as the cell bodies proceed in the direction of chemotaxis, resulting in

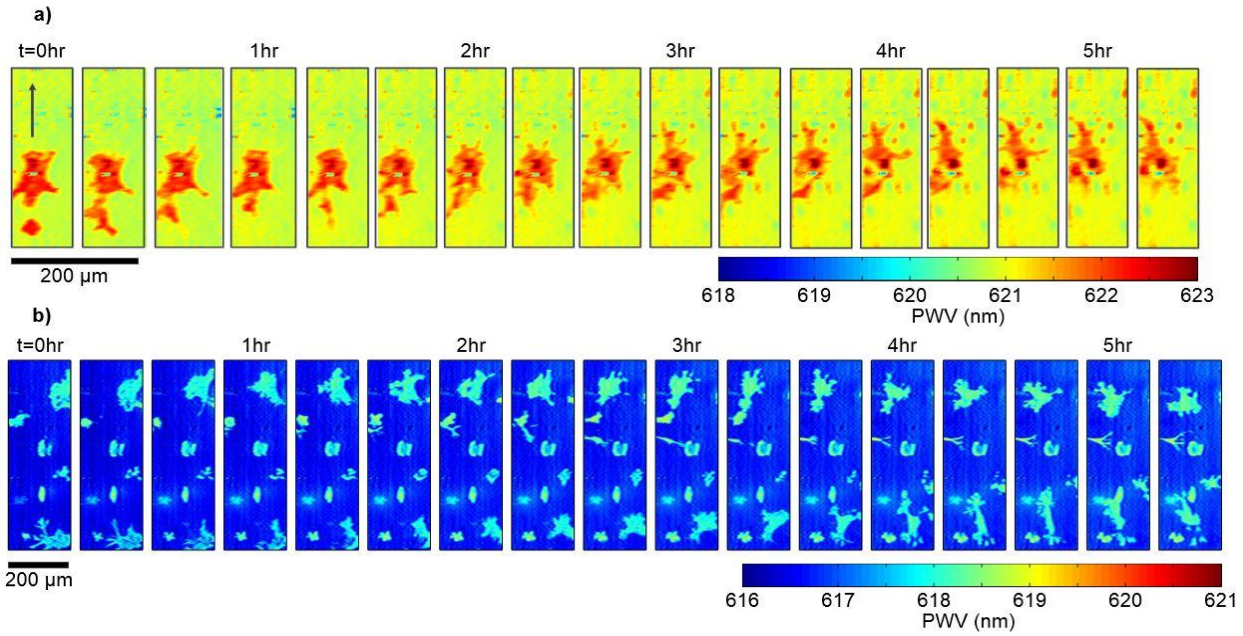

Figure 4.5 (a) Time lapse PWV images of chemotaxis of mHAT9a cells. Cells were deposited on the sensor surface at a concentration of 8,000 cells/ml and allowed to attach for 2 hours before imaging. An agarose bead was placed at a location approximately 100 microns above the top of the image, and PWV images were collected every 20 minutes after the bead was placed. Cell movement direction is indicated with an arrow in the leftmost frame. (b) CXCR4 knockout cells exhibit non-directional movement on the sensor surface. Similarly prepared, CXCR4 mutants do not show directional movement toward the bead, demonstrating that the previously observed directional locomotion was due to chemotaxis.

a return of the sensor to its native state. The experiment was repeated with a mHAT cell line with a constitutive knockout of the CXCR4 coding gene, and no directional movement was observed. This suggests that the observed cellular movement was indeed due to chemotaxis, as opposed to nonspecific locomotion. Critically, we do not observe preferential movement or extension of cell processes in the direction of the PC grating lines. To our knowledge, this represents the first label-free time-lapse imaging of the attachment localization of living cells during chemotaxis.

It has been shown that SDF-1α/CXCR4 mediated recruitment of dental stem cells is likely an important inflammatory response and underlying promoter of reparative dentin formation[148]. Further investigation of the SDF-1α/CXCR4 pathway with the PCEM technology could provide a valuable investigation of morphological changes induced by the inflammatory response of dental stem cells to dental damage.

4.7 Conclusions

PCEM represents a new imaging modality that can be easily integrated with a conventional optical microscope to enable quantified, near real-time, high resolution imaging of cell-surface interactions. While traditional microscopy techniques such as phase-contrast and DIC provide basic information about cellular morphology and general appearance, PCEM provides information that is specific to the interface between the cell and its substrate. By virtue of the surface-confined resonant electric field of the photonic crystal, PCEM enables high contrast imaging of the interaction strength of cells with a surface, providing a specific attachment footprint as opposed to a generalized shape of the entire three-dimensional cell body. The approach utilizes low power illumination from a visible wavelength LED from below, using a PC sensor structure that can be incorporated into standard coverslips (as demonstrated here), microscope slides, or microtiter plates that are typically used for cell research. PCEM clearly demonstrates that cell-surface attachment strength is not uniformly distributed within a cell or static as a function of time, but instead contains rich dynamic information that includes the rate of cell boundary extension, the size of a cell "footprint" on a surface, and the effect of the extracellular environment (including chemotactic gradients) on cell attachment.

The cell imaging experiments used to demonstrate PCEM were selected to show that the spatial resolution of the approach is sufficient for clearly observing features such as spatial gradients in cell-surface attachment and the extension of fine-structured filopodia, attributes that are typically observed only using dyes or stains. As a label-free detection approach, PCEM enables continuous monitoring of these phenomena over extended time periods that are compatible with the biological time scales of chemotaxis, apoptosis, differentiation, and proliferation. This work

demonstrates, to our knowledge, the first time-lapse movies of cell-surface interaction monitoring at these time scale.

It is already well-established that both the comparison of cancerous/non-cancerous cells and of cell lineages differentiated from pluripotent stem cells lend themselves to investigation via their unique morphologies and cellular attachment protein expression, with the majority of such differences easily visible via traditional microscopy. With PCEM, cellular attachment morphology can be directly observed, and attachment 'profiles' for different cell types can be developed. By limiting the study of cell morphology to the specific density of cellular material present in the evanescent field region of a photonic crystal, attachment can be observed in a more direct method with less subjectivity than simple qualitative observation using traditional microscopy methods.

There is an increasing awareness of the importance of cellular adhesion and the mechanical microenvironment of cells on their behavior, yet directly measuring these attributes in a non-invasive fashion has proved difficult. PCEM provides a novel, robust methodology for the investigation of these attributes in a controlled environment without chemical alteration. The relationship between mechanical microenvironmental cues and cancer cell behavior has been demonstrated, contributing significantly to tissue dysplasia and metastatic detachment[149]. With PCEM, it will be possible to investigate important components within the progression of tumor-development, such as the recruitment and movement of neutrophils to the cancer microenvironment. Neutrophil polarization and chemotaxis represents a challenging process to study as it presents a complex and dynamic set of cellular-ECM interactions. Near real-time imaging would allow for rapid improvement in our understanding of this and the other biological applications discussed herein, providing dynamic attachment information that is not currently available.

Similarly, the resolution demonstrated in this chapter with which subcellular localization of filopodia and focal adhesions were observed provided the first suggestion that other biodetection opportunities requiring high spatial resolution might be possible. In combination with the previously demonstrated smartphone-based spectrometric optics, I began thinking about specific point-of-care clinical challenges that remained unsolved that might be addressed with a portable version of the PCEM instrument, and settled on HIV viral load, as will be discussed in Chapter 5.

CHAPTER 5: HIV DETECTION USING PCEM FOR POINT-OF-CARE TESTING

5.1 Introduction

In Chapters 2 and 3, I demonstrated the full design cycle from ideation through prototyping, and a successful handoff to a corporate partner who will commercialize the technology. In Chapter 4, I describe the use of PCEM as a new technology to further enhance the sensitivity of the PC-modality of spectral biosensing by re-introducing the second spatial dimension. In this chapter, I seek to apply the same PCEM technology to a specific point-of-care application that would significantly benefit from the increase in sensitivity resultant from digital detection of individual nanoscale attachment events. To this end, this chapter will begin with specific background information on HIV viral load testing, and why it is ideally suited for development as a PCEM-based digital-detection assay. Then, demonstration of the single-particle resolution of the benchtop PCEM setup will be described and validated with non-HIV antibody capture experiments. A thorough discussion of the HIV Env protein is included to provide important context and relevant background for the second experimental section (Section 5.4) where HIV viral attachment events will be investigated. At the end of the chapter, a discussion of important considerations relevant to the design of the portable PCEM instrument will be included based upon 1) optical design considerations from Chapters 2 and 3, 2) human factors considerations from Chapter 4, and 3) practical considerations from both the usage case of the eventual device (Section 5.1) and the physical structure of HIV (Section 5.3).

5.1.1 Background and Motivation

HIV/AIDS has presented itself as one of the most serious public health challenges facing the world today [150]. Since its emergence as a global pandemic 30 years ago, AIDS has claimed the lives of over 25 million people and increased global disability-adjusted life years (DALYs), a measurement of global disease burden, by 351% over the past 20 years [151]. Having recognized HIV/AIDS as a true pandemic, initiatives such as the President's Emergency Plan for AIDS Relief (PEPFAR) and the UN Millennium Declaration have specifically targeted reversal of the spread of the disease as a key area to improve the health, economic security, and overall wellbeing of the global population [150,152]. While great strides have been made toward reversing the spread of HIV infection, it remains a significant threat to global health with over 35 million people currently infected, and remains the leading cause of mortality of young women in low- and middle-income countries [153,154]. In addition to a heavy gender-discrepancy in burden, the disease is disproportionately found in sub-Saharan Africa, which accounts for 69% of the global population living with HIV but only 12% of global population [150]. Increasing access to antiretroviral therapy (ART) is a leading cause of the decrease in AIDS-related deaths [155]. Plans to increase the penetration of available treatment to areas of high disease burden are ongoing, but often the infrastructural requirements and cost-prohibitive nature of current diagnostic equipment needed for proper treatment selection and monitoring prevents successful deployment of such strategies in primary and secondary-level facilities.

HIV viral load (VL) has long been known to provide meaningful clinical information about the progression of infection and development of AIDS by directly quantifying the number of virus particles present in patient blood [156-158]. Current methodologies used in commercial diagnostics rely heavily on nucleic-acid quantification via PCR to quantify the number of virus particles.

Nucleic acid quantification tests have been demonstrated as successful tools for measuring VL, but prohibitive features such as equipment cost, infrastructure demands, and technical expertise requirements make these gold-standards inadequate for the developing world [159-161]. A few enzyme linked immunosorbent assay (ELISA)-based tests have been developed to measure HIV RNA or RNA-associated proteins, such as the Cavidi ExaVir RT and PerkinElmer ultrasensitive p24 assays; however, these tests have received mixed reviews in regard to their high measurement variability and lack of sensitivity [162,163].

In addition to being able to detect the initial contraction of an HIV infection and risk of transmission to others in real time, VL measurement has been demonstrated as a key indicator for the monitoring of ART. For years, CD4+ T-cell levels and clinical observation were used as diagnostic indicators for treatment failure of antiretrovirals. These are still important tools for assessing the overall degradation of a patient's immune response, but due to the higher sensitivity and potential for earlier detection of treatment failure, VL has emerged as an increasingly important component of current and future ART monitoring strategies [164]. Beginning in 2010, VL testing became the WHO-preferred approach to ART monitoring whenever possible and, with the adoption of the WHO June 2013 Consolidated ART guidelines, became the only clinical approach to be recommended for assessing virologic failure and beginning second-line treatment [154,155]. These guidelines suggest initial VL testing after 6 months of ART and annually thereafter. Upon a measurement of VL greater than 1000 copies/mL, a second VL test administered after a three-month period of strict ART adherence is considered justification to switch ART regimens in all patient populations.

5.1.2 Limitations of Current Techniques for the Point-of-Care

Current standard-of-care tests in the US present lower limits of detection at 20 copies/mL. When translated to a point-of-care context, several significant challenges become evident. Standard blood plasma collection volumes for tests run on platforms such as the Abbott Xpert, Hologic Aptima, and Biomerieux NuliSens range from 1 to 1.2 mL, while a large finger prick can generate about 100 µL, resulting in a 20x decrease in plasma volume, and therefore RNA copies, for a point-of-care test. While further optimization may be possible, fundamental limits of PCR, such as the "Monte Carlo" effect, and even individual enzyme efficiencies[165] are likely already contributing factors. Assuming that 20 copies per PCR reaction is at the limit of what can reproducibly be quantified, the decrease in volume would result in a comparable amount of 200 virions per mL of whole blood, or 20 virions per 100 µL sample.

At 200 virions/mL, this represents a concentration in the sub-femtomolar range, which is beyond that of even the newest serological detection methods. The Quanterix Simoa™ system and the Singulex Erenna system and similar emergent high-end serology-based biosensing platforms have demonstrated detection down to the femtomolar range, but no less.[166-168] All of these systems all rely on some sort of signal amplification, be it enzymatic of replication-based. Just as PCR and other nucleic acid amplification techniques have demonstrated, when nearing the lowest limits of detection, any sort of amplification will introduce some noise and uncertainty into the measurement as at such low concentrations particles follow a Poisson distribution.

When discussing 20 virions per 100 µL sample, this leaves us looking for techniques that can identify each and every particle attachment event. Such "single particle" sensors have been demonstrated, and consist of two broad groups: imaging and non-imaging platforms, many of which the Cunningham group recently described in a review published in Chemosensors.[169] Such

single-particle detection techniques are optimal for situations such as point-of-care HIV viral load monitoring when simplicity of assay design (no thermocycling, no primer design, fewer reagents, etc.) and low-variability at low concentrations. Having already demonstrated sub-micron spatial resolution of cellular attachment processes, a logical next step is detecting single binding events using PCEM.

By utilizing plasmonic nanoparticles that absorb maximally at the resonance condition of a PC, spatially-resolved images of binding events can be monitored via repeated PCEM scanning, much as cellular attachment was, but at a smaller scale. In this chapter, I will first demonstrate the ability to detect single-attachment events using a standard serological binding event, I will then move on to discussion of the HIV Env protein, the only non-host material present on the external surface of an HIV virion, and will then present recent work on detecting and validating single HIV virion binding events via PCEM, which will inform the subsequent validation of antibody-HIV-antibody-nanoparticle complexes present on the PC surface and visible in PCEM images.

5.2 Single Nanoparticle Detection

In the sub-micron size regime, typical gravitational and buoyancy forces on particles (both HIV and nanoparticles) become secondary to diffusion, which has timescales of minutes to hours. As a result, one of the most important considerations for a POC device for viral load management that maximizes the capture of virions in a sample is the microfluidic channel height of the capture region, which strongly affects the particle settling time. This dimension, coupled with the width of the channel, the flow rate, and cross-sectional area, collectively determine the shape and size of the depletion zone around the sensor. For a useful primer on balancing fluid dynamic and mass transport considerations in the microscale regime, the reader is directed to a paper with several relevant, practical examples.[170]

To serve as a starting point for experimentation, COMSOL simulations were run with a variety of sensing geometries, and optimal starting parameters were identified (Figure 5.1). Simulations were run to understand the improvements to LOD that could be made by using a microfluidic device, compared to an experimentally-derived one, as previously reported for the static capture of HIV.[82] There were two key considerations for determining the sensor's theoretical LOD: a direct improvement of the previously achieved surface density (0.65 virions/mm^2, COMSOL), and capturing enough particles at the LOD to generate a reliable signal assuming at least 50% capture(3-8 virions). Based upon simulations, the optimal sensor should be 2-3mm in width with a height as short as possible (10µm was determined to be at the low-end of what might be possible to physically construct). At concentrations relevant for HIV viral load, it is crucial to minimize the fraction of cross-sectional area of the microfluidic channel that does not allow HIV passing through it to interact with the sensor surface. Manufacturing such a short, wide channel is an engineering challenge in-and-of-itself, and in parallel to preliminary

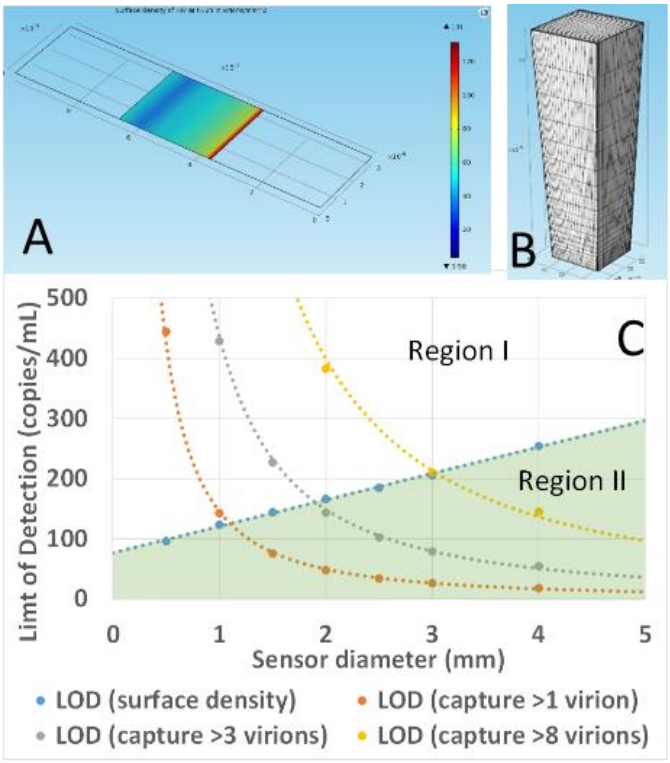

Figure 5.1. COMSOL modeling results. A. Representative image from microfluidic model showing time and position-based concentration gradients. B. Model used for representative 384-well plate well. Incredibly large height dimension, compared to that of surface area at the biosensing surface (bottom) presents a hydrodynamics challenge for attachment of virions to the surface. C. LOD for sensors of various parameters. In Region I, LOD is governed by a fundamental critical number of required virions present across the entire sensor, (orange, gray, and yellow dashes for critical number = 1, 3, 8 virions, respectively). In Region II, LOD is determined only by the surface density of captured virions, as in [167], (blue dashes). The optimal LOD for any critical number of viruses is the minima located at the intersection of Regions I and II.

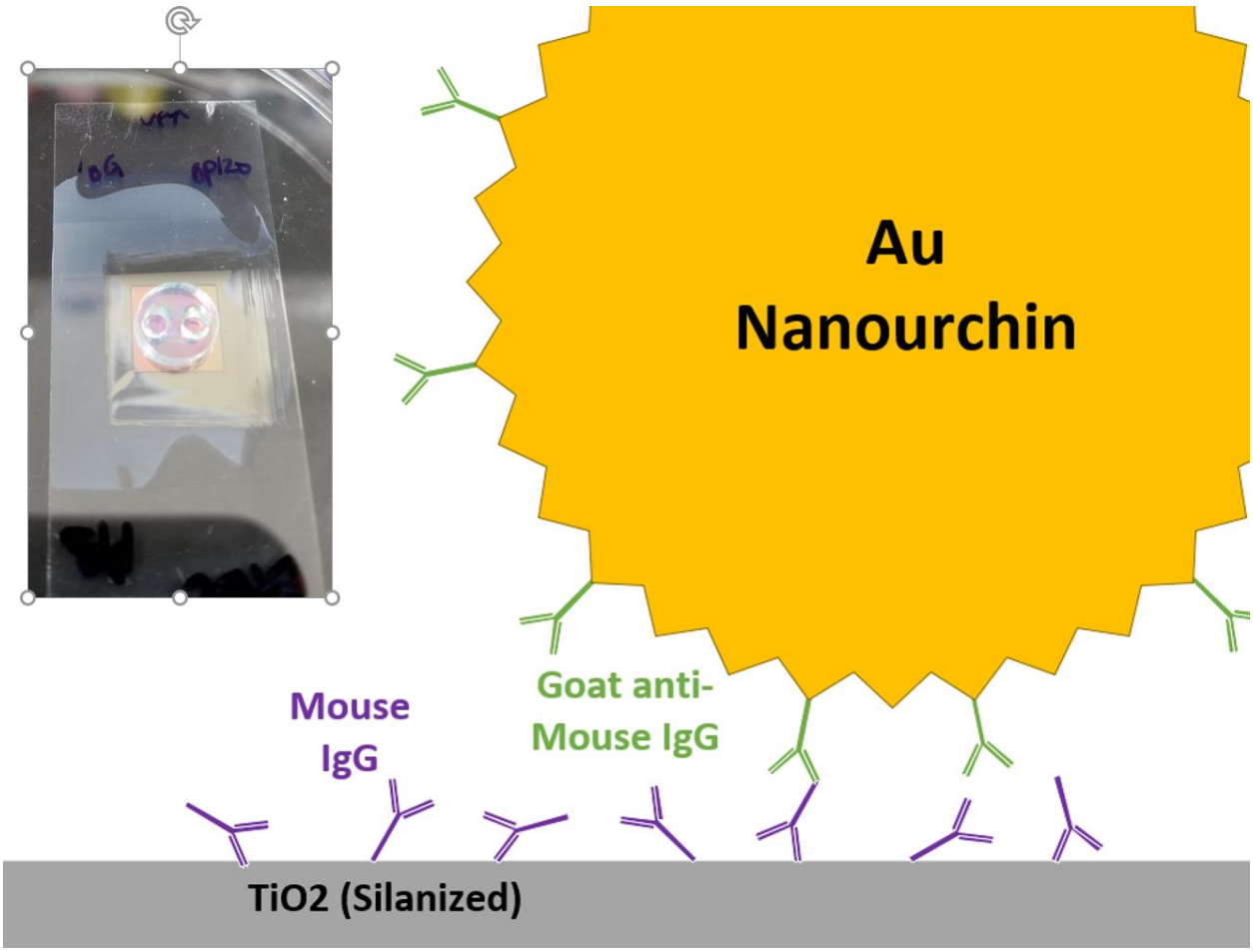

Figure 5.2 Detection scheme for proof-of-concept single nanoparticle attachment. Murine IgG is immobilized via epoxysilanization, and hircine anti-mouse IgG is linked to gold nanourchins via SH-PEG linkers. Figure is drawn approximately to scale. **Inset:** PDMS gasket for location-specific functionalization.

experiments discussed in this section, the development of the microfluidic device was initiated (Section 5.4.2).

To demonstrate the concept of single nanoparticle detection, we set up a simple serological capture assay with minimal biosafety concerns (Figure 5.2). A PC sensor was silanized with (3-Glycidyloxypropyl)trimethoxysilane (GPTMS), resulting in epoxide rings which will indiscriminately attach to any exposed primary amine group on proteins. A PDMS gasket was attached to the sensor surface with two wells, an active area and a control (Figure 5.2 inset). Next, mouse IgG antibody was incubated on the surface overnight, and then washed with PBST three times. The prepared sensor was placed on the PCEM and scanned.

Detection nanoparticles were prepared using commercially available gold nanourchins (Sigma). Briefly, goat anti-mouse IgG was linked with SH-PEG via NHS, EDC chemistry. After successful functionalization with SH-PEG, the resultant SH-PEG-IgG solution was mixed with gold urchins. The ideal volume of Sh=PEG-Ab was determined to be approximately 12 µL via DLS, corresponding to a 12-nm bathochromic shift in absorbance peak for the nanourchins. Functionalized nanourchins were incubated on the sensor, and serial scans were completed twice per hour. After between two and three hours, the nanourchins were removed, and the sensor was once again washed 3x with PBS.

Next, the sensor was observed via SEM, and patterns of attachment were observed (Figure 5.3). In the inset of the figure, an overlay of the SEM and PCEM images shows clear recognition of each of 7 nanoparticles in the PCEM image. Spreading in the direction orthogonal to the PC grating is a result of the PCEM stepper motors used, which can only move in increments of .1 nm, whereas the "true" step distance to achieve a square 'pixel' is .16 nm. For all scans discussed subsequently, a .1 nm step size was utilized, resulting in images that must be stretched by a factor of 1.6 in image postprocessing.

Clearly the reliance on minor defects or holes in the PC surface as landmarks is not ideal, so a gridded pattern to track spatial location on the macroscale for correlation between PCEM images and SEM (as well as between steps that require the sensor to be removed from the microscope, as required by BSL2+ safety protocols for future HIV work) was devised. A photomask was designed with a grid pattern (Figure 5.4), and transferred to the surface via photoresist patterning, exposure, and removal of some of the PC's TiO_2 layer (Figure 5.5). The resultant device allows for the 2D location to be recorded using a labeled coordinate system of etched "pixels" so that any 50 μm^2 scan area will be within 50 µm of a coordinate location (fine

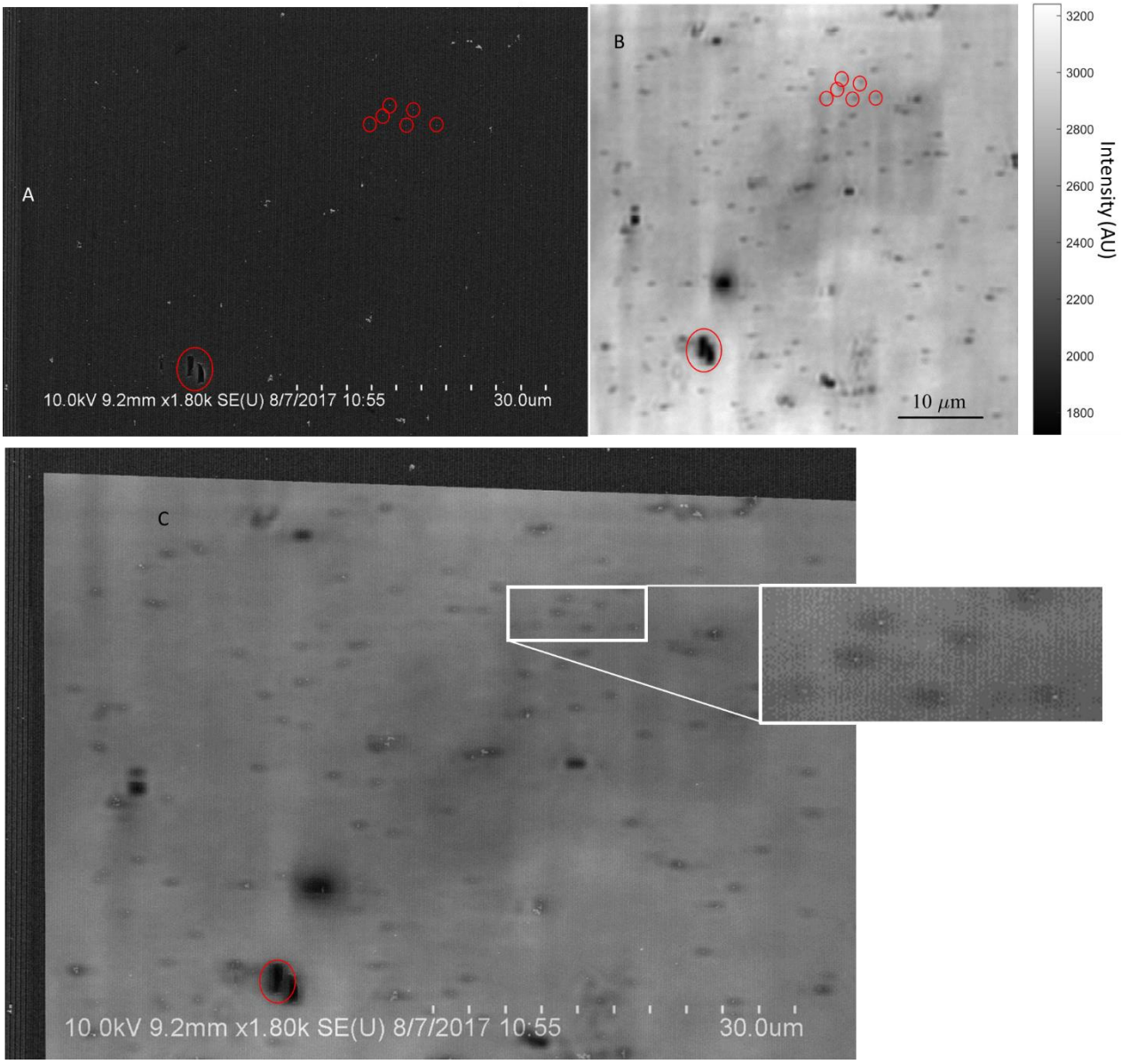

Figure 5.3 Validation of PCEM Images with SEM. A. SEM, B. PIV image from PCEM and C. Composite image of the same location on a PC. Defects used to align images from different sources are circled in each image. The top two images are the unaltered images resulting from data acquisition using each platform. C. Overlay of the two images with appropriate transformations: stretch, rotation, and zoom. Inset shows the seven nanoparticles discussed.

grid, for use with 40x objective). The coarse grid is for possible use with a 10x objective. Grids were centered at distances to match the locations of the centers of wells in the PDMS gaskets used for functionalization and incubation. Once grids were tested and validated on the PCEM and SEM, we prepared to begin experiments with HIV-based chemistry.

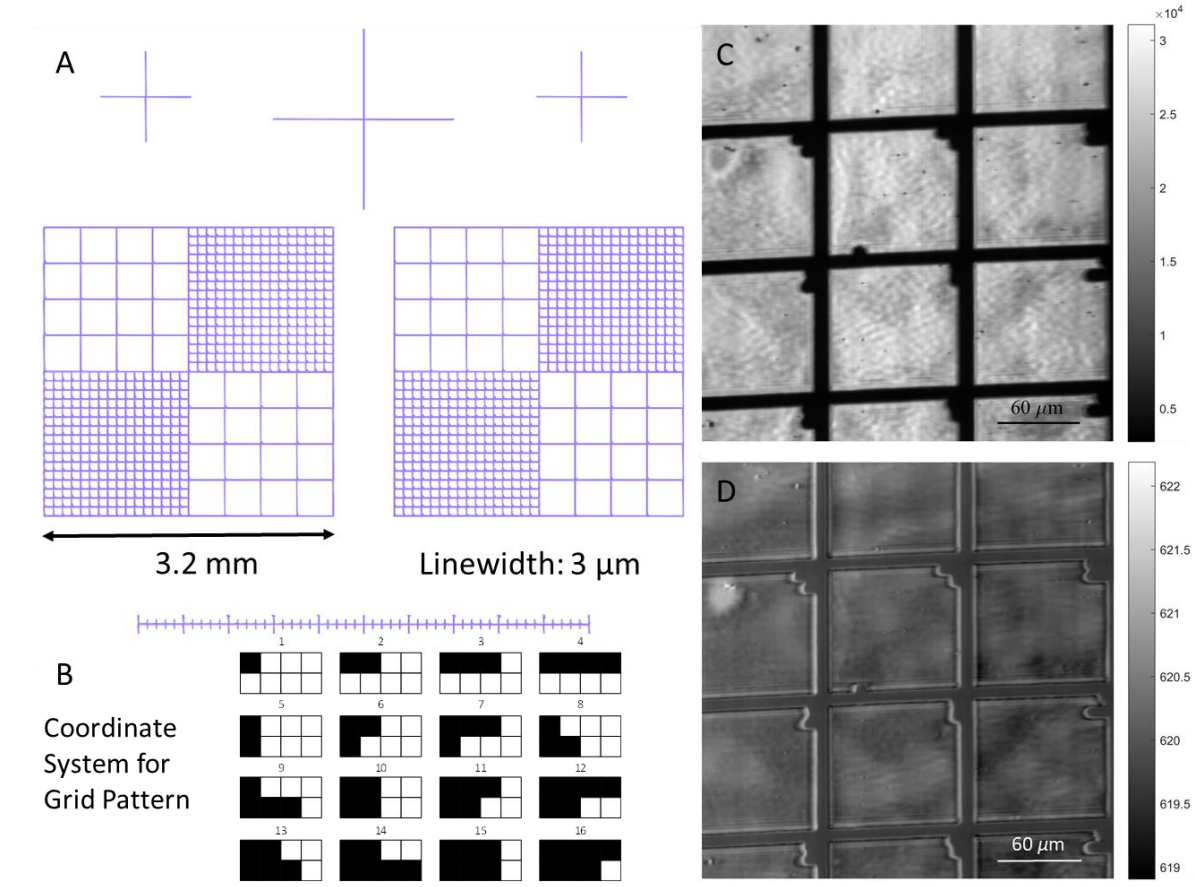

Figure 5.4 A. Photomask design and pattern. B. Coordinate system for each grid. C. PIV and D. PWV images of patterned grid on a PC

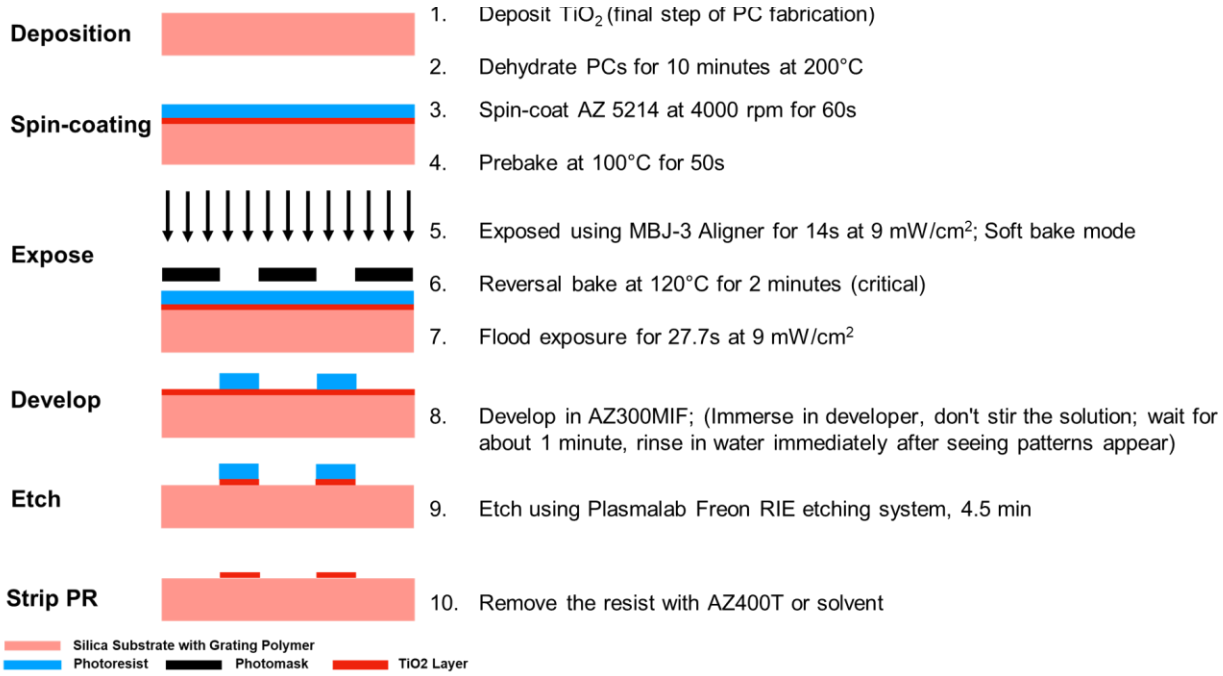

Figure 5.5 Fabrication procedure for etched grid for photonic crystals.

5.3 The HIV Env Protein Complex

As direct-detection of HIV is not a standard method of quantification, it is important to have a thorough understanding of the underlying structure and function of the target protein for viral capture, the Env protein. Knowing that HIV persists as a latent infection in spite of immune responses, and that the Env protein is the only viral protein expressed on the surface, I performed a thorough review of current work relating to the structure, action, and function of the protein as it facilitates host-cell attachment, entry, but also immune-avoidance.

The surface of HIV is comprised of a lipid bilayer assembled from the host cell with multiple copies of a protein spike, Env, which facilitates its tropism, attachment, and entry. These spikes are made of a mushroom-shaped trimer of heterodimers of proteins gp120 and gp41, which are generated from a common gp160 precursor, and comprise the surface (SU) and transmembrane (TM) portions of the spike, respectively (Figure 5.6).[171] These spikes are assembled as part of the outer membrane via the cytoplasmic domain of gp41 (gp41CD) which serves to target mature gp160 to inner-leaflet-tethered developing virions. This gp41CD region is also responsible for minimizing the amount of Env expressed on the cell surface. By having endocytotic motifs that interact with clathrin pits,[172,173] the envelope protein itself is able to maintain a low level of expression to maximize evasion of the immune system. While this strategy does decrease potential for immune recognition, the most significant component of successful HIV Env-based evasion of immune detection lies in the fundamental structure of the protein complex.

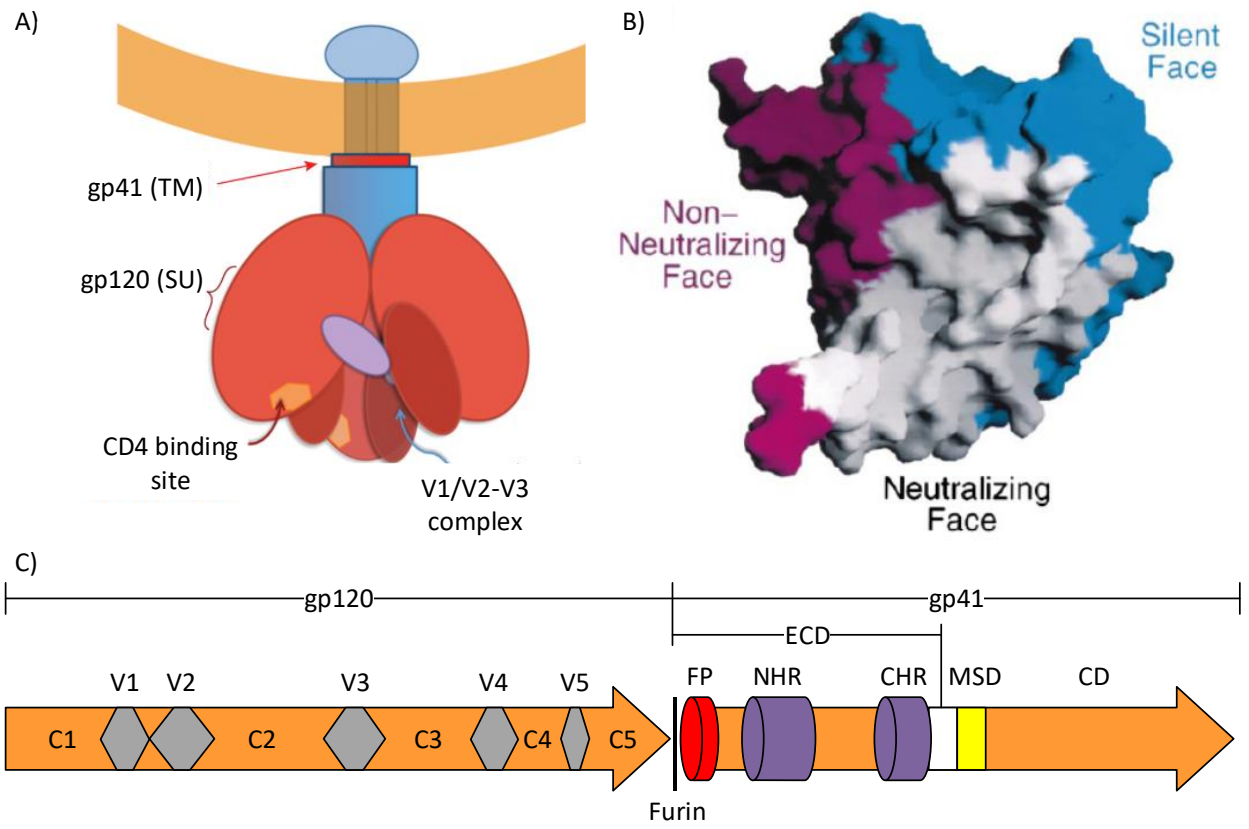

Figure 5.6 A) Schematic of the env protein. TM and SU components are shown, as is basic structure. Rusert, adapted B) Surface profile of the three faces of the gp120 core monomer. The gp120 core is seen from the perspective of CD4, and is oriented with the viral membrane at the top of the figure and the target cell membrane at the bottom.[189] C) Domains of HIV-1 Env. The gp140 precursor is cleaved into the surface subunit (gp120) and transmembrane subunit (gp41) in the Golgi complex at the furin site indicated. gp120 contains five variable domains (V1-V5) and five constant domains (C1-C5). gp41 consists of an extracellular domain, containing the fusion peptide (FP), and the heptad-repeats (NHR and CHR), a membrane-spanning domain (MSD), and a cytoplasmic domain (CD).[176, adapted]

5.3.1 Structure of Env

HIV gp160 is a precursor protein containing both proteins necessary for forming the Env structures present on the surface of a mature virion. In the Golgi, this protein is cleaved by a furin protease, allowing the resulting gp120 and gp41 to organize into heterodimers, and then collect during virion formation into trimers resulting in a final, mature Env.[174] Functionally, gp41 serves two purposes: membrane anchoring, and mediating membrane fusion with the host cell. Non-covalent bonds serve to attach gp120 to gp41, which functions as the interface between the virion and the outside world, responsible for host-cell recognition and immune system evasion.

Structural elucidation of gp120 has historically been of significant interest to scientists interested in vaccine design. However, one of the unique attributes of HIV that makes it so successful at immune evasion also has historically confounded attempts to determine its structure: the remarkable physical flexibility of the protein and ability to adopt multiple confirmations with significant differences in shape and relative distances between subcomponents.[175-178] The primary structure of gp120 can be described as five constant domains, which are highly conserved and responsible for the binding of CD4, interspersed with five variable domains, which are responsible for the broad heterogeneity resulting from the rapid rate of genetic mutagenesis (Figure 5.6C). Most of these variable domains are separated from the rest of the protein with disulfide bridges of cysteine-cysteine residues, which help in the tertiary folding of the protein.[174]

The primary functions of gp120 are to target HIV to its preferred host cells (CD4+ T cells), and to evade a host immune response. Though some work has demonstrated CD4-independent entry of HIV,[179,180] the most common process begins with CD4 binding of a highly conserved pit in the core of the protein, which introduces a conformational change in the Env protein, which both reveals the secondary binding site for a targeting coreceptor (either CXCR4 or CCR5), and induces changes in the gp41 fusion machinery.[178]

The first successful model of gp120 was published in 1998 in an article and letter in Nature by Kwong and Wyatt.[177,181] This model introduces the concept of three functional faces of the protein: one that is immunologically active (neutralizing), one that is immunologically silent, and one that is only accessible in a dissociated form (non-neutralizing) due to interactions with gp41 (Figure 5.6B,C).[181] While it has since been shown that the exposed faces of gp120 are significantly dynamic in nature and so do not lend themselves to easily demarcated categorization, it is

beneficial to understand the functional principles of these faces, as they confer a basic framework for the three principle methods of gp120-based host-immune evasion.

5.3.2 Cloaking of Env

The 'silent' face of the protein actually constitutes a large portion of gp120, and is a direct result of heavy glycosylation, effectively shielding it from host immune responses. These sugars constitute approximately 50% of the molecular mass of Env (Figure 5.6),[182] and are of a heterogeneous nature. Oligomannose moieties are added to the precursor protein during translation in the endoplasmic reticulum, and are differentially modified in the Golgi, yielding a mixture of oligomannose and more complex N-glycan carbohydrates present on the surface of the mature protein.[183]

The development of viable, mature, properly folded Env protein requires unmodified oligomannose, but the presence of these moieties alone would normally elicit a strong endocytotic uptake and endolysosomal degratory response by dendritic cells.[184] In contrast, the presence of N-glycans on the surface is able to redirect the uptake of HIV by dendritic cells to an alternate pathway that transports HIV particles inside microvesicles, avoiding the degratory pathway, leading to eventual presentation of intact virions to CD4+ T-cells.[183,185] This process, based upon the DC-SIGN lectin, has been described as a novel method by which HIV is able to hijack the host immune system, as it facilitates the transport of HIV particles during initial infection from mucosal surfaces to secondary lymphoid tissue, where the particles are presented to CD4+ T-cells, the target cells for HIV infection.[186,187] As these interactions are not specific to a single glycan, but rather the relative concentrations of them, and the fact that these carbohydrates seem to exhibit a significant amount of clustering based upon hydrogen bonding of nearby moieties,[188] the virion is

able to retain significant flexibility in the external surface features of the glycosylated regions of the Env protein.

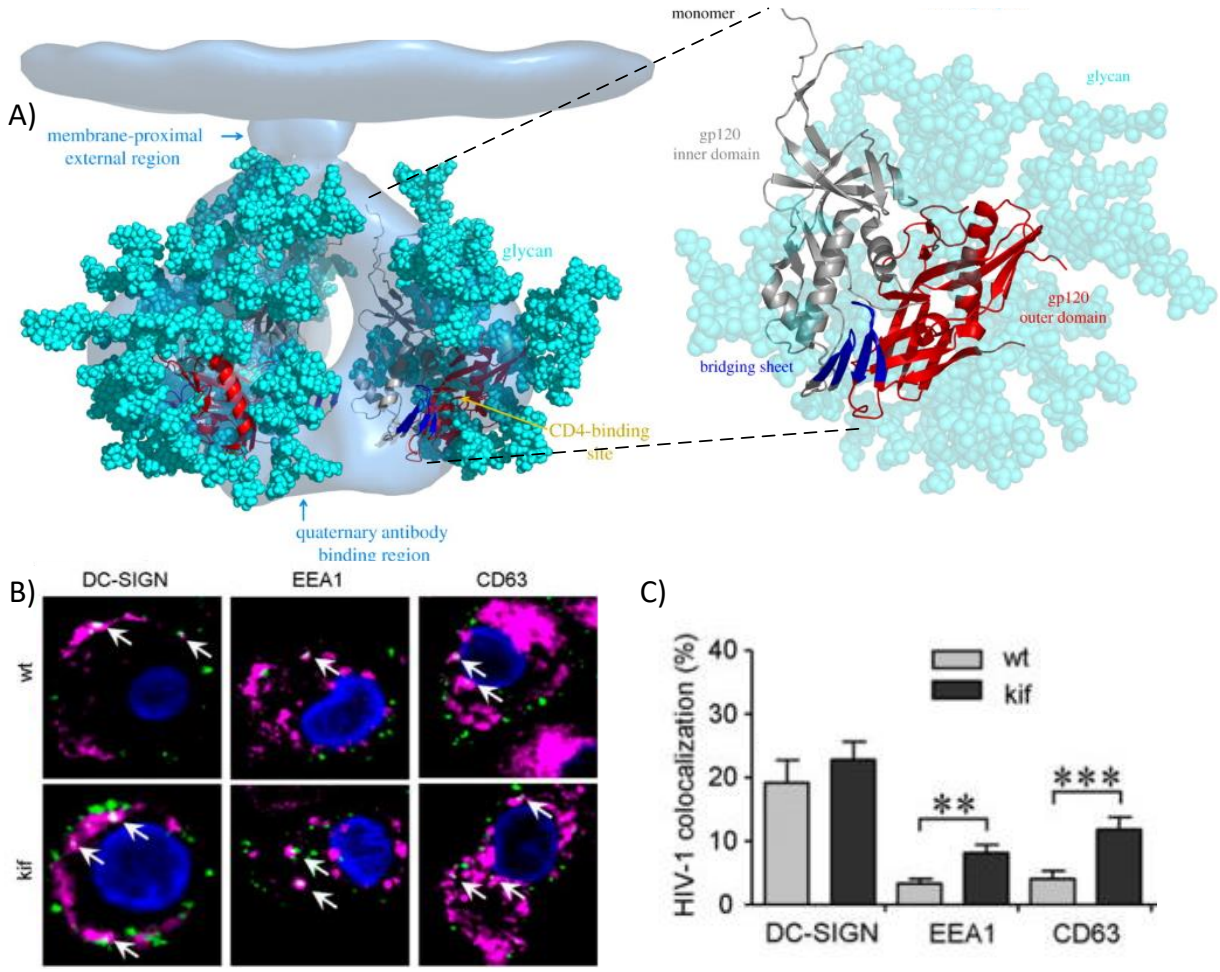

Figure 5.7. A) Glycan Shield of gp120. Density is shown in light blue for the cryoelectron microscopy tomogram of the HIV-1 spike.25 This has been fitted with the crystal structure of the HIV-1 gp120 envelope glycoprotein,[180] with N-linked glycosylation shown in cyan as space-filling spheres and polypeptide backbone displayed in ribbon representation and colored grey for inner domain, red for outer domain and blue for bridging sheet. Modelled N-linked glycan is displayed as light blue.[228] B, C) Oligomannose-enriched virus colocalizes more strongly with internal endocytic markers compared with wt virus. Dendritic cells were loaded with fluorescent GFP-labeled virus (green) in the absence (wt) or presence of kifunensine (kif) for 2 h. Nuclei (blue) and different marker proteins specific for cellular compartments of iDCs were stained (pink); colocalization (white) with fluorescent HIV-1 (green) is indicated by arrows. A relatively small amount of HIV was clustered with EEA1 (~3%) and CD63 (~4%), which mark early and late endosomes, respectively. Oligomannose-enriched virus colocalized more consistently with both EEA1 and CD63 (~8 and ~12%, respectively). The relatively low colocalization of both viruses with EEA1 and CD63 may be, in part, a consequence of fast transit through these compartments, but the colocalization of oligomannose-enriched virus with these markers was consistently higher.[185, Adapted]

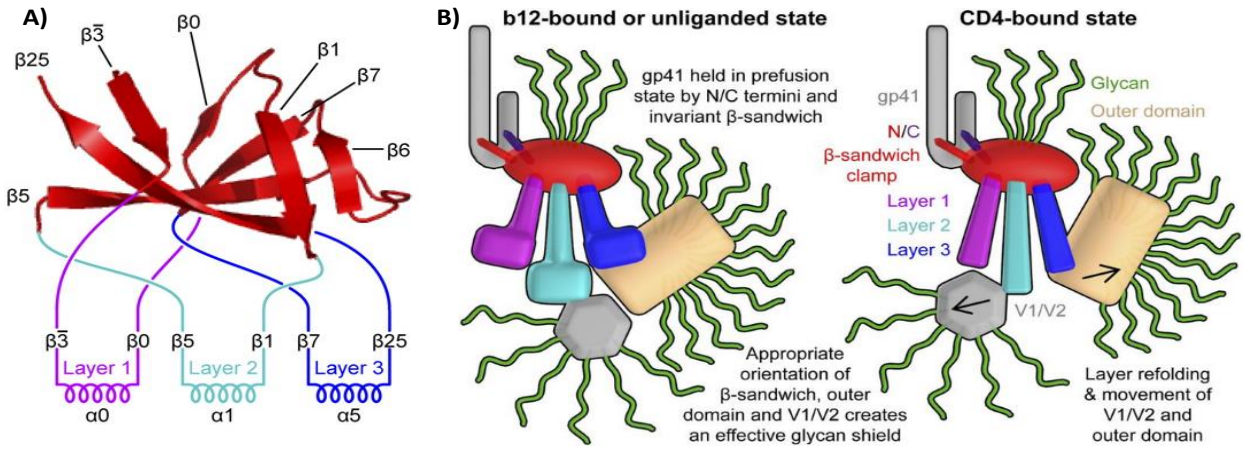

Figure 5.8. "Layered" gp120 architecture A) The newly defined 7-stranded β-sandwich is shown in ribbon diagram representation (red) with β-strands labeled and loop excursions to the layers depicted schematically with layer 1 in violet, layer 2 in cyan, layer 3 in blue, and the outer domain in light brown. B,C) β-Sandwich clamp and embracing N and C termini of gp120 are shown holding gp41 in a metastable state. The layers, meanwhile, can refold to position the relative orientations of three highly glycosylated components: β-sandwich, V1/V2 loops, and outer domain. In the unliganded state (B), the glycan-bearing elements arrange to form an effective "glycan shield" that prevents recognition by most antibodies. In the CD4-bound state (C), the layers organize with outer domain to form the high-affinity binding sites for CD4 and coreceptor.[170]

More than just providing a scaffold for a multifunctional glycan shied, the structure of gp120 itself also confers multiple methods of host immune response evasion. While even early structural analyses of gp120 recognized major conformational changes likely took place,[177] understanding the full picture of complex interactions that take place to move between the unliganded[189,190] and CD4-bound conformations has taken a substantial amount of effort.[176,177,191,192] Initial limitations in crystallization methods were surpassed, and as more complete Env isolates were successfully studied, less uncertainty about peripheral structures existed, particularly near the gp41 attachment point. The current model for gp120 relies on two domains: the inner and outer domains, referring to the location of the domains with respect to the central axis of the trimeric complex *in vivo.* The inner domain is composed of a beta-sheet 'clamp' sub-domain responsible for interfacing with gp41 and three layered structures emanating from the beta-sheet region as separate loops. These layers can effectively move past each other to rearrange the larger, glycosylated portions of gp120: the V1/V2 loop and the outer domain (Figure 5.8).[190,193-195]

Variable loops, V1 through V5, provide high levels of mutability, and exist on the external faces of gp120. V3 emanates from the distal, inner tip of the outer domain and is not glycosylated, and has been known to be a significant source of immunologic response since the early 1990s.[196] It has been shown to specifically direct the choice of secondary receptor toward either CCR5 or CXCR4, based upon the amino acids at the 11th and 25th positions.[197] The structure has been elucidated as a beta-hairpin tipped loop that extends independently from the gp120 body after CD4 binding, with highly conserved regions at its tip and base utilized for interaction with two separate domains of the coreceptor (Figure 5.9A).

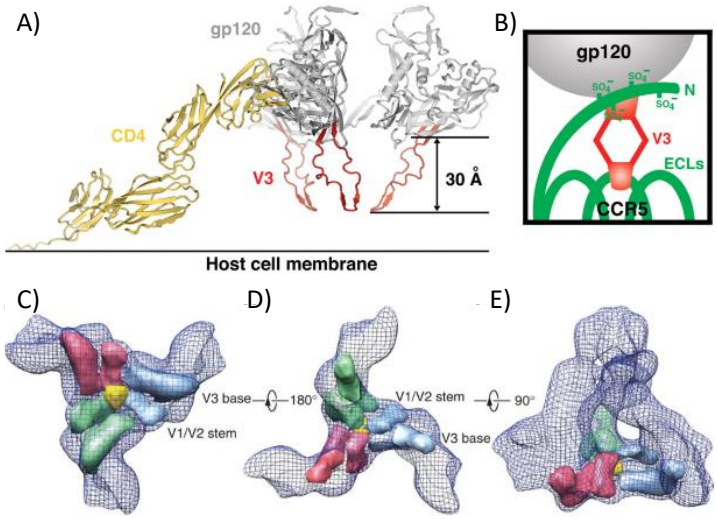

Figure 5.9. A) V3 in the context of a trimer at the target cell surface. The structure of the CD4-triggered gp120 with V3 was superimposed onto the structure of four-domain CD4 and the trimer model obtained by quantification of surface parameters. B) Schematic of coreceptor interaction. V3 (red) is shown with its conserved base interacting with the sulfated CCR5 (green) N terminus and its flexible legs allowing its conserved V3 tip to reach the second extracellular loop of CCR5.[193] C) The segmented local densities of gp120 that associate near the trimer axis are shown as solid surfaces wrapped in a meshwork representing the overall Env trimer, viewed from the perspective of the target cell, (D) as viewed from the perspective of the viral membrane and (E) as viewed from an angle parallel to the viral membrane. Three arms extend from the V3 base of each gp120 subunit toward the trimer axis and appear to support the central triangular junction. (c) The gp120 trimer-association domain segments are viewed from a perspective parallel to the viral membrane.[196]

Though it is not glycosylated, V3 participates in an important immuno-evasive structure: the unliganded trimeric structure of the gp120 glycoprotein.[194] Mao, *et al.* has shown that a highly structured union centered on the trimeric axis serves to stabilize the trimer as well as remove any access to either gp41 or the functionally active components of the inner domain. V3, along with the V1/V2 loop, engage in gp120-gp120 interactions to stabilize the unliganded state of Env.[195]

This stabilization is important as the CD4-bound conformation of Env is the thermodynamically favorable position.[190,198] While difficulties in determining complete structures for V1/V2 and V3 domains persist, there is reasonable consensus that these interactions are occurring at the distal apex of the protein spike.[194,195,199-201] Functionally, it has been determined that V1/V2 interaction with V3 likely occurs as a trimeric unit, where the V1/V2 domain of a single gp120 interacts with the V3 domain of an adjacent gp120 (Figure 5.9B).[200] Furthermore, the differences in the stability of this unliganded trimer likely has significant clinical implications, as any changes to these regions seem to directly affect infectivity. One interesting hypothesis is that the relative instability of the unliganded form[202] is an evolved instability not present in HIV-2, which might be a reason that infectivity of that subtype is significantly lower than the more highly-CD4-dependent HIV-1.[203] Mutagenic modulation of the strength of these interactions is an important consideration for neutralization targets, as modification of these exposed domains, particularly V3, could potentially stabilize the unliganded trimer, thereby decreasing infectivity.[190,204]

5.3.3 Viral Attachment and Entry

As the primary effector of HIV entry, CD4 binding is likely the most thoroughly studied step in the HIV infection pathway. As could be expected, the amino acids directly involved with the binding pocket are some of the most conserved, located in C1, C3, and C4 domains.[205] Within the layered structure discussed previously, the CD4 binding region is located in-between layers 2 and 3 of the inner domain and the outer domain. A conformational change in the 3rd layer of the inner domain serves as a wedge causing a rotation and displacement of the outer domain of gp120.[206] The overall movement can be described as a rotation combined with a 'blossoming' or outward separation of the three gp120 units (Figure 5.10).[191,207] This movement is responsible for many of the conformational changes in gp120 subunits: the rotation is responsible for the

uncovering of the V3 domain by an adjacent V1/V2 domain,[200] while the hinged opening has been shown to be an important step in decreasing the distance between virion and host cell membranes via lateral deformation of CD4 proteins (Figure 5.10f).[191] Together, these interactions serve to prepare the coreceptor binding site by forming the bridging sheet area,[181,208] as well as repositioning the V3 loop[192] so that it is oriented directly away from the virion particle.

HIV gp41 is the smaller of the two Env proteins, and has three functional units: the previously discussed CD participates in intracellular localization and endocytosis, the membrane spanning domain (MSD) serves to anchor the Env protein in the lipid envelope, and the extracellular domain (ECD), is responsible for interactions with host cells. The MSD is composed of 25 highly conserved amino acids that anchor the protein into the viral membrane with a single alpha-helical domain. Mutations in this sequence have been shown to modulate viral fusion efficiency, but specific mechanisms remain unconfirmed.[174,209]

While the first two domains remain relatively structurally stable, the third domain undergoes multiple, complex, conformational changes throughout the attachment and entry processes. This third domain has been recognized as being crucial to understanding the mechanism of entry for HIV, but until recently, only basic primary and secondary structural information was known.[209] In 2014, x-ray crystallography was able to elucidate the dynamic structure (Figure 5.11A).[178] While the gp120 beta-sandwich structure and N- and C- terminal domains of the gp120 inner domain have been implicated in gp120-gp41 attachment, Pancera, et al. was able to observe the structured four-helix collar present in the ECD that maintains the stable confirmation of these two gp120 tails (Figure 5.11B).[178,193] In agreement with several previous studies,[201,210,211] the prefusion state of gp41 is shown to contain two main precursor helices to the N- and C-terminal heptad repeats (NHR and CHR, respectively) along with unstructured loops. Across several

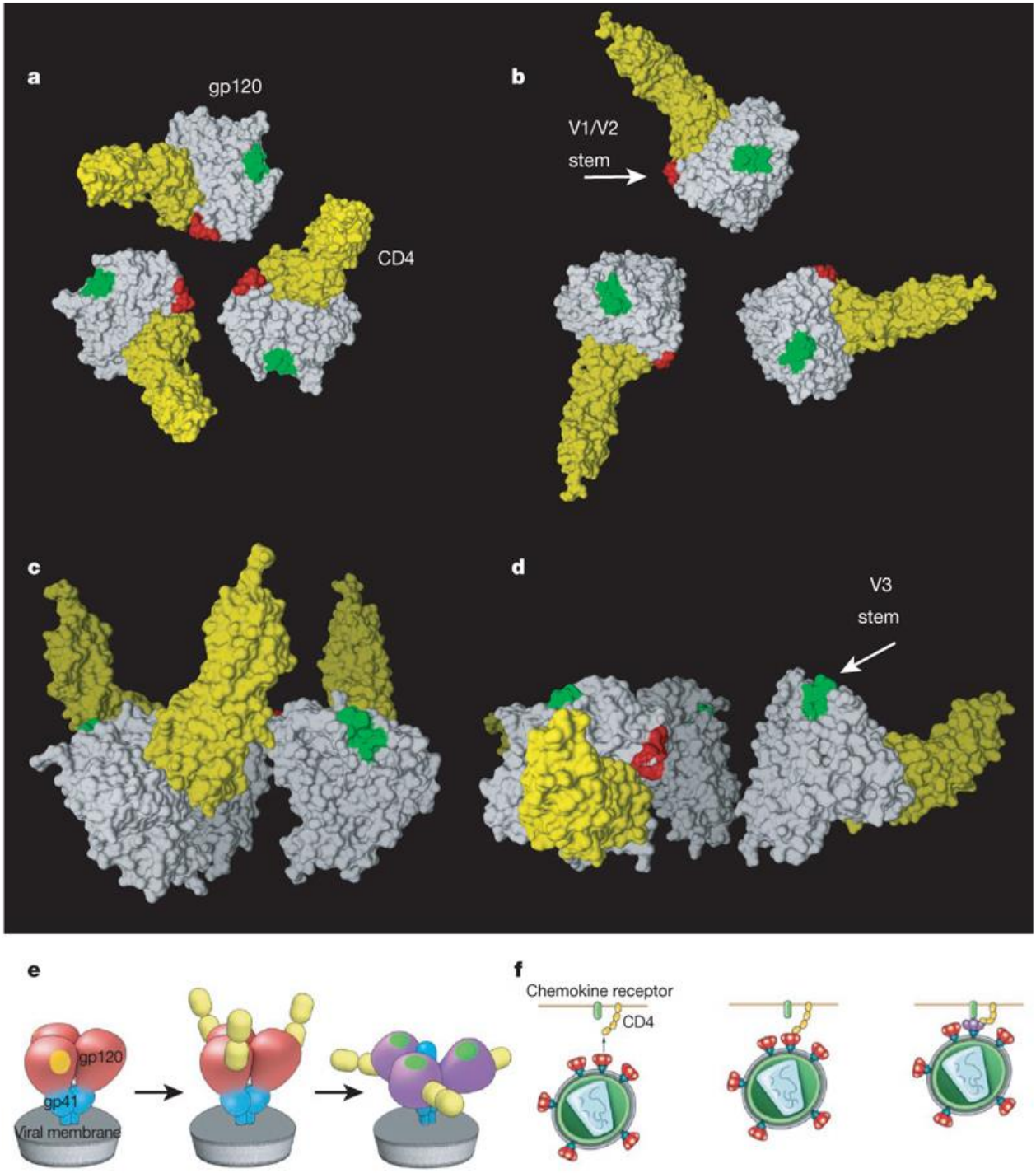

Figure 5.10. Model for the conformational change from the unliganded (a, c) to the CD4-bound state (b, d) shown as top (a, b) and front (c, d) views. The gp120 core, CD4, V1/V2 and V3 stems are shown in white, yellow, red and green colors, respectively. e, Schematic description of the gp41 (blue) and gp120 (red/purple) regions of the trimeric spike and the conformational changes that occur upon CD4 binding. The yellow patch near the apex marks the location of the CD4 binding site in the unliganded spike and the green patch at the apex marks the location of the V3 loop region in the spike after CD4 binding. f, Schematic view of the consequence of the CD4-induced conformational changes for viral attachment to the target cell and interaction with chemokine receptors (green at top). Colors in (f) have same meaning as in (e). [192]

piecewise crystal structures comprising intermediate states between pre- and post-fusion states, the precursor helices were shown to rapidly form two, long alpha-helices upon release of the four-helix 'latch' that place the fusion peptide (FP) in close proximity with the target cell membrane where it can enact its membrane-destabilizing mechanism.[178] The structure of this post fusion state is that of a coiled-coil, a common motif for Class 1 fusion proteins.

Upon establishment of the post fusion state, the projected FP domain, which is basic and strongly hydrophobic, interacts directly with the plasma membrane of the host cell, as a member of the Class 1 fusion proteins that includes other viruses such as coronavirus, influenza virus and ebolavirus.[178,212,213] Upon integration into the membrane, NHR and CHR regions attempt to assume a characteristic six-helix bundled formation. It has been demonstrated that either one or two of the CHR moving to the grooves of the NHR trimer is sufficient for membrane hemi fusion, and that the purpose of the final six-mer bundle is stabilization of the pore (Figure 5.12).[214,215] The details of actual lipid rearrangement during pore formation and viral membrane fusion are still unclear. Demonstration of comparatively high concentrations of phosphoinositides provides one potential mechanism for mediating instability in close-proximity lipid bilayers.[216] These membrane structures, much like cholesterol, maintain membrane fluidity, and allow for point-like protrusions to form.[217]

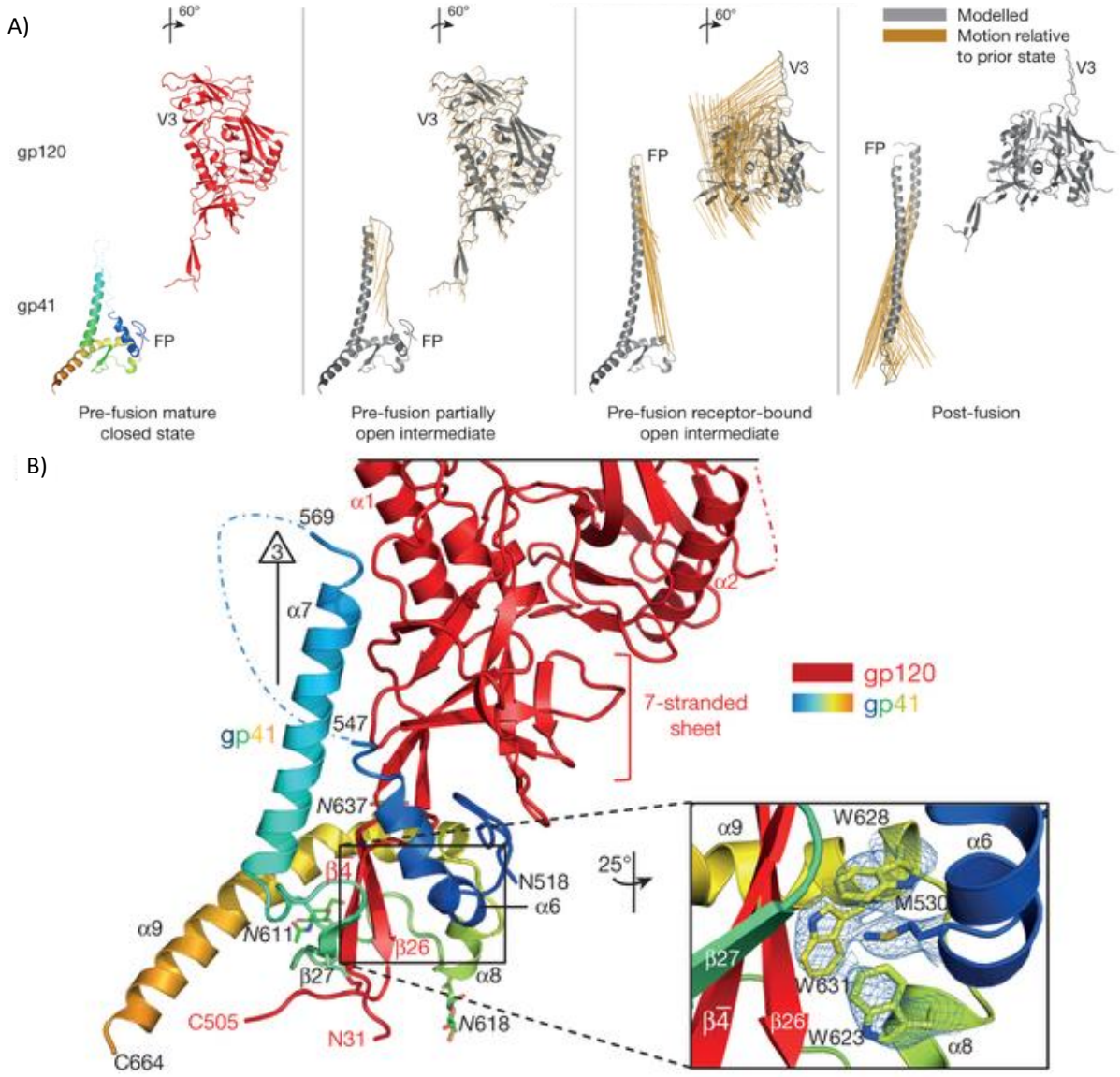

Figure 5.11. A) HIV-1 Env entry rearrangements with gp120 (top) and gp41 (bottom) rearrangements between each conformational state highlighted with orange lines depicting movement of each Cα between conformations. Subunit models are shown in grey. The spring-like release of the NHR and CHR can be readily observed. B) gp41 forms a four-helix collar, which wraps around extended N and C termini of gp120. Both gp120 (red) and gp41 (rainbow from blue to orange) are depicted in ribbon representation. The location of the trimer axis is indicated with a '3' inside a triangle. The viral membrane is at the bottom of the image. Zoom insert: the gp41 collar is clasped by the insertion of Met 530gp41 into a tryptophan sandwich and by the alignment of helices α6 and α8. 2Fo − Fc electron density for clasp residues is depicted at 1σ.[180]

5.3.4 Discussion

As with any field of cutting-edge science, there are current debates on particular components of the Env structure as described here. Of particular note at this time is the dialogue between the Cryo-EM and X-ray Crystallography methods, particularly the Sodroski and Subramaniam labs, in respect to the unliganded form of gp41. Since 2013 when a 6.5 Å Cryo-EM structure was published containing an unliganded gp41 form with disorganized pre-NHR/CHR precursor helices located in its core,[195,199] a discussion of the efficacy of the method has unfolded.[199,218-220] Conflicting results have been presented, suggesting a more ordered pre-NHR/CHR organization, which have also been supported by separate Cryo-EM studies.[201,210,211] Recent consensus appears to support the latter,[178,221,222] and so the gp41 structure discussed here is of that variety. It is worth noting that the discussion is ongoing, with recent discussion of the usage of disulfide-bond modification to assist with structural analysis, and its potentially contaminating effect on the determined ordered structures.[223] Regardless, the fact that gp41 undergoes some sort of conformational change from a more compact structure to the classically appreciated NHR/CHR coiled-coil protrusion post-CD4-binding is readily apparent from either school of thought.

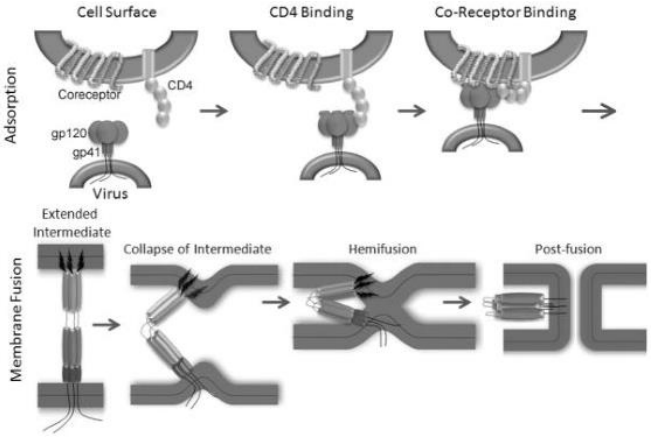

Figure 5.12. Top panel: The envelope protein is a trimer of heterodimers on the virus surface made up of the transmembrane subunit, gp41, embedded in the viral membrane and the globular surface subunit, gp120, non-covalently associated to gp41. Association between gp120 and CD4 causes conformational changes in gp120 that lead to binding to coreceptor. Bottom panel: Coreceptor binding triggers further concerted conformational changes, including formation of agp41 extended intermediate, that allow gp41 to initiate mixing of the outer bilayer leaflet resulting in formation of the hemifusion state. Finally, the inner leaflets mix resulting in membrane pore formation and injection of the virus core which is concomitant with gp41 six-helix bundle formation.[211]

While many structural investigations have been completed of various portions of the Env spike, there is much still to learn about the dynamics. While beginning and end-point analyses of structures (i.e. unliganded and CD4-bound) can provide a general picture of the complex conformational challenges, understanding the time-resolved path from conformation A to conformation B is a complex issue that necessitates the use of new tools. One such recent development is the use of Forster resonant energy transfer (FRET) with single-molecule resolution to look at the inter-protein distances in real time. Researchers at Yale and Cornell recently demonstrated the transient shifting of Env conformations for the unbound state to the canonically-described CD4-bound state and back, suggesting the binding action-conformational change relationship may not necessarily be as causal as has been assumed thus far.[202]

The fact that the Env spike is still an area for such intense scrutiny only serves to emphasize both its complexity and importance. As the sole non-host protein exposed on the HIV virion surface, Env serves as the sole target for any traditional antibody-based vaccine or therapy. As the underlying mechanism of Env variation and conformational progression during membrane fusion events unfolds, the quest for neutralizing antibodies and vaccine candidates is proceeding in tandem, benefiting from each new piece of the puzzle.[224,225] The past 30 years have seen a remarkable increase in awareness, funding, and international cooperation that have spurred much of the work discussed. With an ambitious goal of 90-90-90 by 2020 and 95-95-95 by 2030 (95% of infected people who know their status, 95% of people who know their status being placed on antiretroviral therapy (ART), and 95% of those on ART maintaining suppressed viral load)[226] progress will likely even accelerate.

5.3.5 Implications for Direct HIV Detection

For the successful direct detection of whole HIV virions, the options for serological detection are limited. The few consensus regions discussed here provide strong indicators of where future monoclonal antibody development might have success. Significant work is ongoing in the field of serological recognition of HIV virions due to the extensive research being done into vaccine development. The best chances at high-yield capture of the dilute concentrations required for viable viral load measurement rely on broadly neutralizing antibodies bnAbs. For the development of the digital detection platform, I believe the use of a similarly polyclonal antibody is well-suited for our applications and current project progress. As research within the realm of bnAbs continues in parallel with our development of the optical and microfluidic platforms, it is advisable to continue monitoring literature for consensus on which bnAbs might be 1) most stable 2) reasonable to acquire, and 3) most likely to operate on compatible sites for sandwich-based capture.

5.4 Single Virus Detection of HIV

Based upon previous whole-virion detection in a static setting,[82] we selected a high-selectivity, high-affinity surface functionalization for our polyclonal antibody immobilization. After cleaning the gridded PC surface discussed in 5.3, overnight chemical vapor deposition (CVD) of (3-Mercaptopropyl) trimethoxysilane (3MPTS) results in a SAM of sulfhydryl groups. To minimize linear distance between detectable nanoparticles and the PC sensor, a maleimide-activated Neutravidin was used in combination with a biotinylated anti-gp120 antibody (Abcam). Nanoparticles were attached to anti-gp120 via the same SH-PEG chemistry used in Section 5.1. The overall detection scheme can be seen in Figure 5.13.

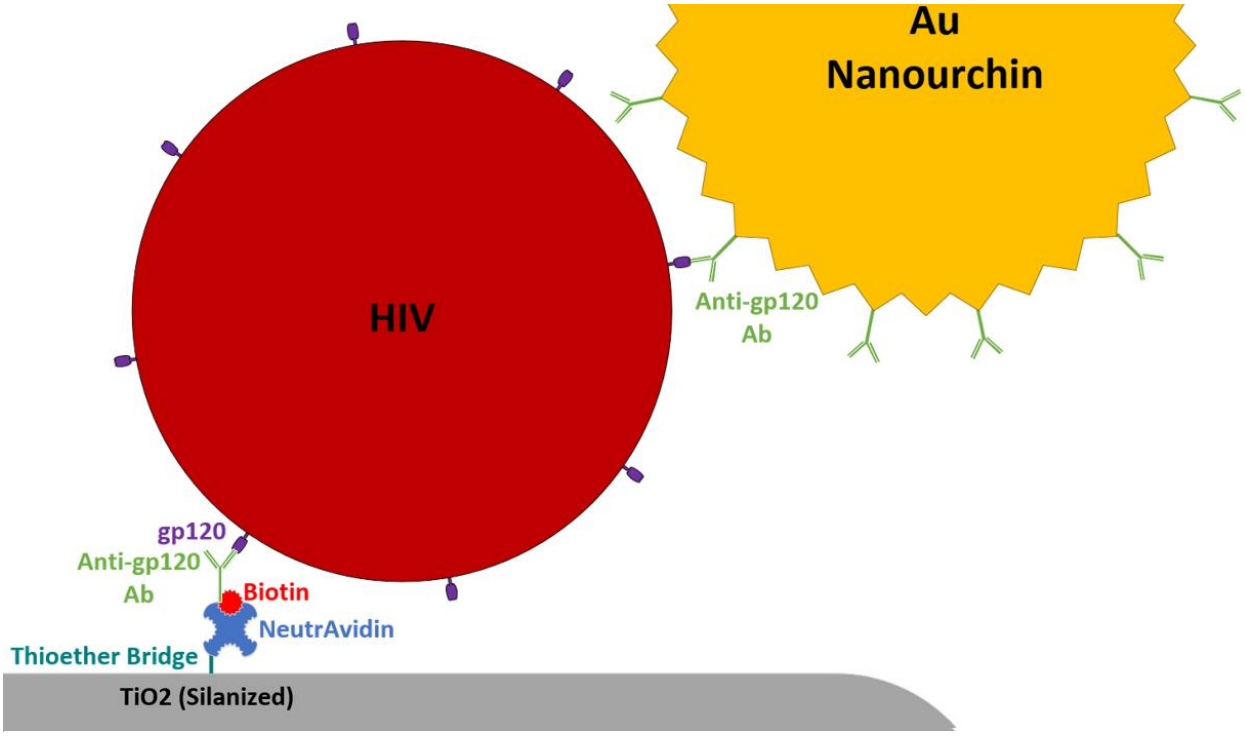

Figure 5.13. Schematic of HIV Direct Detection. 3-MTS serves to thiolate the surface of the PC sensor, which forms high-affinity bonds with the maleimide-activated Neutravidin. A biotinylated anti-gp120 antibody serves as the final functional layer. All components are drawn approximately to scale.

As can be seen in Figure 5.14, we were able to observe both HIV and nanoparticles on the sensor surface. HIV itself does not appear to generate a measurable signal via either PIV or PWV images from the PCEM; however, the nanoparticles generate a clearly-visible signal. By using the previously described grid, corresponding areas of the PC sensor were imaged by both PCEM and

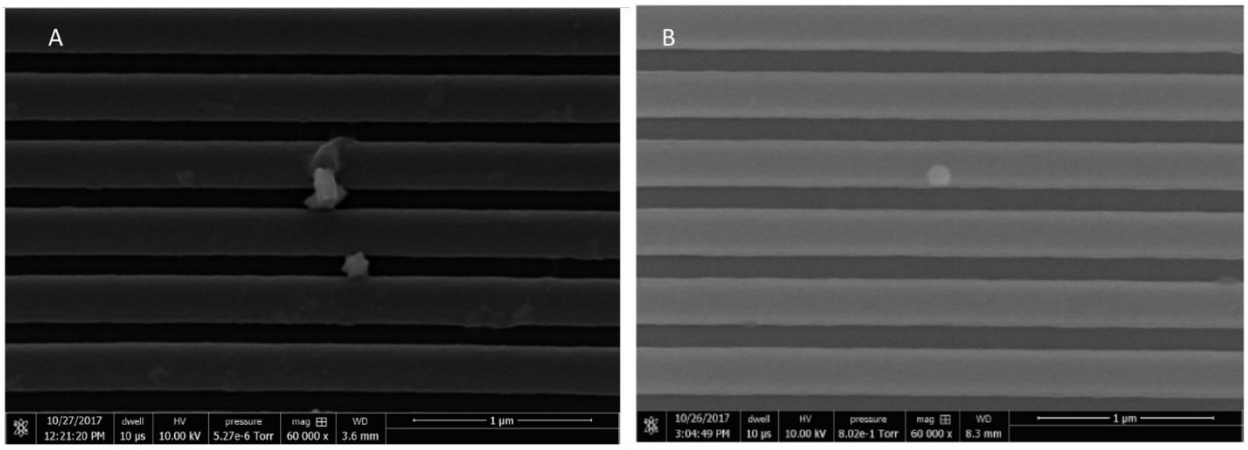

Figure 5.14. A. SEM image of magnetic nanoparticles, comprised of gold core and nickel decorations. B. SEM of HIV virion**.**

SEM, and SEM images were analyzed for potential HIV virion-nanoparticle complexes. One such complex can be seen in Figure 5.15.

Having located a complex of interest in a gridded section that had been scanned via PCEM, spatial locations were aligned (as described in Section 5.2) and an overlay was used to identify the respective location in the PCEM scan. In panel A, the grid pattern can be observed across the top and right side of the full PIV image. B shows a composite image resulting from the overlay of SEM and PCEM images, and shows clear PIV shifts for many of the nanoparticles observable in the SEM image. Panel D has a series of bright yellow regions in a line, indicating substantial decreases in PIV. These are resultant from a series of deformations in the periodic structure of the grating, and they help to orient the reader to the alignment between the images. In panel E, representative spectra from within the region of interest and just outside are shown, demonstrating a clear decrease in PIV, and a slight positive shift in PWV, as expected. A close-up view of the HIV-nanoparticle complex is shown in panel F.

5.4.1 Improvements for Collection Efficiency

As discussed in previously in this Chapter, one of the most substantial challenges in developing a viable POCT assay for HIV viral load is balancing the time-dependence of the diffusion of virions to the sensor surface with a reasonable measurement duration for the POC testing paradigm. A principal way in which we can overcome this time constraint is by mixing the HIV sample with functionalized antibodies prior to introduction to the PC sensor. This allows for the HIV-NP binding event to take place in 3D space, leaving a single 1D diffusion step (as opposed to the two serial 1D diffusion steps required if HIV sample and NP solution are flowed over the sensor in order.

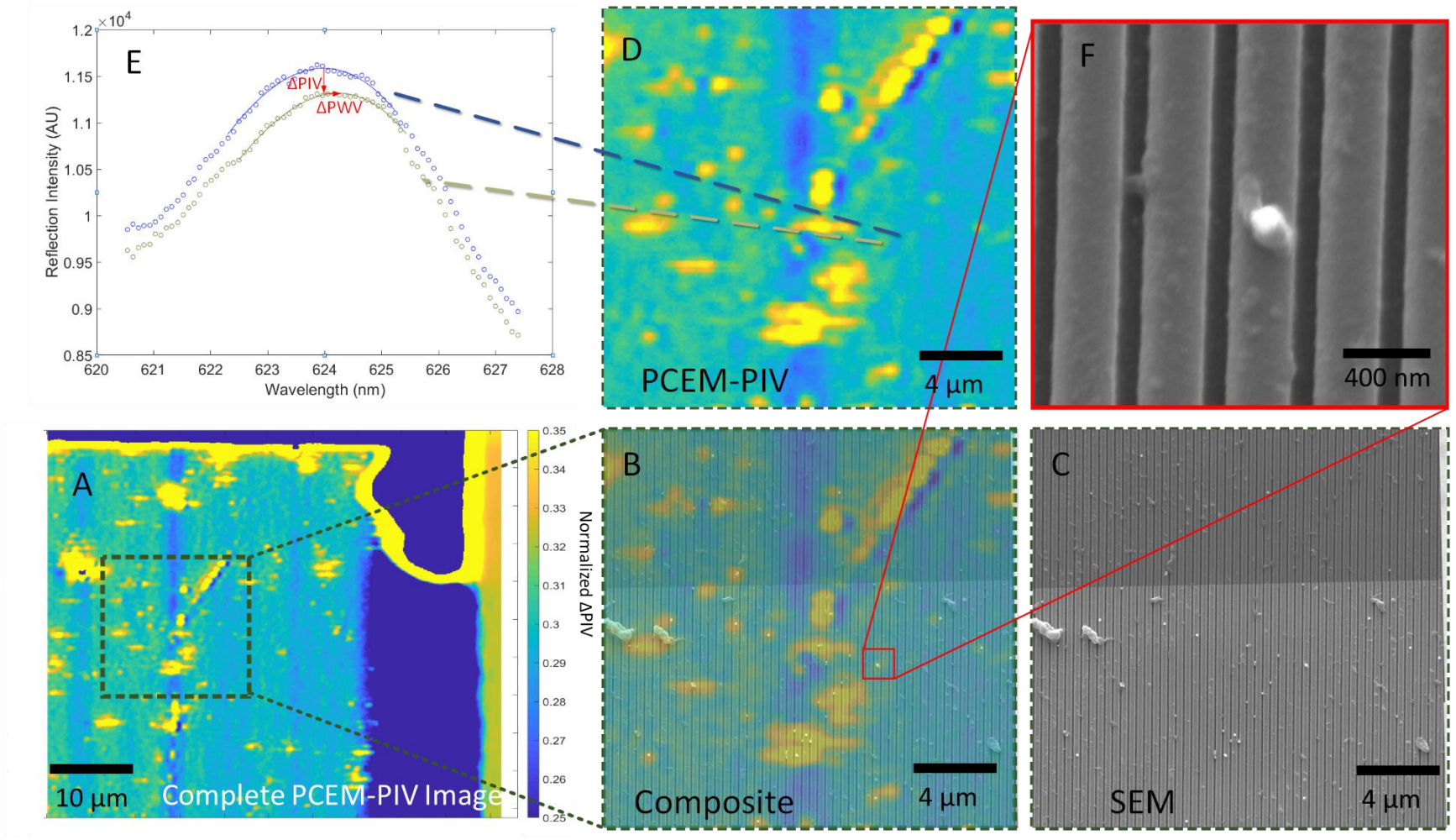

Figure 5.15. Validation of PC-captured HIV-Nanoparticle Complex. A. C., Normalized PIV images from PCEM showing the location of many nanoparticles, and a single HIV-nanoparticle complex. B. Composite image of C & D with 50% transparency to observe colocalization of PIV features and observed SEM nanoparticles. The red box shows the location of the detected HIV-nanoparticle complex. F. Peaks of representative pixels from inside and outside the complex area showing shifts in PWV and PIV. Solid lines represent cubic curvefit used to calculate PIV and PWV.

To that end, we can further accelerate the process by incorporating a complimentary technology being developed by our collaborators in the Singamaneni lab at Washington University in St. Louis. By decorating octahedral gold nanoparticle cores with nickel, resonant-wavelength-tuned particles can be created that also exhibit ferromagnetic properties. Thus, by performing incubation of a mixed HIV-sample/conjugated NP solution on a PC sensor with a bar magnet located underneath (visible in Figure 5.16C), the magnetic field can bias diffusion toward the sensor for the rate-limiting 1D diffusion step.

5.4.2 Microfluidic Design

While COMSOL simulations were crucial for developing an intuition for how channel dimensions affect the flow rate and size/shape of the depletion region over the PC sensor, practical experimentation was an important component of designing our prototype microfluidic device. Knowing we wanted to rely on a passive "pump" to drive the microfluidic flow, it was necessary to run a series of experiments on types, thicknesses, sizes and shapes of filter paper pads. The two criteria used to assess the filter paper capillary pumps were capacity (it must hold 200 µL of liquid)

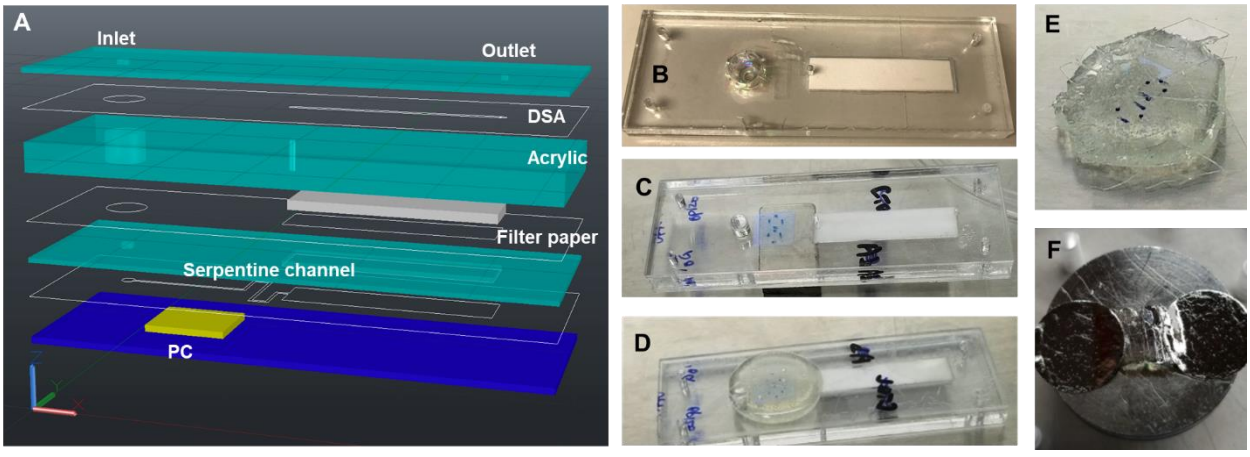

Figure 5.16. Design of the Microfluidic Chip. A. Alternating layers of laser-cut acrylic sheet and double-sided adhesive provide the structure of the chip which contains a detection chamber, where the PC is located, a serpentine channel to provide some flow resistance, and a multi-layer sandwich of filter paper to provide our passive capillary action pump. B. One of the microfluidic chips used to experimentally determine filter paper pump dimensions to pump 200 µL in 30 minutes. C. PC sensor incubating on top of a magnet. D. Epoxy used to remove PC sensor from microfluidic device. E. Removed PC sensor. F. PC sensor prepped for SEM showing clear fragmentation of the sensor surface from the removal process.

and flow rate (it should take between 30 and 45 minutes for a 200 µL of liquid to flow through the sensing region. The resultant sensor design is based on a multi-layer lamination of layers comprised of acrylic sheet, double-sided adhesive (DSA), and filter paper (Figure 5.16A). An inlet chamber (capable of holding up to 100 µL of liquid) is connected to the PC sensing region by a 1-mm-wide channel which continues on the other side of the PC sensing area. Next, the liquid is introduced to a short serpentine channel, followed by its exit onto the laminated filer paper.

Two full microfluidic experiments have been completed thus far, though SEM validation with the microfluidic platform is more challenging. As the PCs are fabricated on cover glass, detaching them from the DSA interface with the microfluidic chip resulted in the first several sensors shattering. A new method of curing quick-set epoxy on the underside of the PC has been developed to allow for removing the PC from the chip. Even with this method, which does largely preserve the glass cover slip, albeit in many smaller pieces, the UVCP appears to be bound to the PC itself less strongly than the DSA applied during microfluidic chip fabrication. A second epoxy-curing on the underside of the thin UVCP/PC film has allowed for SEM mounting and imaging. Due to the significant increase in difficulty of obtaining SEM images, validation of the microfluidic improvements to the binding dynamics of the device are likely best completed by scanning multiple areas of the PC for known (and verified) concentrations of virus.

5.5 Toward a Point-of-Care PCEM Instrument

From the work thus far, direct detection of HIV via PCEM continues to demonstrate significant promise. But that's not to say that issues haven't arisen along the way. A few of these I would like to elaborate on possible ways to address them, in particular, as we design a portable PCEM instrument to build upon the work completed thus far.

As soon as we completed our first SEM validation of nanoparticles detected via PCEM, I first noticed a pattern among nanoparticles that provided sharp, clear PIV responses and those that provided essentially none. In Figure 5.3, there are approximately 10 nanoparticles that do not elicit a localized decrease in PIV. At the time, I recognized that all of these ten nanoparticles appeared on the "top" surfaces of the PC device. In going back and looking more closely, in addition to all "undetected" nanoparticles appearing on the PC plateaus, *all* of the tens of *detected* nanoparticles exist in or adjacent to the troughs in between. This is not the first time we've thought about location-specific implications for nanoparticles. In our 2014 paper first describing single nanoparticle detection on the PCEM, simulations were run for both dielectric and metallic particles of TiO_2 and Au, respectively. In figure 2, 100nm nanoparticles (the precise size used in this work) are modeled to show FDTD E-field distribution. It looks as if there is about a 50% theoretical loss of PIV shift between the two modeled locations. While that doesn't completely explain the absence of particles, it does suggest that further investigation of how the PC structure responds to attachment events at different locations in its period. In addition to landing on different parts of the surface, the direct HIV detection discussed in this work relies on two binding events, which further increases the locational variation of nanoparticles that we would hope to register on our point-of-care device.

Another concern is most certainly the extent to which losses of capture efficiency compound upon each other. With very low numbers of analyte that we are hoping to enumerate, each "missed' particle has substantial consequences. With both known losses (inability to have 100% of the sample have enough residence time to bind to the sensor surface), and unknown losses (Env viral shedding? Conformational changes?) there remains significant amounts of risk for the limits of detection that may be possible. Something worth investigating further might be the

possibility of using a viral protein target with more copies per virion. Copies of both p17 (matrix protein) and p24 (capsid protein) are in the hundreds/virion range, which would increase the number of potential analytes in a patient sample from the 1-10 range to the 1000-10,000 rage, which in turn, would result in a more robust device capable of tolerating more errors as a result of "lossy" biology.

Finally, as for the actual design and construction of the portable PCEM instrument, I firmly believe in minimizing moving parts, and the value of rapid-prototyping. The rate at which the development of the first-generation smartphone spectrometer (machined aluminum) and second-generation (3D printed in-house) could take place were so incredibly different. The ability to affordably and quickly test out components, or even build custom optical mounts, made a world of difference. Furthermore, the collective body of experience in lab presents a natural advantage to working with other prototyping systems. The work thus far on the POC PCEM platform for viral load monitoring has been incredibly promising, and I look forward to continuing to work with my colleagues to see it become a reality.

CHAPTER 6: CONCLUSIONS

In the first half of this dissertation, I have presented the evolution of smartphone-based spectroscopic biosensing. The work in Chapter 2, when published, represented the first demonstration of a smartphone camera for spectrometric measurement of biological samples, and set off a significant amount of interest in the area both within the academic community and the public. From that initial demonstration, we have traced the development of a smartphone-based spectrometer into a truly handheld, 3D printed prototype capable of performing the most common spectroscopic assays commercially available with comparable limits of detection. While there are still a few interesting research questions remaining related to the developed TRI-Analyzer, including the possibility of performing scattering-based measurements, I am excited for the project to graduate to the realm of commercialization.

In the second half of this work, I presented the evolution of Photonic Crystal Enhanced Microscopy from a micro-scale attachment sensing platform to a nano-scale binding-event detector. The work in Chapter 4 touches on just a few of the myriad of cellular-based assays that could be investigated, with particular future potential in the areas of stem-cell differentiation, drug screening, and even personalized medicine. For the point-of-care, though the PCEM platform hold enormous promise as a mechanistically-simple, spatially-resolved platform capable of discerning individual binding events. The discussed benefits for diagnostics for infectious pathogens, including HIV viral load, make the PCEM ideally suited for further development in situations with extremely low numbers of expected analyte. In Chapter 5, I present the body of work that has already been put forward toward the goal of a portable PCEM instrument developed specifically to perform point-of-care viral load monitoring.

From my exposures to the many parts of the diagnostic design process, from the generation of new ideas through the selection and performance of proof-of-use assays, I have been able to observe the development of the field of smartphone biosensing as a whole. The number of researchers has increased dramatically in this area, and I believe will continue to expand, which in turn, will push smartphone based biosensing toward the frontiers of research, where perhaps they will continue to provide interesting diagnostic platforms to users and researchers alike as the lines between laboratories and our everyday environments continue to blur.

REFERENCES

Portions of this Dissertation include material previously published under a variety of copyright agreements, including:

Portions of Chapter 2, including Subsections 2.1.1, 2.1.2, and Section 2.3, as well as Figures 2.3 and 2.11 are adapted and reproduced from Ref. 16 with permission from the Royal Society of Chemistry.

Section 2.2, including Figures 2.4-2.9, is adapted and reproduced from Ref. 10 with permission from the Optical Society of America.

Much of Chapter 3, including Figures 3.1 – 3.9 is adapted and reproduced from Ref. 87 with permission from the Royal Society of Chemistry.

Some material in Sections 3.2 and 3.4 was first published with IEEE, as indicated by references at the end of those paragraphs. Reference #95, Long, K. D., Woodburn, E. V. & Cunningham, B. T. in IEEE-NIH 2017 Special Topics Conference on Healthcare Innovations and Point-of-Care Technologies (IEEE EMB, NIH Natcher Conference Center, Bethesda, MD, November 6-8 2017).

Sections 4.3-4.7, including Figures 4.2-4.5, is adapted and reproduced from Ref. 114 with permission from the Royal Society of Chemistry.

1 Sullivan, F. Global Battery Market for Wearables. (Frost & Sullivan, 2016).
2 Soper, S. A. *et al.* Point-of-care biosensor systems for cancer diagnostics/prognostics. *Biosens Bioelectron* **21**, 1932-1942, doi:10.1016/j.bios.2006.01.006 (2006).
3 Kirkwood, J. The Next Step for Molecular Point-of-Care Testing - AACC.org. *Clinical Laboratory News* (2016). <https://www.aacc.org/publications/cln/articles/2016/june/the-next-step-for-molecular-point-of-care-testing>.
4 Bissonnette, L., Département microbiologie-infectiologie et immunologie, F. d. m., Université Laval, Centre de recherche en infectiologie de l'Université Laval, C. d. r. d. C., Québec, Canada, Bergeron, M. G. & Département microbiologie-infectiologie et immunologie, F. d. m., Université Laval. Diagnosing infections—current and anticipated technologies for point-of-care diagnostics and home-based testing. *Clinical Microbiology and Infection* **16**, 1044-1053, doi:10.1111/j.1469-0691.2010.03282.x (2016).
5 Chin, C. D., Linder, V. & Sia, S. K. Commercialization of microfluidic point-of-care diagnostic devices. doi:10.1039/C2LC21204H (2012).
6 McLeod, E. & Ozcan, A. Unconventional methods of imaging: computational microscopy and compact implementations. *Rep Prog Phys* **79**, 076001, doi:10.1088/0034-4885/79/7/076001 (2016).
7 Lee, S. A. & Yang, C. A smartphone-based chip-scale microscope using ambient illumination. doi:10.1039/C4LC00523F (2014).
8 Yu, H., Tan, Y. & Cunningham, B. T. Smartphone Fluorescence Spectroscopy. doi:10.1021/ac502080t (2014).
9 Hossain, M. A. *et al.* Combined "dual" absorption and fluorescence smartphone spectrometers. *Optics Letters, Vol. 40, Issue 8, pp. 1737-1740,* doi:doi:10.1364/OL.40.001737 (2015).
10 Long, K. D., Yu, H. & Cunningham, B. T. Smartphone instrument for portable enzyme- linked immunosorbent assays. *Biomedical Optics Express, Vol. 5, Issue 11, pp. 3792-3806,* doi:doi:10.1364/BOE.5.003792 (2014).
11 Jiang, L. *et al.* Solar thermal polymerase chain reaction for smartphone-assisted molecular diagnostics. *Scientific Reports, Published online: 20 February 2014; | doi:10.1038/srep04137,* doi:doi:10.1038/srep04137 (2014).
12 Mudanyali, O. *et al.* Integrated rapid-diagnostic-test reader platform on a cellphone. doi:10.1039/C2LC40235A (2012).
13 St John, A. & Price, C. P. in *Clin Biochem Rev* Vol. 35 155-167 (2014).
14 Kwon, L., Long, K. D., Wan, Y., Yu, H. & Cunningham, B. T. Medical diagnostics with mobile devices: Comparison of intrinsic and extrinsic sensing. *Biotechnology Advances* **34**, 291–304, doi:10.1016/j.biotechadv.2016.02.010 (2016).
15 Zhang, D. & Liu, Q. Biosensors and bioelectronics on smartphone for portable biochemical detection. *Biosens Bioelectron* **75**, 273-284, doi:10.1016/j.bios.2015.08.037 (2016).
16 Gallegos, D. *et al.* Label-free biodetection using a smartphone. *Lab on a Chip* **13**, 2124-2132, doi:10.1039/C3LC40991K (2013).
17 Lequin, R. M. Enzyme immunoassay (EIA)/enzyme-linked immunosorbent assay (ELISA). *Clinical Chemistry* **51**, 2415-2418 (2005).
18 Kai, J. *et al.* A novel microfluidic microplate as the next generation assay platform for enzyme linked immunoassays (ELISA). *Lab on a Chip* **12**, 4257-4262, doi:10.1039/C2LC40585G (2012).
19 Poulsen, F. & Jensen, K. B. A luminescent oxygen channeling immunoassay for the determination of insulin in human plasma. *J Biomol Screen* **12**, 240-247, doi:10.1177/1087057106297566 (2007).
20 Cauchon, E. *et al.* Development of a homogeneous immunoassay for the detection of angiotensin I in plasma using AlphaLISA acceptor beads technology. *Anal Biochem* **388**, 134-139, doi:10.1016/j.ab.2009.02.031 (2009).
21 Brown, J. *et al.* A hand-powered, portable, low-cost centrifuge for diagnosing anemia in low-resource settings. *Am J Trop Med Hyg* **85**, 327-332, doi:10.4269/ajtmh.2011.10-0399 (2011).

22 Wong, A. P., Gupta, M., Shevkoplyas, S. S. & Whitesides, G. M. Egg beater as centrifuge: isolating human blood plasma from whole blood in resource-poor settings. *Lab on a Chip* **8**, 2032-2037, doi:10.1039/B809830C (2008).
23 Mach, A. J., Kim, J. H., Arshi, A., Hur, S. C. & Di Carlo, D. Automated cellular sample preparation using a Centrifuge-on-a-Chip. *Lab on a Chip* **11**, 2827-2834, doi:10.1039/C1LC20330D (2011).
24 Pham, N. M. *Blood filtration for multiplexed point-of-care diagnostic devices*, University of Toronto, (2012).
25 Peter, J. G., Theron, G. & Dheda, K. Can Point-of-Care Urine LAM Strip Testing for Tuberculosis Add Value to Clinical Decision Making in Hospitalised HIV-Infected Persons? *PLoS ONE* **8**, e54875, doi:10.1371/journal.pone.0054875 (2013).
26 Spielberg, F. *et al.* Field testing and comparative evaluation of rapid, visually read screening assays for antibody to human immunodeficiency virus. *The Lancet* **333**, 580-584 (1989).
27 Addiss, D. G. *et al.* Evaluation of a commercially available enzyme-linked immunosorbent assay for Giardia lamblia antigen in stool. *Journal of clinical microbiology* **29**, 1137-1142 (1991).
28 Sia, S. K., Linder, V., Parviz, B. A., Siegel, A. & Whitesides, G. M. An Integrated Approach to a Portable and Low-Cost Immunoassay for Resource-Poor Settings. *Angewandte Chemie International Edition* **43**, 498-502, doi:10.1002/anie.200353016 (2004).
29 Sun, S., Yang, M., Kostov, Y. & Rasooly, A. ELISA-LOC: lab-on-a-chip for enzyme-linked immunodetection. *Lab on a Chip* **10**, 2093-2100, doi:10.1039/C003994B (2010).
30 Wang, S. *et al.* Micro-a-fluidics ELISA for Rapid CD4 Cell Count at the Point-of-Care. *Scientific reports* **4** (2014).
31 Coskun, A. F. *et al.* A personalized food allergen testing platform on a cellphone. *Lab Chip* **13**, 636-640 (2013).
32 Shen, L., Hagen, J. A. & Papautsky, I. Point-of-care colorimetric detection with a smartphone. *Lab Chip* **12**, 4240-4243, doi:10.1039/c2lc40741h (2012).
33 Guerrero, D. J., DiMenna, W., Flaim, T. D., Mercado, R. & Sun, S. 298-306.
34 Eliasson, H. in *Society of Photo-Optical Instrumentation Engineers (SPIE) Conference Series.* 753709-753711 (Society of Photo-Optical Instrumentation Engineers (SPIE) Conference Series).
35 Galli, C. Modeling systematic errors: polychromatic sources of Beer–Lambert deviations in HPLC/UV and nonchromatographic spectrophotometric assays. *Journal of pharmaceutical and biomedical analysis* **25**, 803-809 (2001).
36 Kristiansen, O. P. & Mandrup-Poulsen, T. Interleukin-6 and diabetes: the good, the bad, or the indifferent? *Diabetes* **54 Suppl 2**, S114-124 (2005).
37 Kugisaki, H. *et al.* Serum concentrations of interleukin-6 in patients following unilateral versus bilateral total knee arthroplasty. *J Orthop Sci* **14**, 437-442, doi:10.1007/s00776-009-1344-9 (2009).
38 Mokart, D. *et al.* Procalcitonin, interleukin 6 and systemic inflammatory response syndrome (SIRS): early markers of postoperative sepsis after major surgery. *Br J Anaesth* **94**, 767-773, doi:10.1093/bja/aei143 (2005).
39 Knüpfer, H. & Preiss, R. Significance of interleukin-6 (IL-6) in breast cancer (review). *Breast Cancer Res Treat* **102**, 129-135, doi:10.1007/s10549-006-9328-3 (2007).
40 Wong, V. W.-S. *et al.* High serum interleukin-6 level predicts future hepatocellular carcinoma development in patients with chronic hepatitis B. *Int J Cancer* **124**, 2766-2770, doi:10.1002/ijc.24281 (2009).
41 Hobisch, A. *et al.* Interleukin-6 regulates prostate-specific protein expression in prostate carcinoma cells by activation of the androgen receptor. *Cancer Res* **58**, 4640-4645 (1998).
42 Blay, J. Y. *et al.* Serum level of interleukin 6 as a prognosis factor in metastatic renal cell carcinoma. *Cancer Res* **52**, 3317-3322 (1992).

43 Flinterman, A. E. *et al.* Children with peanut allergy recognize predominantly Ara h2 and Ara h6, which remains stable over time. *Clin Exp Allergy* **37**, 1221-1228, doi:10.1111/j.1365-2222.2007.02764.x (2007).
44 Sicherer, S. H., Muñoz-Furlong, A., Godbold, J. H. & Sampson, H. A. US prevalence of self-reported peanut, tree nut, and sesame allergy: 11-year follow-up. *J Allergy Clin Immunol* **125**, 1322-1326, doi:10.1016/j.jaci.2010.03.029 (2010).
45 Branum, A. M. & Lukacs, S. *Food allergy among US children: trends in prevalence and hospitalizations*. (US Department of Health and Human Services, Centers for Disease Control and Prevention, National Center for Health Statistics, 2008).
46 Bland, J. M. & Altman, D. G. Statistical methods for assessing agreement between two methods of clinical measurement. *Lancet* **1**, 307-310 (1986).
47 Enders, M. *et al.* Performance of the Elecsys Rubella IgG assay in the diagnostic laboratory setting for assessment of immune status. *Clin Vaccine Immunol* **20**, 420-426, doi:10.1128/cvi.00688-12 (2013).
48 Crofts, N., Maskill, W. & Gust, I. D. Evaluation of enzyme-linked immunosorbent assays: a method of data analysis. *J Virol Methods* **22**, 51-59 (1988).
49 Bland, J. M. & Altman, D. G. Measuring agreement in method comparison studies. *Stat Methods Med Res* **8**, 135-160 (1999).
50 Altman, D. G. Construction of age-related reference centiles using absolute residuals. *Stat Med* **12**, 917-924 (1993).
51 Szczepanik, A. M. *et al.* IL-6 serum levels predict postoperative morbidity in gastric cancer patients. *Gastric Cancer* **14**, 266-273, doi:10.1007/s10120-011-0039-z (2011).
52 Taylor, S. L. *et al.* Threshold dose for peanut: Risk characterization based upon diagnostic oral challenge of a series of 286 peanut-allergic individuals. *Food Chem Toxicol* **48**, 814-819, doi:10.1016/j.fct.2009.12.013 (2010).
53 Pomés, A. *et al.* Monitoring peanut allergen in food products by measuring Ara h 1. *Journal of Allergy and Clinical Immunology* **111**, 640-645, doi:10.1067/mai.2003.118 (2003).
54 Flinterman, A. E. *et al.* Determination of no-observed-adverse-effect levels and eliciting doses in a representative group of peanut-sensitized children. *J Allergy Clin Immunol* **117**, 448-454, doi:10.1016/j.jaci.2005.11.035 (2006).
55 Sicherer, S. H. & Sampson, H. A. Peanut allergy: emerging concepts and approaches for an apparent epidemic. *J Allergy Clin Immunol* **120**, 491-503; quiz 504-495, doi:10.1016/j.jaci.2007.07.015 (2007).
56 Wensing, M. *et al.* The distribution of individual threshold doses eliciting allergic reactions in a population with peanut allergy. *Journal of Allergy and Clinical Immunology* **110**, 915-920, doi:10.1067/mai.2002.129235 (2002).
57 Zurzolo, G. A. *et al.* Peanut Allergen Threshold Study (PATS): validation of eliciting doses using a novel single-dose challenge protocol. *Allergy Asthma Clin Immunol* **9**, 35, doi:10.1186/1710-1492-9-35 (2013).
58 de Souza, V. A. *et al.* Sensitivity and specificity of three ELISA-based assays for discriminating primary from secondary acute dengue virus infection. *J Clin Virol* **39**, 230-233, doi:10.1016/j.jcv.2007.04.005 (2007).
59 Dasso, J., Lee, J., Bach, H. & Mage, R. G. A comparison of ELISA and flow microsphere-based assays for quantification of immunoglobulins. *Journal of immunological methods* **263**, 23-33 (2002).
60 Leng, S. X. *et al.* ELISA and multiplex technologies for cytokine measurement in inflammation and aging research. *The Journals of Gerontology Series A: Biological Sciences and Medical Sciences* **63**, 879-884 (2008).
61 Wu, Y.-Y. *et al.* Limitations on the quantitative determination of telomerase activity by the electrophoretic and ELISA based TRAP assays. *Clinica Chimica Acta* **293**, 199-212 (2000).

62 Barhoumi, A. & Halas, N. J. Label-Free Detection of DNA Hybridization Using Surface Enhanced Raman Spectroscopy. *Journal of the American Chemical Society* **132**, 12792-12793, doi:10.1021/ja105678z (2010).
63 Ray, S., Mehta, G. & Srivastava, S. Label-free detection techniques for protein microarrays: prospects, merits and challenges. *Proteomics* **10**, 731-748, doi:10.1002/pmic.200900458 (2010).
64 Cunningham, B. T. & Laing, L. G. Advantages and application of label-free detection assays in drug screening. *Expert Opinion on Drug Discovery* **3**, 891-901, doi:doi:10.1517/17460441.3.8.891 (2008).
65 Guo, X. Surface plasmon resonance based biosensor technique: a review. *J Biophotonics* **5**, 483-501, doi:10.1002/jbio.201200015 (2012).
66 Homola, J., Vaisocherova, H., Dostalek, J. & Piliarik, M. Multi-analyte surface plasmon resonance biosensing. *Methods* **37**, 26-36, doi:10.1016/j.ymeth.2005.05.003 (2005).
67 Kausaite-Minkstimiene, A., Ramanaviciene, A. & Ramanavicius, A. Surface plasmon resonance biosensor for direct detection of antibodies against human growth hormone. *Analyst* **134**, 2051-2057, doi:10.1039/b907315a (2009).
68 Löfås, S. *et al.* Bioanalysis with surface plasmon resonance. *Sensors and Actuators B: Chemical* **5**, 79-84 (1991).
69 Quinn, J. G. *et al.* Development and application of surface plasmon resonance-based biosensors for the detection of cell-ligand interactions. *Anal Biochem* **281**, 135-143, doi:10.1006/abio.2000.4564 (2000).
70 Chan, L. L., Gosangari, S. L., Watkin, K. L. & Cunningham, B. T. A label-free photonic crystal biosensor imaging method for detection of cancer cell cytotoxicity and proliferation. *Apoptosis* **12**, 1061-1068, doi:10.1007/s10495-006-0031-y (2007).
71 Chan, L. L., Cunningham, B. T., Li, P. Y. & Puff, D. Self-referenced assay method for photonic crystal biosensors: Application to small molecule analytes. *Sensors and Actuators B: Chemical* **120**, 392-398, doi:10.1016/j.snb.2006.02.047 (2007).
72 Choi, C. J., Block, I. D., Bole, B., Dralle, D. & Cunningham, B. T. Label-free photonic crystal biosensor integrated microfluidic chip for determination of kinetic reaction rate constants. *Sensors Journal, IEEE* **9**, 1697-1704 (2009).
73 Threm, D., Nazirizadeh, Y. & Gerken, M. Photonic crystal biosensors towards on-chip integration. *J Biophotonics*, doi:10.1002/jbio.201200039 (2012).
74 Skivesen, N. *et al.* Photonic-crystal waveguide biosensor. *Optics Express* **15**, 3169-3176 (2007).
75 Zhang, W., Ganesh, N., Block, I. D. & Cunningham, B. T. High sensitivity photonic crystal biosensor incorporating nanorod structures for enhanced surface area. *Sensors and Actuators B: Chemical* **131**, 279-284, doi:10.1016/j.snb.2007.11.017 (2008).
76 Choi, C. J. & Cunningham, B. T. Single-step fabrication and characterization of photonic crystal biosensors with polymer microfluidic channels. *Lab Chip* **6**, 1373-1380, doi:10.1039/b603514k (2006).
77 Choi, C. J. & Cunningham, B. T. A 96-well microplate incorporating a replica molded microfluidic network integrated with photonic crystal biosensors for high throughput kinetic biomolecular interaction analysis. *Lab Chip* **7**, 550-556, doi:10.1039/b618584c (2007).
78 Sharon, A., Rosenblatt, D. & Friesem, A. A. Resonant grating?waveguide structures for visible and near-infrared radiation. *Journal of the Optical Society of America A* **14**, 2985-2993, doi:10.1364/JOSAA.14.002985 (1997).
79 Rosenblatt, D., Sharon, A. & Friesem, A. A. Resonant grating waveguide structures. *Ieee Journal of Quantum Electronics* **33**, 2038-2059, doi:Doi 10.1109/3.641320 (1997).
80 George, S. *et al.* Cytotoxicity screening of Bangladeshi medicinal plant extracts on pancreatic cancer cells. *BMC Complement Altern Med* **10**, 52, doi:10.1186/1472-6882-10-52 (2010).
81 Pineda, M. F. *et al.* Rapid Specific and Label-Free Detection of Porcine Rotavirus Using Photonic Crystal Biosensors. *Sensors Journal, IEEE* **9**, 470-477, doi:10.1109/JSEN.2009.2014427 (2009).

82 Shafiee, H. *et al.* Nanostructured Optical Photonic Crystal Biosensor for HIV Viral Load Measurement. *Scientific reports* **4** (2014).
83 Soelberg, S. D., Stevens, R. C., Limaye, A. P. & Furlong, C. E. Surface plasmon resonance detection using antibody-linked magnetic nanoparticles for analyte capture, purification, concentration, and signal amplification. *Analytical chemistry* **81**, 2357-2363 (2009).
84 He, L. *et al.* Colloidal Au-enhanced surface plasmon resonance for ultrasensitive detection of DNA hybridization. *Journal of the American Chemical Society* **122**, 9071-9077 (2000).
85 Lyon, L. A., Musick, M. D. & Natan, M. J. Colloidal Au-enhanced surface plasmon resonance immunosensing. *Analytical Chemistry* **70**, 5177-5183 (1998).
86 Zhu, H. *et al.* Cost-effective and rapid blood analysis on a cell-phone. *Lab Chip* **13**, 1282-1288, doi:10.1039/c3lc41408f (2013).
87 Long, K. D. *et al.* Multimode smartphone biosensing: the transmission, reflection, and intensity spectral (TRI)-analyzer. *Lab on a Chip*, doi:10.1039/C7LC00633K (2017).
88 Ji, D. *et al.* Dielectric-grating-coupled surface plasmon resonance for ultrasensitive sensing. *Frontiers in Optics 2016 (2016), paper JW4A.30*, doi:doi:10.1364/FIO.2016.JW4A.30 (2016).
89 Seydack, M. Nanoparticle labels in immunosensing using optical detection methods. *Biosensors and Bioelectronics* **20**, 2454-2469, doi:http://dx.doi.org/10.1016/j.bios.2004.11.003 (2005).
90 Willets, K. A. & Van Duyne, R. P. Localized surface plasmon resonance spectroscopy and sensing. *Annu. Rev. Phys. Chem.* **58**, 267-297 (2007).
91 Yoon, J.-Y. Latex Immunoagglutination Assay in Lab-on-a-Chip. *Biological Engineering* **1**, 79-94 (2008).
92 Sullivan, F. Advances in Label-Free Detection. Report No. D12D, (Frost & Sullivan Online, 2008).
93 Tiwari, R. (ed PR Newswire) (ProQuest, ABI/INFORM Collection, 2017).
94 Sullivan., F. Overview of the In-vitro Diagnostics Market in India. (2013).
95 Sullivan, F. Analysis of the US Immunochemistry Market. Report No. NE6F, (Frost & Sullivan, 2014).
96 Long, K. D., Woodburn, E. V. & Cunningham, B. T. in *IEEE-NIH 2017 Special Topics Conference on Healthcare Innovations and Point-of-Care Technologies* (IEEE EMB, NIH Natcher Conference Center, Bethesda, MD, 2017).
97 WHO. Health in 2015: from MDGs to SDGs. (World Health Organization, 2015).
98 WHO. in *WHO* (World Health Organization, 2016).
99 Organization, W. H. Preterm birth. (World Health Organization, 2016).
100 WHO recommendations on interventions to improve preterm birth outcomes. (World Health Organization, 2015).
101 Kiefer, D. G. & Vintzileos, A. M. The Utility of Fetal Fibronectin in the Prediction and Prevention of Spontaneous Preterm Birth. *Rev Obstet Gynecol* **1**, 106-112 (2008).
102 Audibert F , e. a. Contingent use of fetal fibronectin testing and cervical length measurement in women with preterm labour. - PubMed - NCBI. (2016).
103 Abbott, D. S., Radford, S. K., Seed, P. T., Tribe, R. M. & Shennan, A. H. Evaluation of a quantitative fetal fibronectin test for spontaneous preterm birth in symptomatic women. *Am J Obstet Gynecol* **208**, 122.e121-126, doi:10.1016/j.ajog.2012.10.890 (2013).
104 Deshpande, S. *et al.* Rapid fetal fibronectin testing to predict preterm birth in women with symptoms of premature labour: a systematic review and cost analysis. doi:http://www.ncbi.nlm.nih.gov/books/NBK261021/ (2013).
105 Prevention, C. f. D. C. a. in *Barriers to Dietary Control Among Pregnant Women with Phenylketonuria— United States, 1998–2000* (Centers for Disease Control and Prevention, CDC Media Relations, 2016).
106 Williams, R. A., Mamotte, C. D. & Burnett, J. R. in *Clin Biochem Rev* Vol. 29 31-41 (2008).
107 Present status of different mass screening procedures for phenylketonuria. Medical Research Council Working Party on phenylketonuria. *Br Med J* **4**, 7-13 (1968).

108 Bhattacharya, K., Wotton, T. & Wiley, V. The evolution of blood-spot newborn screening. *Transl Pediatr* **3**, 63-70, doi:10.3978/j.issn.2224-4336.2014.03.08 (2014).

109 Schoen, E. J., Baker, J. C., Colby, C. J. & To, T. T. Cost-benefit analysis of universal tandem mass spectrometry for newborn screening. *Pediatrics* **110**, 781-786 (2002).

110 Alex R. Kemper, M., MPH, MS1 *et al.* Implementing Point-of-Care Newborn Screening. (US Department of Health and Human Services, Secretary of Health and Human Services Advisory Committee on Heritable Disorders in Newborns and Children, 2012).

111 Leitich, H. & Kaider, A. Fetal fibronectin--how useful is it in the prediction of preterm birth? *Bjog* **110 Suppl 20**, 66-70 (2003).

112 Abbott, D. S. *et al.* Quantitative fetal fibronectin to predict preterm birth in asymptomatic women at high risk. *Obstet Gynecol* **125**, 1168-1176, doi:10.1097/aog.0000000000000754 (2015).

113 Lu, G. C., Goldenberg, R. L., Cliver, S. P., Kreaden, U. S. & Andrews, W. W. Vaginal fetal fibronectin levels and spontaneous preterm birth in symptomatic women. *Obstet Gynecol* **97**, 225-228 (2001).

114 Chen, W. *et al.* Photonic crystal enhanced microscopy for imaging of live cell adhesion. *Analyst* **138**, 5886-5894, doi:10.1039/C3AN01541F (2013).

115 Boudreau, J. & Jones, P. L. Extracellular matrix and integrin signalling: the shape of things to come. *Biochemical Journal* **339**, 481-488 (1999).

116 Barczyk, M., Carracedo, S. & Gullberg, D. Integrins. *Cell and Tissue Research* **339**, 269-280, doi:Doi 10.1007/S00441-009-0834-6 (2010).

117 Frandsen, T. L. *et al.* Assays for the Study of Human Cancer Cell Invasion and Metastasis. *Fibrinolysis* **6**, 71-76 (1992).

118 Rosoff, W. J. *et al.* A new chemotaxis assay shows the extreme sensitivity of axons to molecular gradients (vol 7, pg 678, 2004). *Nature Neuroscience* **7**, 785-785, doi:Doi 10.1038/Nn0704-785 (2004).

119 Jamil, M. M. A. *et al.* Imaging of the cell surface interface using objective coupled widefield surface plasmon microscopy. *Journal of Structural Biology* **164**, 75-80 (2008).

120 Peterson, A. W., Halter, M., Tona, A., Bhadriraju, K. & Plant, A. L. Surface plasmon resonance imaging of cells and surface-associated fibronectin. *Bmc Cell Biology* **10**, -, doi:Doi 10.1186/1471-2121-10-16 (2009).

121 Lin, B., Li, P. Y. & Cunningham, B. T. A label-free biosensor-based cell attachment assay for characterization of cell surface molecules. *Sensors and Actuators B* **114**, 559-561 (2006).

122 McGuinness, R. Impedance-based cellular assay technologies: recent advances, future promise. *Current Opinion in Pharmacology* **7**, 535-540 (2007).

123 Rothenhausler, B. & Knoll, W. Surface-Plasmon Microscopy. *Nature* **332**, 615-617, doi:Doi 10.1038/332615a0 (1988).

124 Caldwell, M. E. & Yeatman, E. M. Surface-plasmon spatial light modulators based on liquid crystal. *Appl Opt* **31**, 3880-3891, doi:10.1364/AO.31.003880 (1992).

125 Bardin, F., Bellemain, A., Roger, G. & Canva, M. Surface plasmon resonance spectro-imaging sensor for biomolecular surface interaction characterization. *Biosens Bioelectron* **24**, 2100-2105, doi:DOI 10.1016/j.bios.2008.10.023 (2009).

126 Chinowsky, T. M., Mactutis, T., Fu, E. & Yager, P. Optical and electronic design for a high-performance surface plasmon resonance imager. 173-182, doi:10.1117/12.538536 (2004).

127 Binnig, G., Quate, C. F. & Gerber, C. Atomic force microscope. *Phys Rev Lett* **56**, 930-933 (1986).

128 Cunningham, B. *et al.* A plastic colorimetric resonant optical biosensor for multiparallel detection of label-free biochemical interactions. *Sensors and Actuators B-Chemical* **85**, 219-226, doi:Pii S0925-4005(02)00111-9 (2002).

129 Cunningham, B. T. *et al.* Label-free assays on the BIND system. *Journal of Biomolecular Screening* **9**, 481-490, doi:Doi 10.1177/1087057104267604 (2004).

130 Mathias, P. C. *et al.* Improved Sensitivity of DNA Microarrays Using Photonic Crystal Enhanced Fluorescence. *Analytical Chemistry* **82**, 6854-6861, doi:Doi 10.1021/Ac100841d (2010).
131 Winkler, M. *et al.* A quantitative assay for insulin-expressing colony-forming progenitors. *J Vis Exp*, e3148, doi:10.3791/3148 (2011).
132 zur Nieden, N. I., Cormier, J. T., Rancourt, D. E. & Kallos, M. S. Embryonic stem cells remain highly pluripotent following long term expansion as aggregates in suspension bioreactors. *Journal of Biotechnology* **129**, 421-432, doi:http://dx.doi.org/10.1016/j.jbiotec.2007.01.006 (2007).
133 Miller, C. L. & Lai, B. in *Basic Cell Culture Protocols* 71-89 (Springer, 2005).
134 Seiler, C. *et al.* Time-lapse microscopy and classification of 2D human mesenchymal stem cells based on cell shape picks up myogenic from osteogenic and adipogenic differentiation. *Journal of Tissue Engineering and Regenerative Medicine*, n/a-n/a, doi:10.1002/term.1575 (2012).
135 Tang, X. *et al.* Attenuation of cell mechanosensitivity in colon cancer cells during in vitro metastasis. *PLoS One* **7**, e50443, doi:10.1371/journal.pone.0050443 (2012).
136 Wehrle-Haller, B. & Imhof, B. A. Actin, microtubules and focal adhesion dynamics during cell migration. *The International Journal of Biochemistry & Cell Biology* **35**, 39-50, doi:http://dx.doi.org/10.1016/S1357-2725(02)00071-7 (2003).
137 Cooper, G. in *The Cell: A Molecular Approach* (ed GM Cooper) Ch. 11, (2004).
138 Smith, J. T., Elkin, J. T. & Reichert, W. M. Directed cell migration on fibronectin gradients: Effect of gradient slope. *Experimental Cell Research* **312**, 2424-2432, doi:http://dx.doi.org/10.1016/j.yexcr.2006.04.005 (2006).
139 Nemethova, M., Auinger, S. & Small, J. V. Building the actin cytoskeleton: filopodia contribute to the construction of contractile bundles in the lamella. *J Cell Biol* **180**, 1233-1244, doi:10.1083/jcb.200709134 (2008).
140 Cummings, B. S., Kinsey, G. R., Bolchoz, L. J. C. & Schnellmann, R. G. Identification of Caspase-Independent Apoptosis in Epithelial and Cancer Cells. *Journal of Pharmacology and Experimental Therapeutics* **310**, 126-134, doi:10.1124/jpet.104.065862 (2004).
141 Karaman, M. W. *et al.* A quantitative analysis of kinase inhibitor selectivity. *Nat Biotechnol* **26**, 127-132, doi:10.1038/nbt1358 (2008).
142 Sengenès, C. *et al.* Chemotaxis and Differentiation of Human Adipose Tissue CD34+/CD31− Progenitor Cells: Role of Stromal Derived Factor-1 Released by Adipose Tissue Capillary Endothelial Cells. *STEM CELLS* **25**, 2269-2276, doi:10.1634/stemcells.2007-0180 (2007).
143 e Silva, R. L. *et al.* The SDF-1/CXCR4 ligand/receptor pair is an important contributor to several types of ocular neovascularization. *The FASEB Journal* **21**, 3219-3230 (2007).
144 Liu, X. *et al.* SDF-1 Promotes Endochondral Bone Repair during Fracture Healing at the Traumatic Brain Injury Condition. *PloS one* **8**, e54077 (2013).
145 Jiang, L. *et al.* The expression and role of stromal cell-derived factor-1alpha-CXCR4 axis in human dental pulp. *J Endod* **34**, 939-944, doi:10.1016/j.joen.2008.05.015 (2008).
146 Suzuki, T. *et al.* Induced migration of dental pulp stem cells for in vivo pulp regeneration. *Journal of dental research* **90**, 1013-1018 (2011).
147 Kucia, M. *et al.* CXCR4-SDF-1 signalling, locomotion, chemotaxis and adhesion. *J Mol Histol* **35**, 233-245 (2004).
148 Gong, Q. M., Quan, J. J., Jiang, H. W. & Ling, J. Q. Regulation of the stromal cell-derived factor-1alpha-CXCR4 axis in human dental pulp cells. *J Endod* **36**, 1499-1503, doi:10.1016/j.joen.2010.05.011 (2010).
149 Kumar, S. & Weaver, V. M. Mechanics, malignancy, and metastasis: the force journey of a tumor cell. *Cancer Metastasis Rev* **28**, 113-127, doi:10.1007/s10555-008-9173-4 (2009).
150 Global report: UNAIDS report on the global AIDS epidemic 2013. (Joint United Nations Programme on HIV/AIDS, Geneva, Switzerland, 2013).
151 The Global Burden of Disease: Generating Evidence, Guiding Policy. (Institute for Health Metrics and Evaluation, 2010).

152 House, U. S. in *H.R. 1298* Vol. Public Law 108-25 (ed 108th Congress) (Congress.gov, 2003).
153 World Health Organization. A New Health Sector Agenda for HIV/AIDS: Global Health Sector Strategy on HIV/AIDS, 2011-2015., (2011).
154 WHO & UNICEF and UNAIDS. Global Update on HIV Treatment 2013: Results, Impact and Opportunities. (World Health Organization, Geneva, Switzerland., 2013).
155 World Health Organization. Consolidated Guidelines on the Use of Antiretroviral Drugs for Treating and Preventing HIV Infection: Recommendations for a Public Health Approach. (Geneva, Switzerland., 2013).
156 Mellors, J. W. *et al.* Plasma viral load and CD4+ lymphocytes as prognostic markers of HIV-1 infection. *Ann Intern Med* **126**, 946-954 (1997).
157 Mylonakis, E., Paliou, M. & Rich, J. D. Plasma viral load testing in the management of HIV infection. *Am Fam Physician* **63**, 483-490, 495-486 (2001).
158 Mellors, J. W. *et al.* Prognosis in HIV-1 infection predicted by the quantity of virus in plasma. *Science* **272**, 1167-1170 (1996).
159 Rouet, F. & Rouzioux, C. HIV-1 viral load testing cost in developing countries: what's new? *Expert Review of Molecular Diagnostics* **7**, 703-707, doi:doi:10.1586/14737159.7.6.703 (2007).
160 Fiscus, S. A. *et al.* HIV-1 Viral Load Assays for Resource-Limited Settings. *PLoS Med* **3**, e417, doi:10.1371/journal.pmed.0030417 (2006).
161 Klein, D. Quantification using real-time PCR technology: applications and limitations. *Trends in Molecular Medicine* **8**, 257-260, doi:http://dx.doi.org/10.1016/S1471-4914(02)02355-9 (2002).
162 Luft, L. M., Gill, M. J. & Church, D. L. HIV-1 viral diversity and its implications for viral load testing: review of current platforms. *International Journal of Infectious Diseases* **15**, e661-e670, doi:http://dx.doi.org/10.1016/j.ijid.2011.05.013 (2011).
163 Stevens, G., Rekhviashvili, N., Scott, L. E., Gonin, R. & Stevens, W. Evaluation of Two Commercially Available, Inexpensive Alternative Assays Used for Assessing Viral Load in a Cohort of Human Immunodeficiency Virus Type 1 Subtype C-Infected Patients from South Africa. *Journal of Clinical Microbiology* **43**, 857-861, doi:10.1128/jcm.43.2.857-861.2005 (2005).
164 world Health Organization. Antiretroviral Therapy for HIV Infection in Adults and Adolescents: Recommendations for a Public Health Approach., (Geneva, Switzerland., 2010).
165 Bustin, S. A. & Nolan, T. Pitfalls of Quantitative Real-Time Reverse-Transcription Polymerase Chain Reaction. *J Biomol Tech* **15**, 155-166 (2004).
166 Mora, J. *et al.* Next Generation Ligand Binding Assays-Review of Emerging Technologies' Capabilities to Enhance Throughput and Multiplexing. *Aaps Journal* **16**, 1175-1184, doi:Doi 10.1208/S12248-014-9660-1 (2014).
167 Fischer, S. K. *et al.* Emerging Technologies to Increase Ligand Binding Assay Sensitivity. *Aaps Journal* **17**, 93-101, doi:Doi 10.1208/S12248-014-9682-8 (2015).
168 Rissin, D. M. *et al.* Single-molecule enzyme-linked immunosorbent assay detects serum proteins at subfemtomolar concentrations. *Nature Biotechnology* **28**, 595-U525, doi:Doi 10.1038/Nbt.1641 (2010).
169 Aguirre, M. A., Long, K. D., Li, N., Manoto, S. L. & Cunningham, B. T. Detection and digital resolution counting of nanoparticles with optical resonators and applications in biosensing. *Chemosensors* (In Review).
170 Squires, T. M., Messinger, R. J. & Manalis, S. R. Making it stick: convection, reaction and diffusion in surface-based biosensors. *Nature biotechnology* **26**, 417-426 (2008).
171 Adamson, C. S. & Freed, E. O. in *Advances in Pharmacology* Vol. Volume 55 (ed Jeang Kuan-Teh) 347-387 (Academic Press, 2007).
172 Sauter, M. M. *et al.* An internalization signal in the simian immunodeficiency virus transmembrane protein cytoplasmic domain modulates expression of envelope glycoproteins on the cell surface. *J Cell Biol* **132**, 795-811 (1996).

173 Wyss, S. *et al.* The highly conserved C-terminal dileucine motif in the cytosolic domain of the human immunodeficiency virus type 1 envelope glycoprotein is critical for its association with the AP-1 clathrin adaptor [correction of adapter]. *J Virol* **75**, 2982-2992, doi:10.1128/jvi.75.6.2982-2992.2001 (2001).
174 Checkley, M. A., Luttge, B. G. & Freed, E. O. HIV-1 envelope glycoprotein biosynthesis, trafficking, and incorporation. *J Mol Biol* **410**, 582-608, doi:10.1016/j.jmb.2011.04.042 (2011).
175 Rits-Volloch, S., Frey, G., Harrison, S. C. & Chen, B. Restraining the conformation of HIV-1 gp120 by removing a flexible loop. *EMBO J* **25**, 5026-5035, doi:10.1038/sj.emboj.7601358 (2006).
176 Zhou, T. *et al.* Structural definition of a conserved neutralization epitope on HIV-1 gp120. *Nature* **445**, 732-737, doi:http://www.nature.com/nature/journal/v445/n7129/suppinfo/nature05580_S1.html (2007).
177 Kwong, P. D. *et al.* Structure of an HIV gp120 envelope glycoprotein in complex with the CD4 receptor and a neutralizing human antibody. *Nature* **393**, 648-659 (1998).
178 Pancera, M. *et al.* Structure and immune recognition of trimeric pre-fusion HIV-1 Env. *Nature* **514**, 455-461, doi:10.1038/nature13808 (2014).
179 Endres, M. J. *et al.* CD4-independent infection by HIV-2 is mediated by fusin/CXCR4. *Cell* **87**, 745-756 (1996).
180 Reeves, J. D. *et al.* CD4-independent infection by HIV-2 (ROD/B): use of the 7-transmembrane receptors CXCR-4, CCR-3, and V28 for entry. *Virology* **231**, 130-134 (1997).
181 Wyatt, R. *et al.* The antigenic structure of the HIV gp120 envelope glycoprotein. *Nature* **393**, 705-711 (1998).
182 Eggink, D. *et al.* Lack of complex N-glycans on HIV-1 envelope glycoproteins preserves protein conformation and entry function. *Virology* **401**, 236-247, doi:10.1016/j.virol.2010.02.019 (2010).
183 van Montfort, T. *et al.* HIV-1 N-Glycan Composition Governs a Balance between Dendritic Cell-Mediated Viral Transmission and Antigen Presentation. *The Journal of Immunology* **187**, 4676-4685, doi:10.4049/jimmunol.1101876 (2011).
184 Walker, B. D. *et al.* Inhibition of human immunodeficiency virus syncytium formation and virus replication by castanospermine. *Proceedings of the National Academy of Sciences* **84**, 8120-8124 (1987).
185 Izquierdo-Useros, N. *et al.* Siglec-1 Is a Novel Dendritic Cell Receptor That Mediates HIV-1 Trans-Infection Through Recognition of Viral Membrane Gangliosides. *PLoS Biol* **10**, e1001448, doi:10.1371/journal.pbio.1001448 (2012).
186 Geijtenbeek, T. B. H. *et al.* DC-SIGN, a Dendritic Cell–Specific HIV-1-Binding Protein that Enhances trans-Infection of T Cells. *Cell* **100**, 587-597, doi:http://dx.doi.org/10.1016/S0092-8674(00)80694-7 (2000).
187 Izquierdo-Useros, N. *et al.* Siglec-1 Is a Novel Dendritic Cell Receptor That Mediates HIV-1 <italic>Trans</italic>-Infection Through Recognition of Viral Membrane Gangliosides. *PLoS Biol* **10**, e1001448, doi:10.1371/journal.pbio.1001448 (2012).
188 Chen, B. *et al.* Structure of an unliganded simian immunodeficiency virus gp120 core. *Nature* **433**, 834-841, doi:http://www.nature.com/nature/journal/v433/n7028/suppinfo/nature03327_S1.html (2005).
189 Chen, B. *et al.* Determining the structure of an unliganded and fully glycosylated SIV gp120 envelope glycoprotein. *Structure* **13**, 197-211, doi:10.1016/j.str.2004.12.004 (2005).
190 Kwon, Y. D. *et al.* Unliganded HIV-1 gp120 core structures assume the CD4-bound conformation with regulation by quaternary interactions and variable loops. *Proc Natl Acad Sci U S A* **109**, 5663-5668, doi:10.1073/pnas.1112391109 (2012).
191 Liu, J., Bartesaghi, A., Borgnia, M. J., Sapiro, G. & Subramaniam, S. Molecular architecture of native HIV-1 gp120 trimers. *Nature* **455**, 109-113, doi:http://www.nature.com/nature/journal/v455/n7209/suppinfo/nature07159_S1.html (2008).

192 Huang, C.-c. *et al.* Structure of a V3-Containing HIV-1 gp120 Core. *Science* **310**, 1025-1028, doi:10.1126/science.1118398 (2005).
193 Pancera, M. *et al.* Structure of HIV-1 gp120 with gp41-interactive region reveals layered envelope architecture and basis of conformational mobility. *Proc Natl Acad Sci U S A* **107**, 1166-1171, doi:10.1073/pnas.0911004107 (2010).
194 Xiang, S.-H. *et al.* A V3 Loop-Dependent gp120 Element Disrupted by CD4 Binding Stabilizes the Human Immunodeficiency Virus Envelope Glycoprotein Trimer. *Journal of Virology* **84**, 3147-3161, doi:10.1128/jvi.02587-09 (2010).
195 Mao, Y. *et al.* Subunit organization of the membrane-bound HIV-1 envelope glycoprotein trimer. *Nat Struct Mol Biol* **19**, 893-899, doi:http://www.nature.com/nsmb/journal/v19/n9/abs/nsmb.2351.html#supplementary-information (2012).
196 Hwang, S. S., Boyle, T. J., Lyerly, H. K. & Cullen, B. R. Identification of the envelope V3 loop as the primary determinant of cell tropism in HIV-1. *Science* **253**, 71-74 (1991).
197 Resch, W., Hoffman, N. & Swanstrom, R. Improved Success of Phenotype Prediction of the Human Immunodeficiency Virus Type 1 from Envelope Variable Loop 3 Sequence Using Neural Networks. *Virology* **288**, 51-62, doi:http://dx.doi.org/10.1006/viro.2001.1087 (2001).
198 Mao, Y. *et al.* Molecular architecture of the uncleaved HIV-1 envelope glycoprotein trimer. *Proceedings of the National Academy of Sciences* **110**, 12438-12443, doi:10.1073/pnas.1307382110 (2013).
199 Mao, Y., Castillo-Menendez, L. R. & Sodroski, J. G. Reply to Subramaniam, van Heel, and Henderson: Validity of the cryo-electron microscopy structures of the HIV-1 envelope glycoprotein complex. *Proceedings of the National Academy of Sciences* **110**, E4178-E4182, doi:10.1073/pnas.1316666110 (2013).
200 Rusert, P. *et al.* Interaction of the gp120 V1V2 loop with a neighboring gp120 unit shields the HIV envelope trimer against cross-neutralizing antibodies. *J Exp Med* **208**, 1419-1433, doi:10.1084/jem.20110196 (2011).
201 Bartesaghi, A., Merk, A., Borgnia, M. J., Milne, J. L. S. & Subramaniam, S. Prefusion structure of trimeric HIV-1 envelope glycoprotein determined by cryo-electron microscopy. *Nat Struct Mol Biol* **20**, 1352-1357, doi:10.1038/nsmb.2711 (2013).
202 Munro, J. B. *et al.* Conformational dynamics of single HIV-1 envelope trimers on the surface of native virions. *Science* **346**, 759-763, doi:10.1126/science.1254426 (2014).
203 Bohl, C. *et al.* A twin-cysteine motif in the V2 region of gp120 is associated with SIV envelope trimer stabilization. *PLoS One* **8**, e69406, doi:10.1371/journal.pone.0069406 (2013).
204 Yokoyama, M., Naganawa, S., Yoshimura, K., Matsushita, S. & Sato, H. Structural Dynamics of HIV-1 Envelope Gp120 Outer Domain with V3 Loop. *PLoS ONE* **7**, e37530, doi:10.1371/journal.pone.0037530 (2012).
205 Olshevsky, U. *et al.* Identification of individual human immunodeficiency virus type 1 gp120 amino acids important for CD4 receptor binding. *Journal of virology* **64**, 5701-5707 (1990).
206 Désormeaux, A. *et al.* The highly conserved layer-3 component of the HIV-1 gp120 inner domain is critical for CD4-required conformational transitions. *J Virol* **87**, 2549-2562, doi:10.1128/jvi.03104-12 (2013).
207 Tran, E. E. H. *et al.* Structural Mechanism of Trimeric HIV-1 Envelope Glycoprotein Activation. *PLoS Pathog* **8**, e1002797, doi:10.1371/journal.ppat.1002797 (2012).
208 Biscone, M. J. *et al.* Functional impact of HIV coreceptor-binding site mutations. *Virology* **351**, 226-236, doi:http://dx.doi.org/10.1016/j.virol.2006.03.017 (2006).
209 Garg, H., Viard, M., Jacobs, A. & Blumenthal, R. Targeting HIV-1 gp41-induced fusion and pathogenesis for anti-viral therapy. *Curr Top Med Chem* **11**, 2947-2958 (2011).
210 Lyumkis, D. *et al.* Cryo-EM Structure of a Fully Glycosylated Soluble Cleaved HIV-1 Envelope Trimer. *Science* **342**, 1484-1490, doi:10.1126/science.1245627 (2013).

211 Julien, J.-P. *et al.* Crystal structure of a soluble cleaved HIV-1 envelope trimer. *Science* **342**, 1477-1483, doi:10.1126/science.1245625 (2013).
212 Deshayes, S., Morris, M., Heitz, F. & Divita, G. Delivery of proteins and nucleic acids using a non-covalent peptide-based strategy. *Advanced Drug Delivery Reviews* **60**, 537-547, doi:http://dx.doi.org/10.1016/j.addr.2007.09.005 (2008).
213 Galdiero, S. *et al.* Peptide-lipid interactions: experiments and applications. *Int J Mol Sci* **14**, 18758-18789, doi:10.3390/ijms140918758 (2013).
214 Abrahamyan, L. G., Markosyan, R. M., Moore, J. P., Cohen, F. S. & Melikyan, G. B. Human immunodeficiency virus type 1 Env with an intersubunit disulfide bond engages coreceptors but requires bond reduction after engagement to induce fusion. *J Virol* **77**, 5829-5836 (2003).
215 Markosyan, R. M., Cohen, F. S. & Melikyan, G. B. HIV-1 envelope proteins complete their folding into six-helix bundles immediately after fusion pore formation. *Mol Biol Cell* **14**, 926-938, doi:10.1091/mbc.E02-09-0573 (2003).
216 Chan, R. *et al.* Retroviruses human immunodeficiency virus and murine leukemia virus are enriched in phosphoinositides. *J Virol* **82**, 11228-11238, doi:10.1128/jvi.00981-08 (2008).
217 Blumenthal, R., Durell, S. & Viard, M. HIV Entry and Envelope Glycoprotein-mediated Fusion. *Journal of Biological Chemistry* **287**, 40841-40849, doi:10.1074/jbc.R112.406272 (2012).
218 Subramaniam, S. Structure of trimeric HIV-1 envelope glycoproteins. *Proceedings of the National Academy of Sciences* **110**, E4172-E4174, doi:10.1073/pnas.1313802110 (2013).
219 van Heel, M. Finding trimeric HIV-1 envelope glycoproteins in random noise. *Proceedings of the National Academy of Sciences* **110**, E4175-E4177, doi:10.1073/pnas.1314353110 (2013).
220 Henderson, R. Avoiding the pitfalls of single particle cryo-electron microscopy: Einstein from noise. *Proceedings of the National Academy of Sciences* **110**, 18037-18041, doi:10.1073/pnas.1314449110 (2013).
221 Kovacs, J. M. *et al.* Stable, uncleaved HIV-1 envelope glycoprotein gp140 forms a tightly folded trimer with a native-like structure. *Proc Natl Acad Sci U S A* **111**, 18542-18547, doi:10.1073/pnas.1422269112 (2014).
222 Kong, L., Wilson, I. A. & Kwong, P. D. Crystal structure of a fully glycosylated HIV-1 gp120 core reveals a stabilizing role for the glycan at Asn262. *Proteins: Structure, Function, and Bioinformatics* **83**, 590-596, doi:10.1002/prot.24747 (2015).
223 Alsahafi, N., Debbeche, O., Sodroski, J. & Finzi, A. Effects of the I559P gp41 Change on the Conformation and Function of the Human Immunodeficiency Virus (HIV-1) Membrane Envelope Glycoprotein Trimer. *PLoS One* **10**, e0122111, doi:10.1371/journal.pone.0122111 (2015).
224 Crooks, E. T. *et al.* A comparative immunogenicity study of HIV-1 virus-like particles bearing various forms of envelope proteins, particles bearing no envelope and soluble monomeric gp120. *Virology* **366**, 245-262, doi:10.1016/j.virol.2007.04.033 (2007).
225 Watkins, D. I. Update on progress in HIV vaccine development. *Top Antivir Med* **20**, 30-31 (2012).
226 UNAIDS. Fast-Track - Ending the AIDS epidemic by 2030. *Joint United Nations Programme on HIV/AIDS* (2014).